N75-17018
file

NASA CR-
147653

OBSERVATION OF BOW SHOCK PROTONS AT THE LUNAR ORBIT

BY

JOHN L. BENSON

DEPARTMENT OF

SPACE PHYSICS
AND
ASTRONOMY

RICE UNIVERSITY

HOUSTON, TEXAS 77001

(NASA-CR-147653) OESERVATION OF BOW SHOCK PROTONS AT THE LUNAE CRBIT M.S. Thesis (Rice Univ.) 248 p HC $8.00 CSCL 03B
N76-23118
Unclas
G3/90 27656

RICE UNIVERSITY

Observation of Bow Shock Protons at the Lunar Orbit

by

John Louis Benson

A THESIS SUBMITTED
IN PARTIAL FULFILLMENT OF THE
REQUIREMENTS FOR THE DEGREE OF

Master of Science

Thesis Director's Signature:

John W. Freeman

Houston, Texas

April, 1974

ABSTRACT

Observation of Bow Shock Protons at the Lunar Orbit

by

John Louis Benson

Protons with energies ranging from about 500 eV to 3500 eV are observed by the Suprathermal Ion Detector Experiment on both the dusk and dawn sides of the magnetosphere. On each lunation these particles appear as a rather continuous phenomenon for 3 to 5 days after crossing from the dawn-side magnetosheath into the solar wind and for about 2 days prior to entering the dusk-side magnetosheath.

Transverse proton flows of this type have been observed by Asbridge et al., [1968], Scarf et al., [1970] and are believed to be deviated solar wind particles that are accelerated at the earth's bow shock and emitted outwardly along interplanetary field lines at greater than solar wind energies.

Data from the SIDE and from the Explorer 35 lunar orbiting magnetometer have been analyzed and these data indicate that the transverse ion flows observed by the SIDE in the pre and post bow shock crossing regions of the lunar orbit are due to these deviated solar wind particles.

A computer model based on $\vec{E}X\vec{B}$ drift trajectories for particles leaving the shock has been developed and synthetic particle data produced by this model are in good agreement with the observed data.

Table of Contents

Chapter 1

This thesis is concerned with the study of the plasma environment of the moon; particularly when the moon is outside the earth's magnetosphere and in the interplanetary medium. Much has been learned about this environment as a result of placing particles and fields experiments directly on the lunar surface during the six Apollo moon landings and the following work consists of the analysis of data returned to earth by one such experiment, the Suprathermal Ion Detector Experiment, otherwise known as SIDE.

The plasma environment of the moon should not be considered independently of the earth's magnetosphere and the interplanetary medium and a brief review of the basic ideas and observations concerning the complex interactions of the solar corpuscular radiation, (solar wind), and the near extra-magnetospheric region with the earth moon system is in order before going on to a detailed discussion of the results of this analysis.

1.1 General Survey

The sun continuously ejects a tenuous supersonic plasma, known as the solar wind, that consists mostly of protons and electrons in equal amounts. The plasma is tenuous in that typical number densities are on the order of a few particles per cubic centimeter and supersonic in that the bulk flow velocity of the plasma is greater than the Alfvén speed in the medium. The Alfvén speed is,

$$V_A = B/(4\pi\ \rho\ )^{1/2} \sim 50 \text{ km/sec} \qquad 1\text{-}1$$

in the interplanetary medium and is the quantity analogous to the sound speed in a collision dominated medium. The average bulk flow velocity of the solar wind is about 400 km/sec giving an Alfvénic Mach number, V_{bf}/V_A of about 8, indicating the highly supersonic flow.

The solar wind drags the sun's magnetic field lines along with it due to the essentially infinite conductivity in the plasma in such a manner that the ambient interplanetary magnetic field lines intersect the earth's orbit at approximately a 45° angle to the earth-sun line. The field lines in figure 1-1 are shown at this "garden hose angle."

The radial flow of plasma from the sun appears to come from a direction about 5° to the west of the solar direction due to the earth's orbital velocity of about 30 km/sec.

Upon reaching the orbit of the earth, the solar wind plasma is unable to penetrate the earth's dipolar field; it therefore compresses the field creating a cavity in the flow known as the magnetosphere. The solar wind flows around this

Figure 1-1. View of the magnetosphere and the lunar orbit in the ecliptic plane. Typical magnetic field lines in the interplanetary medium and in the magnetosphere are shown.

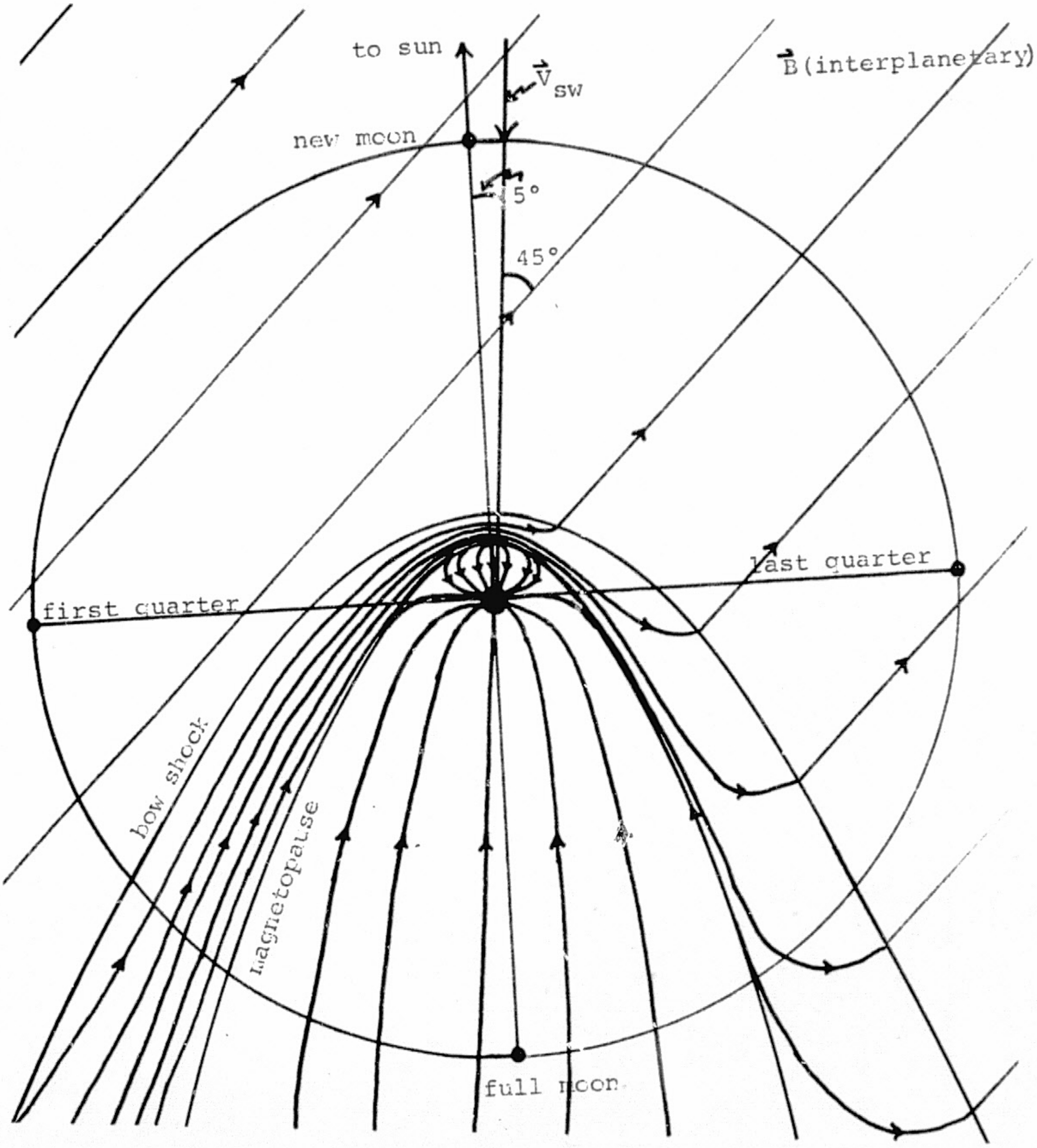

to sun
$\vec{V}_{sw}$
$\vec{B}$(interplanetary)
new moon
45°
45°
first quarter
last quarter
bow shock
Magnetopause
full moon

Figure 1-1

cavity in a fashion resembling hydrodynamic flow. The boundary of the cavity is called the magnetopause and the distance from the center of the earth along the earth-sun line to this boundary is on the order of 10 R_e (earth radii).

The supersonic nature of the solar wind gives rise to a detached shock wave a few R_e upstream of the magnetopause. This standing shock, known as the bow shock, was predicted by Zhigulev and Romishevskii in 1959 and by Axford in 1962. Its existence was confirmed by the IMP 1 satellite, Ness [1964]. Due to the excessively long collision mean free path of a solar wind particle, $\sim$ 1 A.U., the shock is not collision dominated or even collision influenced. Nevertheless, the high conductivity in the plasma causes it to behave somewhat like a fluid and shock calculations using the "fluid dynamic analogy", Spreiter et al. [1966], work fairly well in predicting the location of the shock. See figure 1-2. A few R_e upstream of the shock there is only relatively cool, ($T \sim 10^4$ °K), tenuous, ($n \lesssim 10/cm^{-3}$), unshocked plasma with a weak interplanetary field, ($B \sim 5\gamma$), imbedded in it. For a summary of the properties of the quiet solar wind, see table 1-1. Closer to the shock, where interplanetary field lines intersect the shock surface, complex interactions of the solar wind and the shock take place and energetic particles have been observed flowing upstream of the shock in this region by several investigators; Asbridge et al. [1968],

Figure 1-2. Measurements of the positions of the magnetopause and bow shock from IMP 1,[after Ness, (1965)].

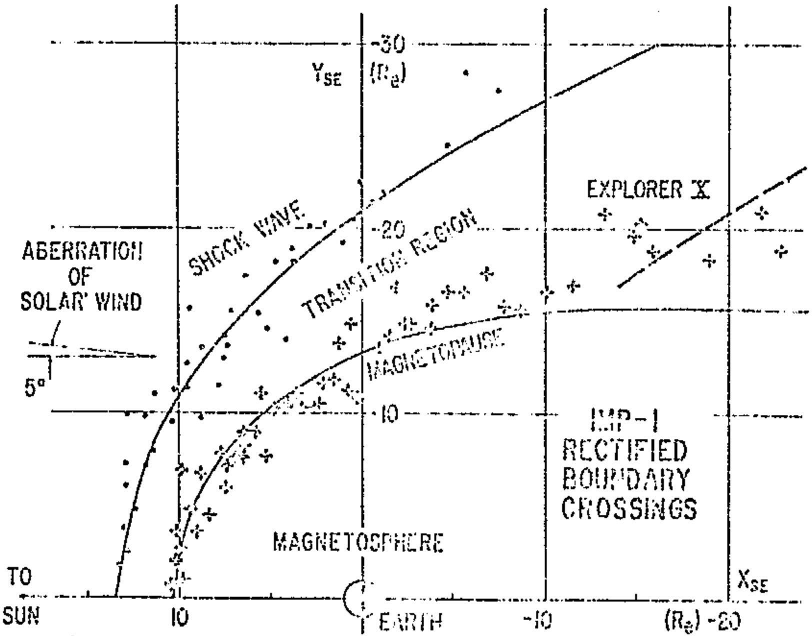
-30
Y_SE
(R_e)
EXPLORER X
SHOCK WAVE
-20
TRANSITION REGION
ABERRATION OF SOLAR WIND
5°
MAGNETOPAUSE
-10
IMP-1
RECTIFIED
BOUNDARY
CROSSINGS
MAGNETOSPHERE
TO SUN
10
EARTH
-10
(R_e) -20
X_SE

Figure 1-2

Table 1-1

Observed Properties of the Quiet Solar Wind

bulk flow velocity	320 km/sec
number density	8 cm^{-3}
proton temperature	$4X10^4$°K
proton thermal anisotropy ratio	2
electron temperature	1 to $1.5X10^5$ °K
magnetic field strength	5γ
proton flux	$2.4X10^8$ $cm^{-2}sec^{-1}$
kinetic energy flux	.22 erg $cm^{-2}sec^{-1}$
kinetic energy density	$7X10^{-9}$ erg cm^{-3}
proton thermal energy density	$6X10^{-11}$ erg cm^{-3}
electron thermal energy density	$1.5X10^{-10}$ erg cm^{-3}
magnetic field energy density	10^{-10} erg cm^{-3}

Frank and Shope [1968], Anderson [1968] and Freeman [1972]. These energetic particles, specifically protons in the energy range of .5 to 3.5 keV are the subject of this thesis. A more detailed discussion of these observations is given below.

After passing through the shock, the temperature of the plasma is increased, ($T \sim 10^6 °K$), the magnetic field is compressed, ($B \sim 20 \gamma$), density goes up, ($n \sim 30/cm^{-3}$) and the bulk flow velocity goes down. Some of the ordered streaming energy is converted to disordered thermal energy. Figure 1-3 summarizes the changes in plasma parameters across the shock. The region of space between the magnetopause and the bow shock is known as the transition region or the magnetosheath and the detailed plasma properties of this region near the lunar orbit are discussed by Fenner [1971,1974].

The inside of the magnetosphere is essentially shielded from the solar wind flow and figure 1-4 depicts the general particle and field morphology relevant to the lunar environment in this region of space. The earth's dipolar field is compressed on the day side in to about 10 R_e and drawn out on the night side at least several tens of R_e past the lunar orbit [Ness et al., 1967], in the anti-solar direction.

The dipolar field lines are closed near the earth, but the distance in the anti-solar direction to which this closing extends is not well established. At a distance of more than about 10 R_e, the field tends to point either toward or

Figure 1-3a. Typical changes in plasma parameters across the bow shock. Note that C=sound speed and b=Alfvén speed. M_O =mach number M_A =Alfvén mach number. [after McKenzie, (1970)].

Figure 1-3b. Measured changes in plasma parameters across the shock. [after Wolfe and McKibbin, (1968)].

Figure 1-4. View of magnetosphere in noon-midnight meridian plane. [after Ness, (1965)].

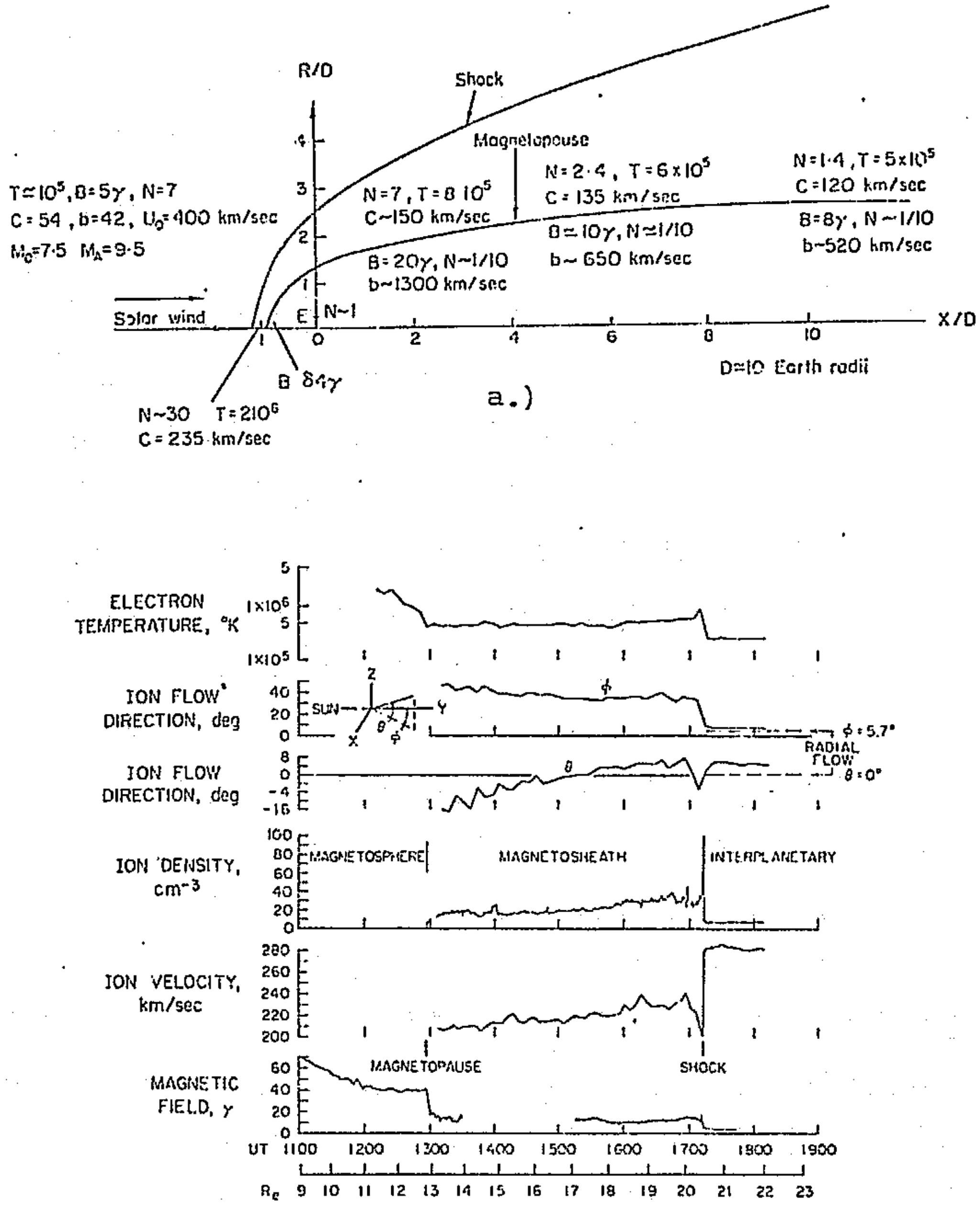
R/D
Shock
Magnetopause
T≃10⁵, B=5γ, N=7
C=54, b=42, U₀=400 km/sec
M₀=7.5 M_A=9.5
N=7, T=8 10⁵
C~150 km/sec
N=2.4, T=6×10⁵
C=135 km/sec
N=1.4, T=5×10⁵
C=120 km/sec
B=20γ, N~1/10
b~1300 km/sec
B≃10γ, N≃1/10
b~650 km/sec
B=8γ, N~1/10
b~520 km/sec
Solar wind
E
N~1
X/D
1 0 2 4 6 8 10
1 2 3 4
B δ4γ
N~30 T=210⁶
C=235 km/sec
D=10 Earth radii
ELECTRON TEMPERATURE, °K
5
1×10⁶
5
1×10⁵
ION FLOW DIRECTION, deg
40 20 0
Z
SUN
Y
X
θ
φ
φ=5.7°
RADIAL FLOW
ION FLOW DIRECTION, deg
8 0 -4 -16
θ
θ=0°
ION DENSITY, cm⁻³
100 80 60 40 20 0
MAGNETOSPHERE
MAGNETOSHEATH
INTERPLANETARY
ION VELOCITY, km/sec
280 260 240 220 200
MAGNETIC FIELD, γ
60 40 20 0
MAGNETOPAUSE
SHOCK
UT 1100 1200 1300 1400 1500 1600 1700 1800 1900
R_e 9 10 11 12 13 14 15 16 17 18 19 20 21 22 23

a.)

b.)

Figure 1-3

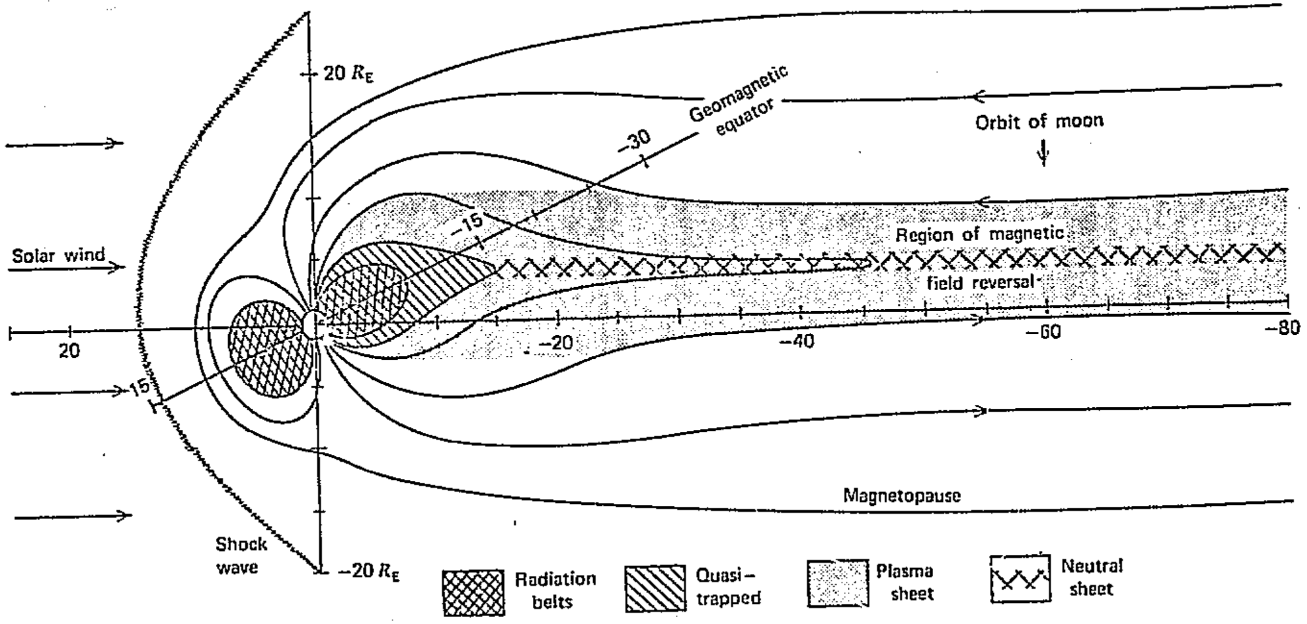
Solar wind
20
15
Shock wave
20 R_E
−20 R_E
−15
−30
Geomagnetic equator
Orbit of moon
Region of magnetic field reversal
−20
−40
−60
−80
Magnetopause
Radiation belts
Quasi-trapped
Plasma sheet
Neutral sheet

Figure 1-4

away from the sun. Although the field lines may be weakly closed ($B_{Z_{se}} << 1$) at 60 R_e, the morphology of the geomagnetic tail in this region can generally be described as a planar neutral sheet with the field lines roughly parallel to the sheet above and below with the sense of the field being toward the sun north of the neutral sheet and away from the sun south of the neutral sheet. The thickness of the neutral sheet at 60 R_e is not well known, but Bowling, [1973] has set a value of about 3 R_e at a distance of 30 R_e in the anti-solar direction.

The magnetic neutral sheet region is also filled with a relatively warm, ($T_i \sim 10^8 °K$), rarefied, ($n \sim 10^{-1}/cm^{-3}$), plasma that surrounds the neutral plane with a thickness of about 3 to 7 R_e at the lunar distance as determined by CPLEE, [Rich, 1973]. See chapter 2 for a description of the Charged Particle Lunar Environment Experiment. The source of the particles in this "plasma sheet" is not well established, but it is believed that they are solar wind particles that have entered the magnetosphere through the magnetopause or through open tail field lines at large distances in the anti-solar direction.

The above brief description of the regions of the magnetosphere and interplanetary medium through which the moon passes allows one to summarize the changing plasma environment of the moon, disregarding any lunar atmospheric phenomena, as follows.

Beginning at new moon, (see figure 1-1), the moon is in the undisturbed solar wind where the ordered streaming plasma rams the sunward side directly without going through a shock wave and the earthward side faces a plasma void that lines up with the solar wind aberration direction. The absence of a lunar bow shock was discovered from Explorer 35 magnetometer data, [Colburn, 1967] and the plasma void was identified using a plasma probe flown on the same spacecraft, [Lyon et al., 1967]. The Explorer 35 magnetometer has also determined that a slight enhancement of the interplanetary field occurs while the satellite is in the moon's optical shadow, [Colburn et al., 1968].

At first quarter the conditions are essentially the same as at new moon, as long as the interplanetary field does not change its streaming angle appreciably. That is, at first quarter the interplanetary magnetic field lines still do not connect the moon and the bow shock so that the bow shock can not yet influence the lunar environment.

When the moon proceeds toward the dusk magnetosheath, it will begin to encounter field lines connected to the bow shock with the probability of observing bow shock associated particles becoming larger as the moon moves closer to the shock.

After passing into the dusk magnetosheath, the plasma environment changes considerably from that just outside the shock. As discussed above, the density increases, the bulk flow velocity decreases and the temperature increases. The magnetic field is enhanced in this region and particle spectra become very stable with peak energies around 500 eV.

By the time the moon has reached full phase it is well into the geomagnetic tail where it experiences multiple neutral sheet crossings and encounters with the plasma sheet; densities decrease from magnetosheath values and temperatures increase.

As the moon passes from the full to the last quarter phase it crosses the dawn magnetosheath where the plasma parameters are similar to those in the dusk magnetosheath but differences in turbulent effects are observed. The dusk magnetosheath exhibits a correlation in turbulence and geomagnetic activity (Kp) and the dawn magnetosheath does not. [Fenner, 1974].

The region between the dawn bow shock and the point at which the last interplanetary field line tangent to the shock intersects the lunar orbit, (see figure 1-1), is the primary region of interest in this thesis since the probability of observing bow shock protons is greatest here.

1.2 Observations of bow shock associated phenomena, upstream of the shock.

Several investigators have observed energetic particles and wave disturbances upstream of the earth's bow shock. A brief summary of those observations follows.

Waves of frequency 10-100 Hz propagating along interplanetary field lines have been detected upstrea of the earth's bow shock by the OGO-1 search coil magnetometer, [Smith et al., 1967]. These waves are believed to be precursor waves propagating upstream in the whistler mode parallel to the field lines. Similar observations of whistler waves upstream of the shock were made by Heppner et al. [1967] although the frequencies were about 1 Hz with the waves being detected in small packets of 4 to 6 cycles. The amplitudes of these waves were found to diminish with increasing distance from the shock which led Heppner to suggest that they were generated at or were associated with the shock itself.

A comprehensive study of upstream waves was made by Fairfield [1969], using Explorer 34 data. He determined that waves of frequency 0.01 to 0.05 Hz upstream of the bow shock are a permanent feature of the region of space extending from the bow shock out to about 34 R_e. These waves are observed 90% of the time when the interplanetary field intersects the shock and Fairfield believes them to be locally generated Alfvén waves due to the outward streaming protons observed by Asbridge and other investigators. He argues that the whistler waves must have a fairly high frequency ($\nu \gtrsim 10$ Hz) to propagate upstream as shown by Smith et al. [1967]. Processes that would explain the necessarily large

Doppler shifting to .01 Hz in the rest frame of the spacecraft would be difficult to explain.

Greenstadt et al. [1968] have contributed further to the association of these low frequency waves with particles by showing a correlation in magnetic field oscillation and particle fluxes outside the shock. Energetic electrons (energy ≥ 40 keV) have also been observed in the upstream region by Anderson [1968], and by Jokipii [1968]. Protons of 1 keV were observed upstream of the shock by Frank and Shope [1968], with the IMP-4 satellite while the detector was looking in the anti-solar direction. Freeman [1972] has also observed energetic ions in the deep lunar night with the suprathermal ion detector on the lunar surface when the detector was looking as near as 17° to the anti-solar direction. Freeman points out that these ions are probably not from the earth's bow shock and that they are most likely associated with deviated solar wind flow around the moon. Examples of outwardly flowing protons are reported by Asbridge et al. [1968], using data from six Vela satellites. The results reported in their paper are particularly relevent to the present work and this paper will now be discussed in more detail.

Asbridge and co-workers report the results of the analysis of particle data from the six Vela satellites which are in nearly circular earth orbits at 18 R_e. The energy analyzers on board are capable of detecting protons in the range of 0.1 to 20 keV. All of the Vela satellites are spin stabilized and sample only certain directions in spacecraft azimuth. Vela's 2 and 3 spin at about 2 rps and take five measurements near the solar direction and others at 90°, 180°, and 270° from the solar direction. The Vela 4 satellites spin at about 1 rpm taking seven measurements of proton spectra near the solar direction and a measurement each 22 1/2° of rotation thereafter.

Several examples of proton flows in the energy range 3 to 6 keV are presented in this paper. These protons are observed to come from the direction of the earth's bow shock and figure 1-5a,b,c shows two examples of the dawn side flows and one example of a dusk side flow. An analysis of four months of Vela 3A and 3B data shows that these outwardly flowing protons are a permanent feature of the dusk-dawn bow shock region and figure 1-5d summarizes these results. Arrows indicate direction of flow and dots indicate flow in the solar direction. A higher incidence of outwardly flowing protons is noted when the spacecraft are on the dawn side of the magnetosphere. The authors suggest that these protons are solar wind particles that are accelerated at the bow shock and emitted outwardly from the shock along interplanetary field lines. Figure 1-6 summarizes the model suggested by these investigators and it is shown in this thesis that this model

Figure 1-5a. Dawn-side transverse proton flow from the bow shock as observed by Vela 3B; 291° spacecraft azimuth points toward the bow shock while on the dawn side. (energy ~ 4 keV).

Figure 1-5b. Dusk-side transverse flow from Vela 2B observations at 18 R_e. (energy ~ 3 keV).

Figure 1-5c. Vela 3A dusk-side observation of transverse flow at 89° from the solar direction. (energy ~ 5 keV).

Figure 1-5d. Summary of four months of Vela 3A and 3B data. Arrows indicate direction of the flow; dots indicate flow in the solar direction.

Figure 1-6. Diagram of Asbridge model to explain the observed transverse proton flows.

Figures 1-5 and 1-6 are from [Asbridge et al. (1968)].

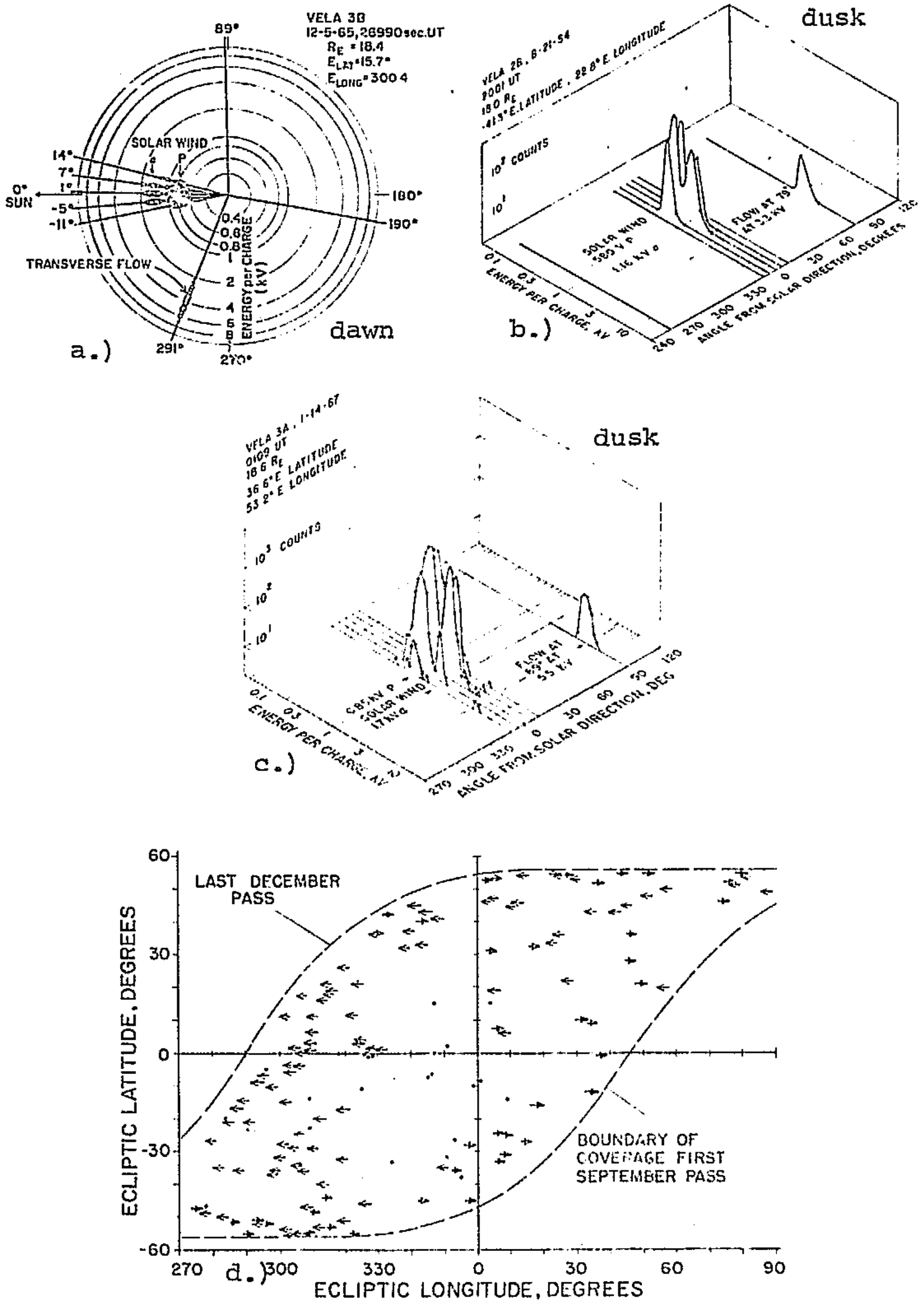
VELA 3B
12-5-65, 26990 sec. UT
R_E = 18.4
E_{LAT} = 15.7°
E_{LONG} = 300.4
89°
SOLAR WIND
α
P
14°
7°
1°
0° SUN
-5°
-11°
180°
190°
0.4
0.6
0.8
1
2
4
6
8
ENERGY per CHARGE (kV)
TRANSVERSE FLOW
291°
270°
dawn
a.)
VELA 2B, 8-21-64
2001 UT
18.0 R_E
41.3° E. LATITUDE, 22.8° E. LONGITUDE
10^3 COUNTS
10^1
SOLAR WIND
.580 V P
1.16 kV α
FLOW AT 79°
AT 3.3 kV
0.1
0.3
1
3
10
ENERGY PER CHARGE, kV
240
270
300
330
0
30
60
90
120
ANGLE FROM SOLAR DIRECTION, DEGREES
dusk
b.)
VELA 3A, 1-14-67
0109 UT
18.6 R_E
36.6° E LATITUDE
53.2° E LONGITUDE
10^3 COUNTS
10^2
10^1
0.85 kV P
SOLAR WIND
1.7 kV α
FLOW AT
-49° AT
5.5 kV
0.1
0.3
1
3
10
ENERGY PER CHARGE, kV
270
300
330
0
30
60
90
120
ANGLE FROM SOLAR DIRECTION, DEG
dusk
c.)
LAST DECEMBER PASS
BOUNDARY OF COVERAGE FIRST SEPTEMBER PASS
60
30
0
-30
-60
ECLIPTIC LATITUDE, DEGREES
270
300
330
0
30
60
90
ECLIPTIC LONGITUDE, DEGREES
d.)

Figure 1-5

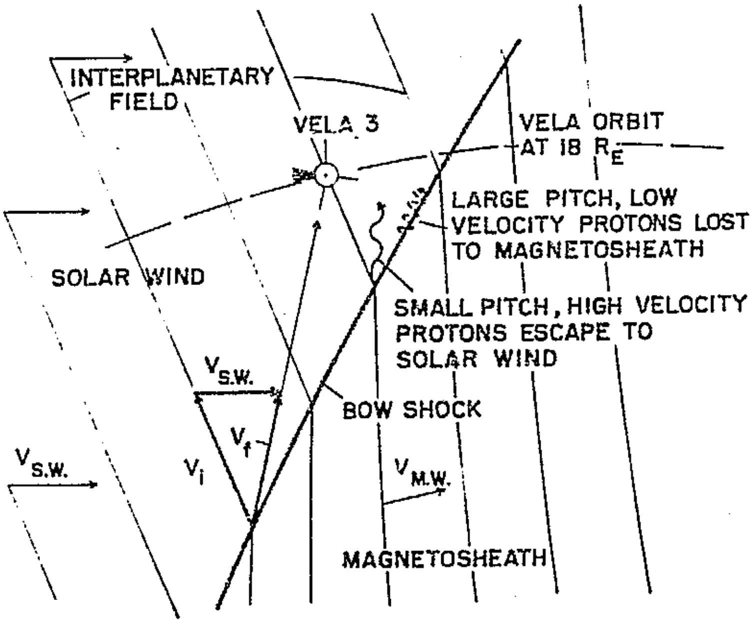
INTERPLANETARY FIELD
VELA 3
VELA ORBIT AT 18 R_E
LARGE PITCH, LOW VELOCITY PROTONS LOST TO MAGNETOSHEATH
SOLAR WIND
SMALL PITCH, HIGH VELOCITY PROTONS ESCAPE TO SOLAR WIND
$V_{S.W.}$
BOW SHOCK
V_f
$V_{S.W.}$
V_i
$V_{M.W.}$
MAGNETOSHEATH

Figure 1-6

is at least partially correct. A more realistic model is developed and discussed along with the Asbridge model in chapter 3.

1.3 Research Objectives

The SIDE observes a variety of ion spectra in the region of space between the bow shock and the terminator. The dominant spectrum is one that is depleted in the lower energies and peaks toward the higher energies. Other spectra show double peaks with one doubly peaked type occuring near the bow shock and the other near the terminator. The lack of a complete understanding of the ion data in this region and the fact that the dominant spectrum is what one would expect from bow shock protons lead to the following research objectives;

a.) to determine whether or not the moderate to higher energy ions observed by SIDE for several days after passing out of the magnetosheath and into the solar wind are particles from the earth's bow shock.

b.) to identify these particles in the data, further explaining some of the more complicated spectra observed in this region , [Lindeman, 1971].

c.) to propose and develop a theoretical model to explain how bow shock protons can reach the lunar orbit.

Chapter 2

2.1 Basic Theory of Instrument Operation

e basic idea behind the SIDE and most particle detectors with energy discrimination capability is simply that the trajectory of a charged particle is altered upon its entering a region in which there exists an electric field. Detectors that are based on this principle often employ a set of parallel plates across which a potential difference is applied to generate the electrostatic field. A channel electron multiplier is placed at the end of the plates as a counter. If the configuration of the plates is such that the electric field is applied perpendicular to the trajectory of the incoming particle, then the amount of deviation from that initial trajectory depends on the energy of the particle and the strength of the electric field.

The very simplest configuration for such a detector would be a pair of straight parallel plates of length L that are separated by a distance d. Then if a potential V is applied across the plates, a particle entering the region between the plates on a trajectory that is parallel to the plates and at a distance of d/2 above the bottom plate, must have an energy that is at least equal to

$$\mathcal{E}_c = q\,\frac{L^2 V}{2d^2} \qquad \text{2-1}$$

to get through the plates, where q is equal to the charge of the particle.

This configuration is not very useful since it only provides the lower limit on the particle energy, i.e. a particle with energy greater than $\mathcal{E}_c$ can also make it through the plates. The energies of particles that get into the counter can be confined to a narrow range if the parallel plates are curved. The SIDE employs such a pair of curved plates in both the total ion detector (TID) and the mass analyzer detector (MA).

The potential, as a function of r, between the curved plates is given by,

$$\phi(r) = \frac{V \ln(r/a)}{\ln(b/a)} \qquad 2\text{-}2$$

where b is the radius of curvature of the outer plate and a is the radius of curvature of the inner plate(see figure 2-1), V is the total potential difference across the plates.

The electric field is given by,

$$\vec{E} = -\vec{\nabla}\phi \qquad 2\text{-}3$$

so that the field strength is

$$E = \frac{V}{\ln(b/a)} \frac{1}{r} \qquad 2\text{-}4$$

The force exerted on a particle of charge q, moving through the curved plates is ,

$$\vec{F}_p = q\,\vec{E}$$

Figure 2-1. Schematic representation of parallel plate electrostatic energy analyzers, flat and curved. Crossed $\vec{E}$ and $\vec{B}$ fields (Wien velocity filter) preceed the Low Energy Curved Plate Analyzer to form the Mass Analyzer.

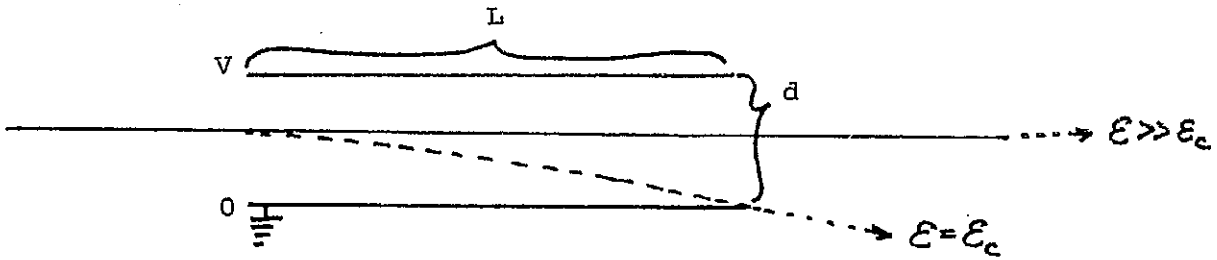

flat plates

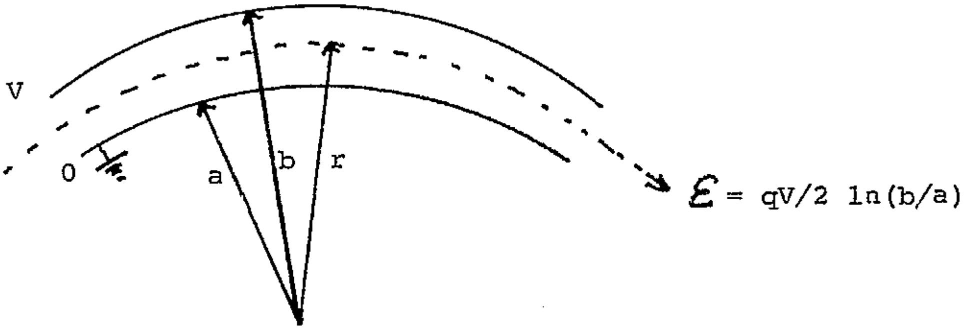

curved plates

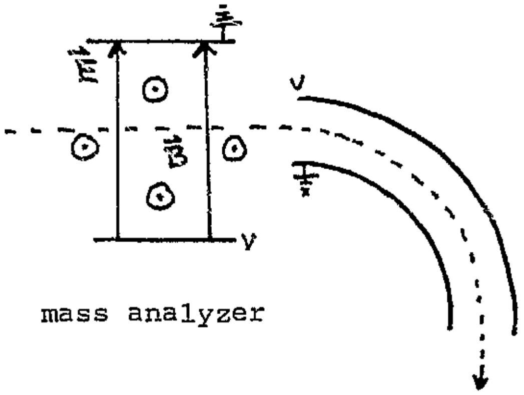

mass analyzer

$$V = E / B$$

$$\mathcal{E}/q = V/2 \ln(b/a)$$

$$(m/q) = 2\mathcal{E}/V^2 q$$

Figure 2-1

and the centrifugal force on the particle of mass m, is,

$$F_c = \frac{m\,v^2}{r} \qquad 2\text{-}6$$

If these forces are balanced, the particle will make it through the plates and into the counter. That is, the energy per unit charge of a particle that gets through is a function of the potential difference across the plates and the plate separation.

$$\mathcal{E}/q = \frac{V}{2\,\ln(b/a)} \qquad 2\text{-}7$$

Equation 2-7 is only approximately correct since equation 2-2 was derived for infinitely long cylindrically concentric plates. The parallel plates of the detector are merely a section of the concentric cylinders and hence, edge effects are important in determining the correct equation relating the energy and the potential difference across the plates. The geometry of the plates and these edge effects give rise to a finite range of energies that may be passed at a particular value of V. The results of the calibration of the Apollo 14 instrument to determine the size of the energy passband are shown in figure 2-2. The bandwidth at the nominal center energy is approximately 10% of the center energy.

2.2 Mass Analyzer

The curved plates of the mass analyzer are preceeded by a

Figure 2-2. Some calibration results of the Apollo 14 Total Ion Detector. Upper part of the graph shows the unidirectional geometric factor as a function of the nominal center energy. Lower part shows the energy bandpass (FWHM) as a function of the nominal center energy. Note that the bandpass is approximately 10% of the center energy.

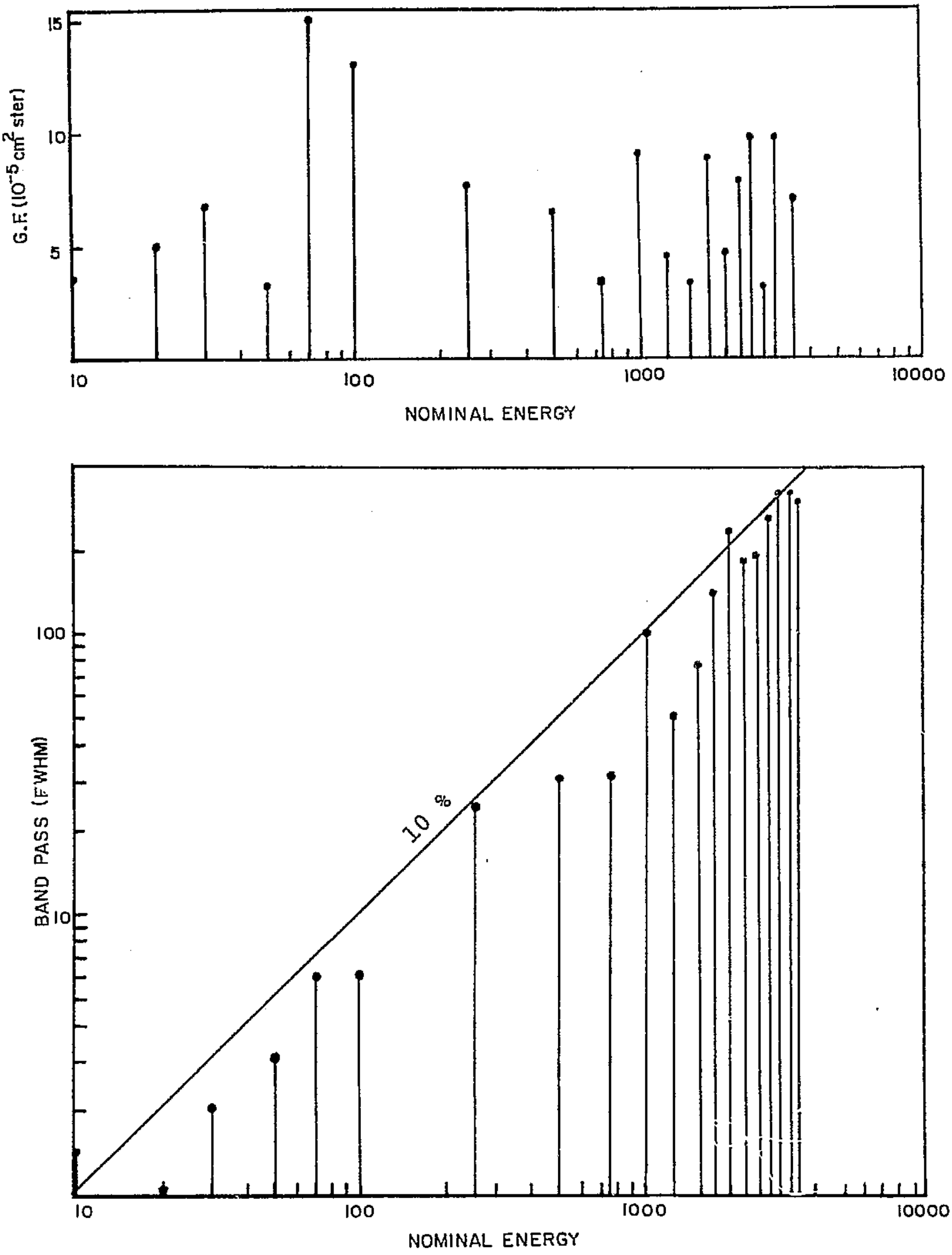
G.F. (10^{-5} cm^2 ster)
15
10
5
10
100
1000
10000
NOMINAL ENERGY
BAND PASS (FWHM)
100
10
10 %
10
100
1000
10000
NOMINAL ENERGY

Figure 2-2

Wien velocity filter which consists of crossed electric and magnetic fields that select the incoming particle's velocity before it is energy-analyzed in the curved plates. If the particle's velocity and its energy per unit charge are known, then the mass per unit charge is simply,

$$m/q = 2\,\mathcal{E}/(v^2 q) \qquad \text{2-8}$$

Upon entering crossed electric and magnetic fields, a charged particle experiences two forces, one associated with the $\vec{E}$ field and one associated with the $\vec{B}$ field. The relative strengths of these two fields determines the resultant trajectory of the particle. The force due to $\vec{E}$ is,

$$\vec{F}_e = q\,\vec{E} \qquad \text{2-9}$$

and that due to $\vec{B}$ is,

$$\vec{F}_b = q\,\vec{v} \times \vec{B} \qquad \text{2-10}$$

so that if,

$$\vec{F}_e + \vec{F}_b = 0 \qquad \text{2-11}$$

the particle goes through the fields undeviated from its initial trajectory. This requires that the particle have a velocity,

$$v = E/B \qquad \text{2-12}$$

to pass through the velocity filter and into the curved plate analyzer.

The $\vec{E}$ field of the velocity filter is provided by flat parallel plates and the $\vec{B}$ field is provided by a permanent magnet. By adjusting the voltage on the plates, various ratios of $\vec{E}$ to $\vec{B}$ can be obtained, thus allowing only particles of certain velocities through the filter.

The basic idea behind the mass analyzer is also depicted in figure 2-1.

2.3 Description of the instrument

Figure 2-3 shows schematically the arrangement of the various components of the instrument. The SIDE has two positive ion detectors, one of which is preceeded by a Wien velocity filter, as discussed above, and this detector is known as the mass analyzer detector (MA). The curved plate analyzer, associated with the mass analyzer is connected to a voltage stepping supply and is sensitive to energies per unit charge ranging from 48.6 to 0.2 eV/q and is referred to as the Low Energy Curved Plate Analyzer (LECPA). After passing through the velocity filter and the LECPA, an ion enters a counter known as a Bendix Channeltron®. This channel electron multiplier is held at a potential of -3.5 kV to accelerate the ions after they pass out of the LECPA. This post acceleration of the ions affords a higher detection efficiency of the channeltron which emits a cascade of secondary electrons whenever an ion strikes its interior.

Figure 2-3. Schematic diagram of the electrical connections of the TID and MA. [Hills et al. (1971)].

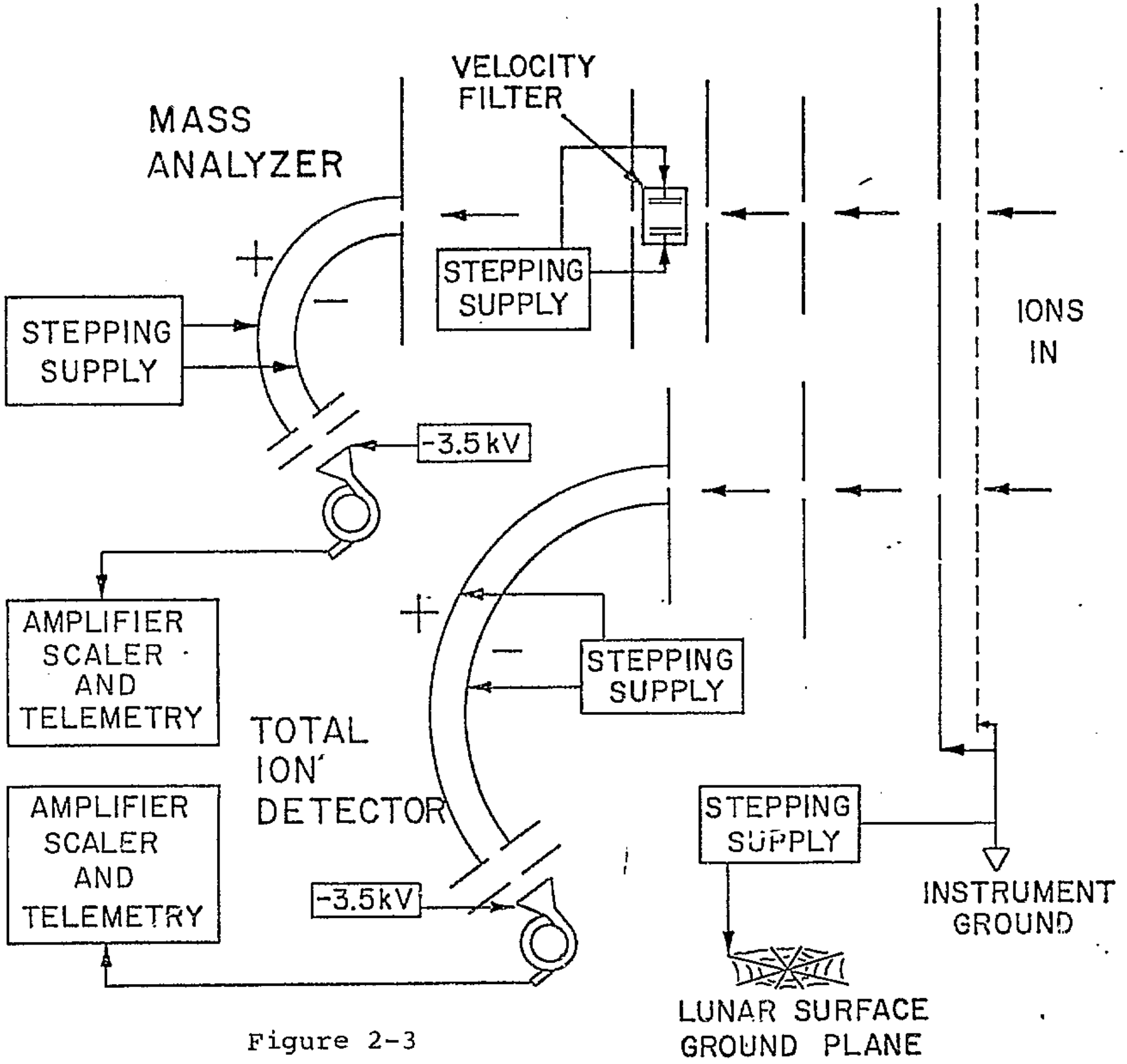
VELOCITY FILTER
MASS ANALYZER
+
−
STEPPING SUPPLY
STEPPING SUPPLY
IONS IN
-3.5kV
AMPLIFIER SCALER AND TELEMETRY
+
−
STEPPING SUPPLY
TOTAL ION DETECTOR
AMPLIFIER SCALER AND TELEMETRY
-3.5kV
STEPPING SUPPLY
INSTRUMENT GROUND
LUNAR SURFACE GROUND PLANE

Figure 2-3

The curved plate analyzer associated with the total ion detector (TID), is known as the High Energy Curved Plate Analyzer (HECPA). It is also connected to a voltage stepping supply and is designed to pass energies per unit charge ranging from 3.5 keV/q to 10 eV/q. Ions leaving the HECPA are also post accelerated into a channeltron. The physical arrangement of the various components of the instrument is shown in figure 2-4.

The velocity filter for each of the three instruments is different and hence each measures a different mass range. Table 2-1 summarizes the energy and mass sensitivities of the three instruments and figure 2-5 shows some results of the mass analyzer calibration.

Each SIDE is also equipped with a spider web-like screen (see figures 2-6,2-7) made of conducting material, that connects the instrument to the lunar surface through a voltage stepping supply. Figure 2-7 is a schematic representation of this connection. The voltage supply is also connected to a wire grid above the ion entrance apertures. This grid is at instrument ground.

The purpose of the ground plane stepper is to compensate for any existing lunar surface potential and to determine its value. For example, if the lunar surface potential is +10 Volts with 0 volts across the stepping supply and the instrument is electrically connected to the surface, then a 10 eV

Figure 2-4. Diagram of the internal configuration of the various components of the SIDE. [after Freeman et al. (1969)].

Figure 2-5. Results of mass analyzer calibration. (plotted from data compiled by Lindeman [1973]).

Figure 2-6. External view of SIDE showing ground plane and grid over the entrance aperature of the instrument. [from Freeman et al. (1969)].

Figure 2-7. Schematic diagram showing relation between grid and ground plane. The ground plane is tied to the aperature grid through a stepping voltage supply.

Energy Steps (eV/q)		Approximate Mass Ranges (amu)			Ground Plane Stepper (volts)
TID	MA	XII	XIV	XV	
10	48.6	10-1500	6-750	1-90	0.0
20	16.2				0.6
30	5.4				1.2
50	1.8				1.8
70	.6				2.4
100	.2				3.6
250					5.4
500					7.8
750					10.2
1000					16.2
1250					19.8
1500					27.6
1750					0.0
2000					-.6
2250					-1.2
2500					-1.8
2750					-2.4
3000					-3.6
3250					-5.4
3500					-7.8
					-10.2
					-16.2
					-19.8
					-27.6

Table 2-1

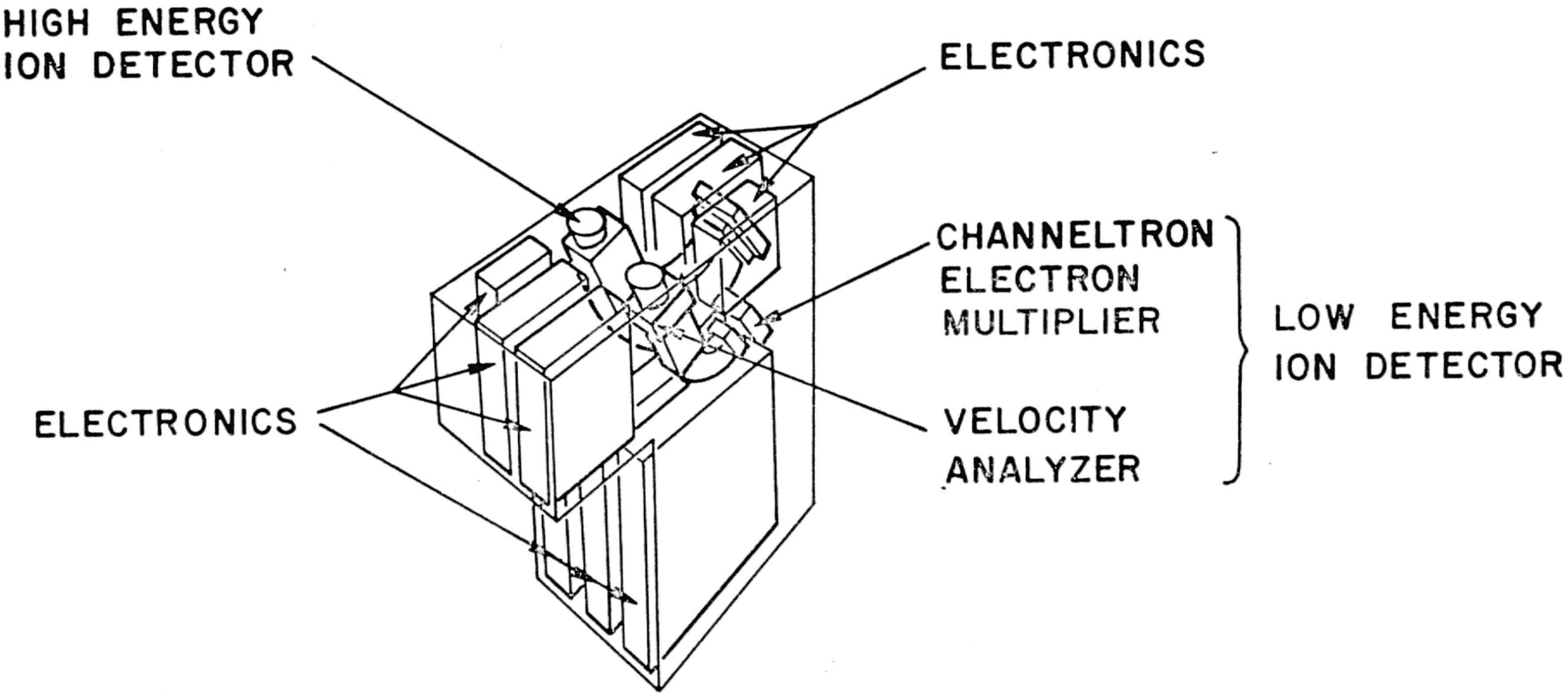

INTERNAL DIAGRAM OF THE SUPRATHERMAL ION DETECTOR EXPERIMENT

Figure 2-4

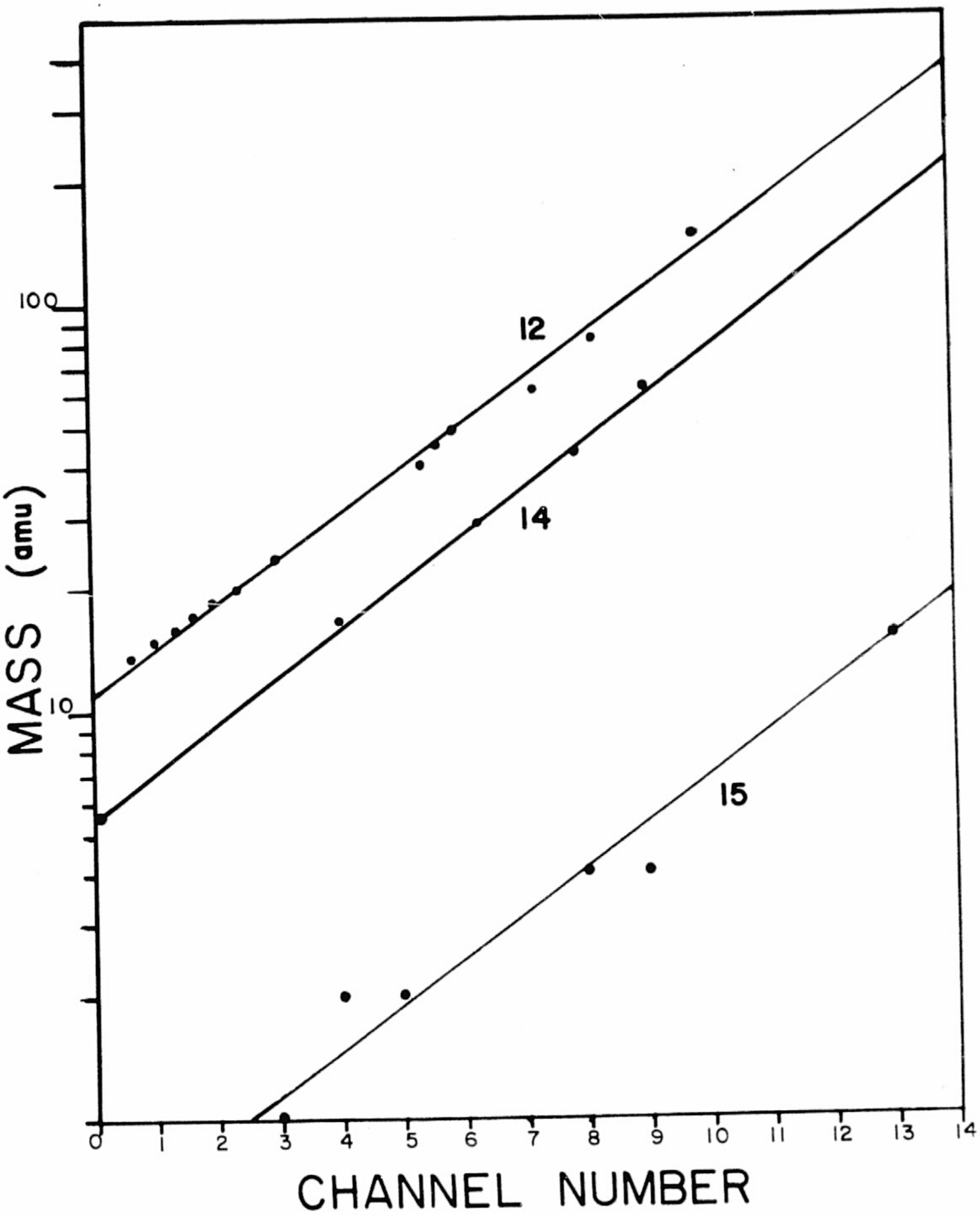

MASS (amu)
100
10
CHANNEL NUMBER
0
1
2
3
4
5
6
7
8
9
10
11
12
13
14
12
14
15

Figure 2-5

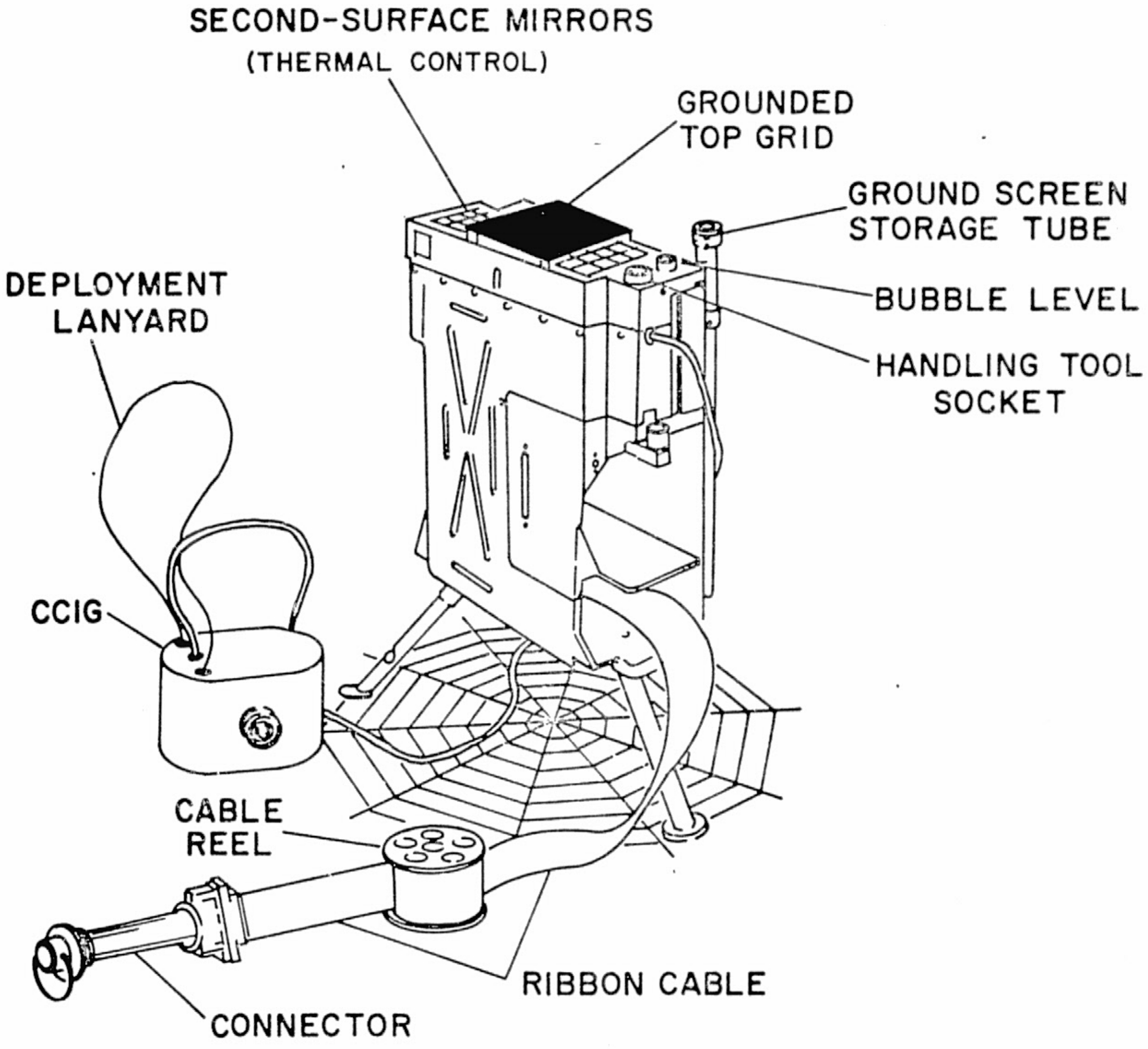

DEPLOYED CONFIGURATION

Figure 2-6

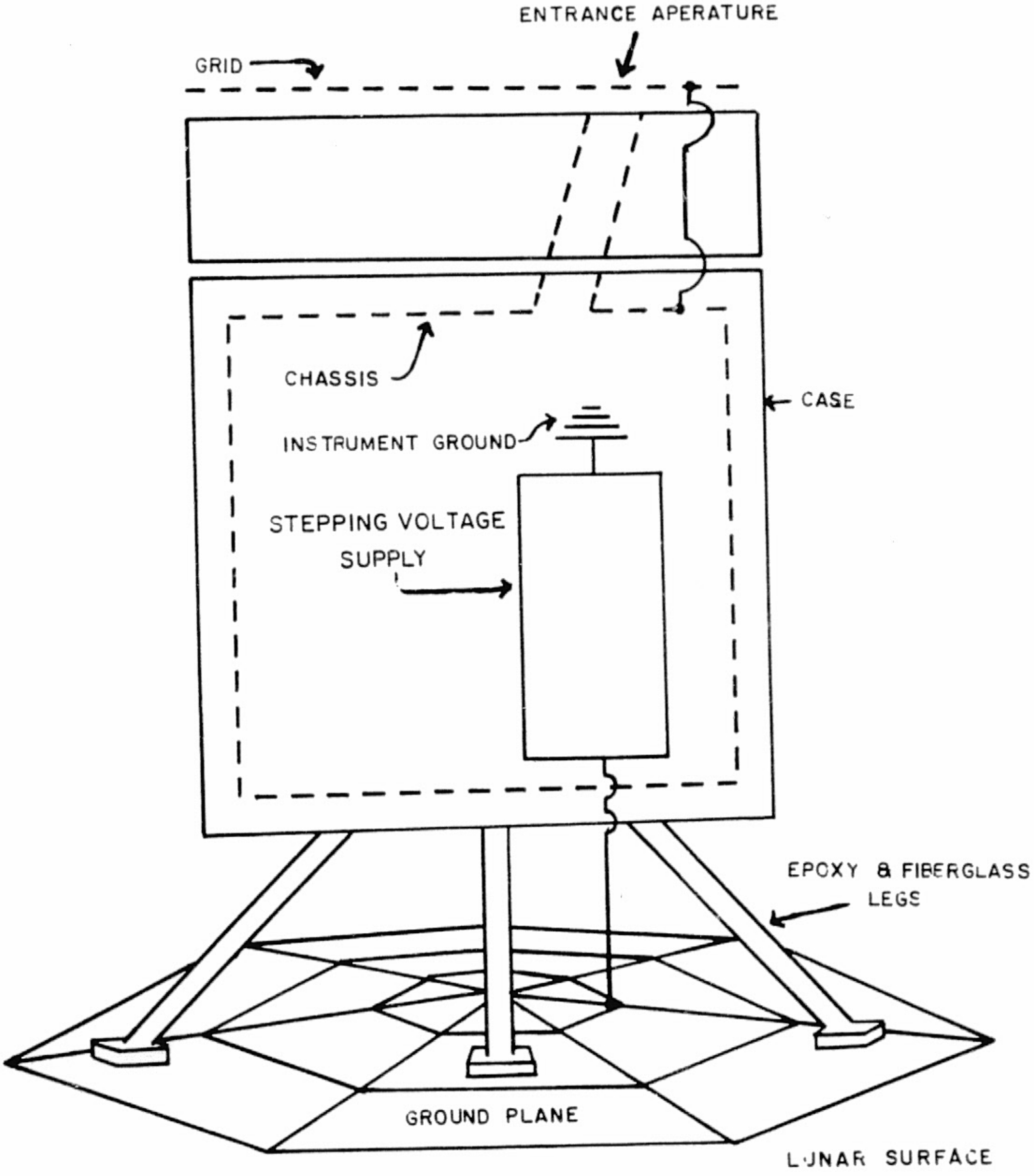
ENTRANCE APERATURE
GRID
CHASSIS
CASE
INSTRUMENT GROUND
STEPPING VOLTAGE SUPPLY
EPOXY & FIBERGLASS LEGS
GROUND PLANE
LUNAR SURFACE

Figure 2-7

proton would not be detected due to the +10 V potential at the entrance aperture. If, on the other hand, the voltage supply maintained a -10 V potential on the grid, with respect to the ground plane, the net potential seen by an incoming 10 eV proton would be zero and it would enter the detector as a 10 eV particle and would be counted as such. This connection between the lunar surface and the instrument through the stepping voltage supply can also be used to determine the value of the lunar surface potential. If we assume that the ambient lunar atmosphere consists of essentially thermal ions (energy 0 eV) then as the ground plane is stepped through various voltages, the ions will begin to appear in the energy channel corresponding to the absolute difference between the lunar surface potential and the voltage on the grid. For example, if the voltage on the grid is -20 V and particles show up in the 10 eV/q channel, then we can expect that if these particles were indeed from the ambient lunar atmosphere, having almost no energy initially, that the lunar surface potential is about +10 V.

The usefulness of the ground plane stepper in determining the lunar surface potential has been demonstrated by Fenner et al. [1973], and it has been determined that a potential of about +10 V is appropriate for the dayside of the moon. Based on data collected near the terminators a value of about -100 V has been set for the night side. Figure 2-8 shows the

Figure 2-8. Results of determination of the lunar surface potential in two regions of the orbit. [Fenner et al. (1973)].

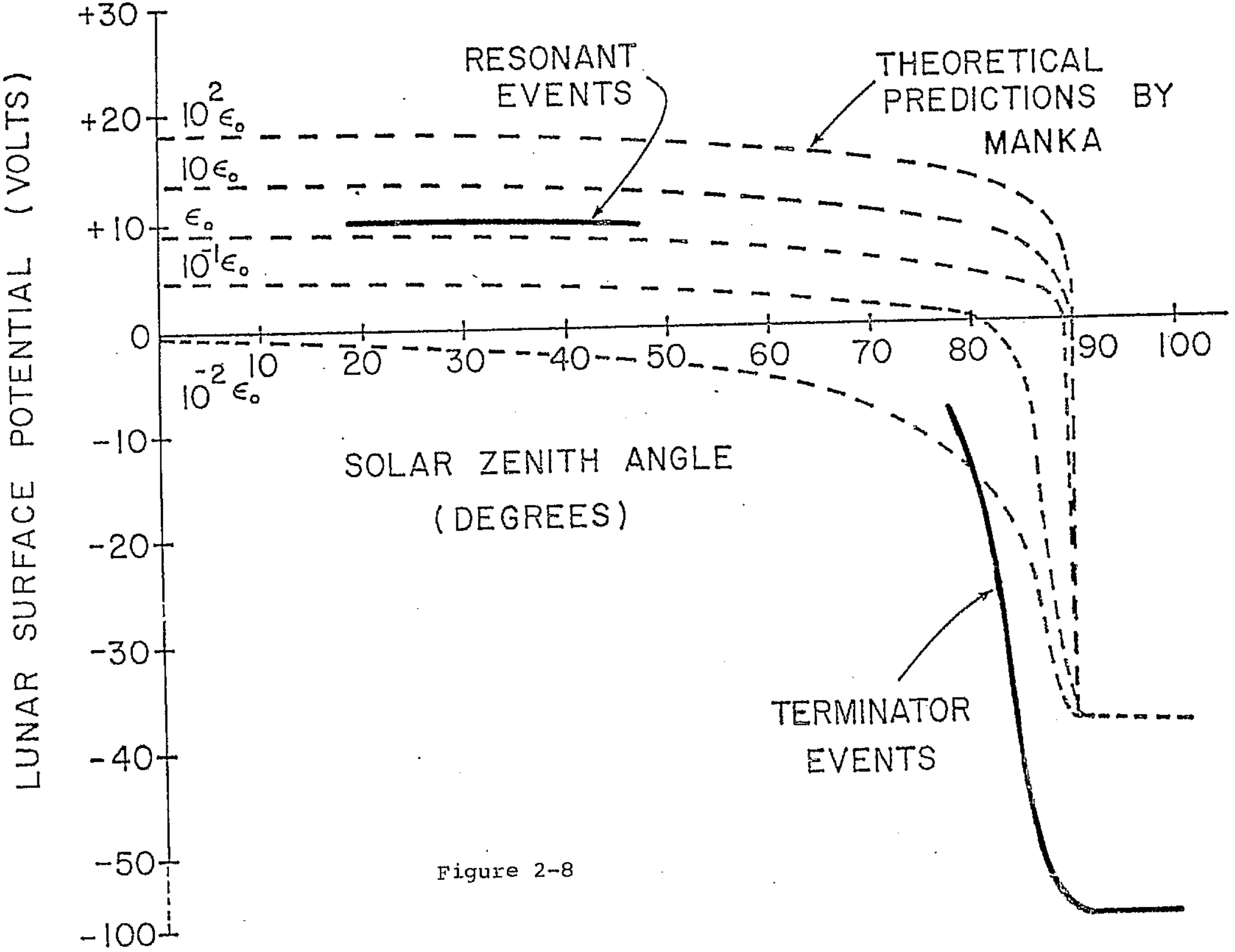
LUNAR SURFACE POTENTIAL (VOLTS)
+30
+20
+10
0
-10
-20
-30
-40
-50
-100
$10^2\epsilon_0$
$10\epsilon_0$
ϵ_0
$10^{-1}\epsilon_0$
$10^{-2}\epsilon_0$
10
20
30
40
50
60
70
80
90
100
RESONANT EVENTS
THEORETICAL PREDICTIONS BY MANKA
SOLAR ZENITH ANGLE (DEGREES)
TERMINATOR EVENTS

Figure 2-8

lunar surface potential data thus far obtained. Theoretical predictions of this potential, based on various values of photoelectric emissivity of the lunar surface, have been made by Manka [1972] and these theoretical predictions are also displayed in figure 2-8.

2.4 Flux measurement

The counting rate R, which is the quantity actually available from SIDE data, can be converted into a more useful quantity, namely the unidirectional differential energy flux $j(\xi,\Omega)$.

The counting rate at energy ξ is given by,

$$R = \int_{\xi} \int_{\Omega} g(\xi, \theta, \phi) j(\xi, \theta, \phi) d\theta \, d\phi \, d\xi \qquad 2\text{-}13$$

where,

$g(\xi, \theta, \phi)$=unidirectional geometric factor at energy ξ

and

$j(\xi, \theta, \phi)$=unidirectional differential flux

If we assume that the flux is independent of θ and ϕ over the solid angle of the detector's field of view so that $j(\xi, \theta, \phi)$ is approximately constant, then,

$$\begin{aligned} R &= \int_{\xi} j(\xi, \theta, \phi) \int_{\Omega} g(\xi, \theta, \phi) d\theta \, d\phi \, d\xi \\ &= \int_{\xi} j(\xi, \Omega) G(\xi) d\xi \end{aligned} \qquad 2\text{-}14$$

where,

$$G(\xi) = \int_{\Omega} g(\xi, \theta, \phi)\, d\Omega = \Xi(\xi)\ \epsilon(\xi) \qquad 2\text{-}15$$

and $\Xi(\xi) = A_{eff}(\xi)\ \Omega_{eff}(\xi)$ and $\epsilon(\xi)$=counter efficiency. A_{eff} is the effective area of the entrance aperture as seen by an incoming particle and Ω_{eff} is the effective solid angle. If we also assume that the flux is constant over the energy bandwidth of the detector, then

$$R = j(\xi, \Omega) \int_{\xi} G(\xi)\, d\xi$$

$$R = j(\xi, \Omega)\ G_o \qquad 2\text{-}16$$

$$G_o = \int_{\xi} G(\xi)\, d\xi \qquad (\mathrm{cm}^2\ \mathrm{ster\ eV})$$

where the integration is carried out over the energy bandwidth.

Therefore, the unidirectional differential flux at energy ξ is given by,

$$j(\xi, \Omega) = R/G_o \qquad (\mathrm{cm}^{-2}\, \mathrm{sec}^{-1}\, \mathrm{ster}^{-1}\, \mathrm{eV}^{-1}) \qquad 2\text{-}17$$

likewise, the omnidirectional differential energy flux is,

$$j_{omni} = \int_{\Omega_{space}} j_{uni}\, d\Omega \qquad \left(\frac{\#\ \text{particles}}{\text{cm}^2\ \text{sec eV}}\right) \qquad 2\text{-}18$$

The corresponding integral fluxes are,

$$J_{uni} = \int_{E_{spectrum}} j_{uni}\, dE \qquad \left(\frac{\#\ \text{particles}}{\text{cm}^2\ \text{sec str}}\right) \qquad 2\text{-}19$$

and

$$J_{omni} = \int_{\Omega_{space}} J_{uni}\, d\Omega \qquad \left(\frac{\#\ \text{particles}}{\text{cm}^2\ \text{sec}}\right) \qquad 2\text{-}20$$

Figure 2-2 shows the results of the geometric factor calibration for the Apollor XIV instrument [Lindeman, 1973].

2.5 Deployment

The SIDE is part of a group of experiments, known as the Apollor Lunar Surface Experiments Package (ALSEP), designed to investigate various phenomena associated with the moon itself and its interaction with the solar wind and the earth's magnetosphere. SIDE's have flown on three Apollo missions; all were successfully deployed and all are still operating at the time of this writing.

The Apollo XII site is located at about 3°S latitude and 23°W longitude in Oceanus Procelarum (Sea of Storms). The Apollo 12 SIDE was placed on the lunar surface by Alan Bean and Charles Conrad during the first EVA which began at about 6 a.m. EST November 19, 1969.

The Apollo XIV mission took place in early 1971, resulting in the placement of the Apollo 14 SIDE on the lunar surface at about 3°S latitude and 17°W longitude in the Fra Mauro formation. Alan Shepard and Ed Mitchell deployed the ALSEP on their first EVA which began about 9 a.m. EST, February 5, 1971.

The Apollo XV SIDE was deployed by Dave Scott and James Irwin in the Hadley-Apennine region of the moon at about 26°N latitude and 3°E longitude again during the first EVA which began about 8 a.m. EST July 31, 1971.

Figure 2-9 shows the positions of the lunar surface of the landing sites and their seleonographic coordinates. Photographs of the three instruments are shown in figure 2-10.

The Apollo 12 and 14 SIDE's were equipped with a bubble leveling device attached to the top of the instrument that allowed the astronauts to align the vertical axis of the SIDE with the local vertical to within a 5° accuracy so that the look direction of the detector is approximately in the ecliptic plane. The Apollo 15 instrument was equipped with an adjustable leg that allowed compensation for the high latitude

Figure 2-9. Seleonographic locations of Apollo 12, 14 and 15 ALSEP sites.

Figure 2-10. From left clockwise, photographs of Apollo 12 and 14 SIDE's deployed on the lunar surface, Apollo 15 SIDE in the lab. [after Medrano, 1973].

MOON

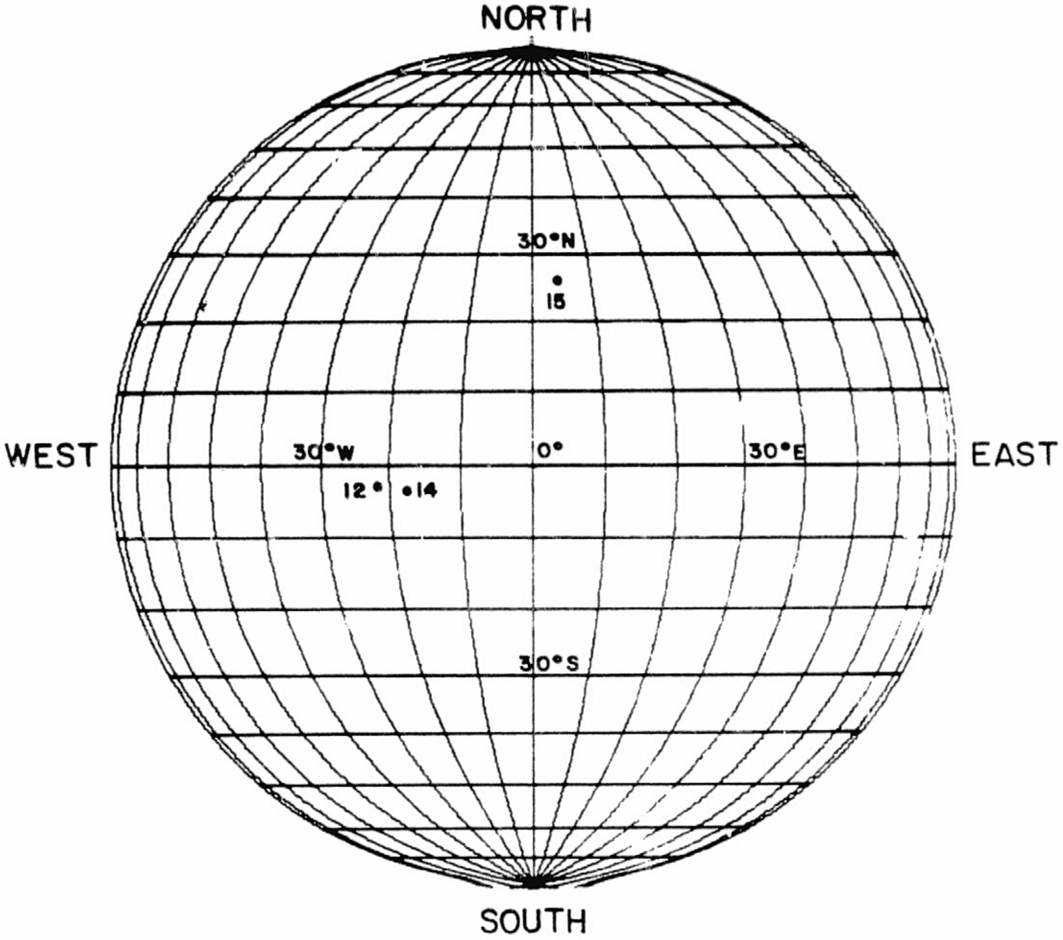

	LONG	LAT	M	D	Y
APOLLO 12	23.4W	3.2S	11	19	69
APOLLO 14	17.4W	3.6S	2	5	71
APOLLO 15	3.6E	26.1N	7	31	71

Figure 2-9

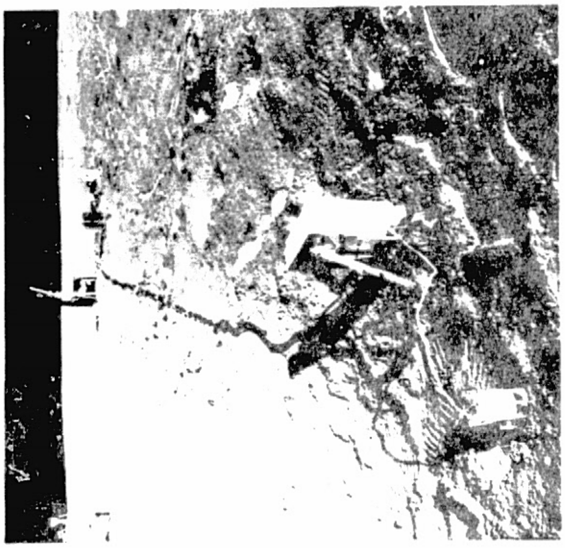

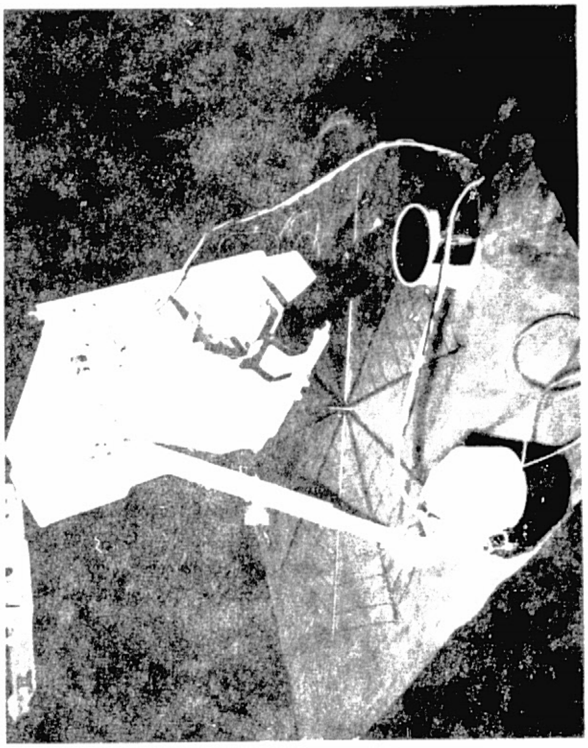

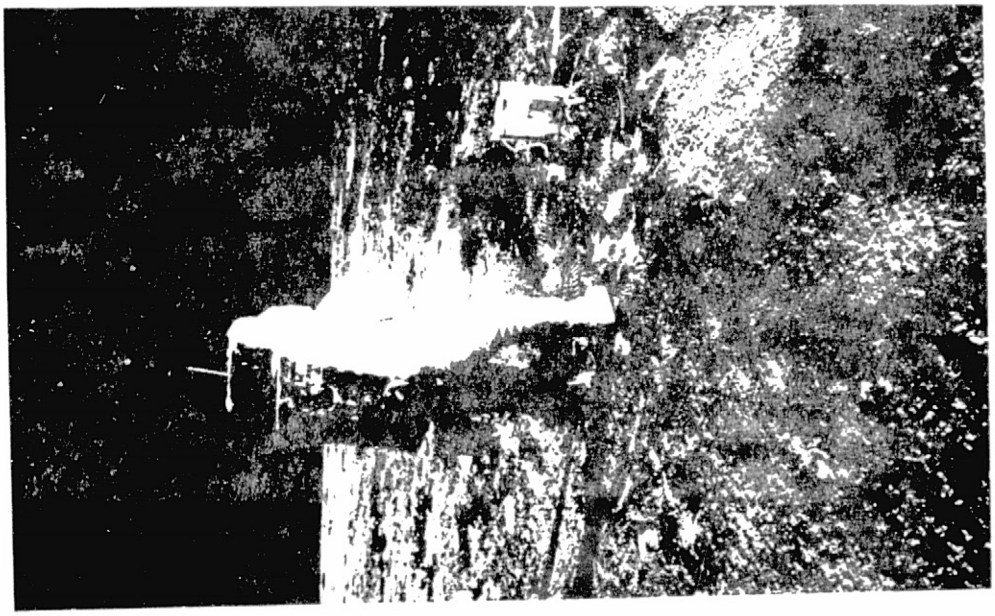

deployment so that its detector look direction is also approximately in the plane of the ecliptic. (see figure 2-11a)

The look direction of the actual detector in each of the instruments is at a 15° angle from the instrument x-axis, which coincides with the local vertical at the ALSEP site for the 12 and 14 instruments. This 15° offset determines the actual look direction, in longitude, with respect to the moon. The configuration in longitude is illustrated in figure 2-11b. Figure 2-12 shows the body axes of the three instruments. The relationship of the body axes to the local coordinate system at ALSEP is as follows.

The local coordinate system is known as system 1, and in the discussion in chapter 4, it is referred to as S'''. It is defined by an x-axis that is aligned with the local vertical at ALSEP, a z-axis that is perpendicular to the x-axis and directed northward along the meridian of deployment. The y-axis completes the orthogonal right handed system. That is, y points east.

In the case of the Apollo 12 and 14 SIDE's the body x-axis of the instrument coincides with the x-axis of system 1. The body x-axis of the 15 instrument is in the plane of the meridian of deployment but tilted southward by 26°. The body y-axis of the 15 instrument coincides with the y-axis of system 1 and the z-axis is orthogonal to x and y. The body z-axis of the 14 instrument coincides with system 1, but the body

Figure 2-11. a. shows the configuration in latitude of Apollo's 14 and 15. Apollo 12 is approximately represented by the drawing for Apollo 14.

Figure 2-11. b. shows the configuration in longitude of all three SIDE's. Apollo 14 SIDE looks most nearly toward earth.

Figure 2-12. Relationship of the instrument body axes to the local ALSEP coordinate system 1.

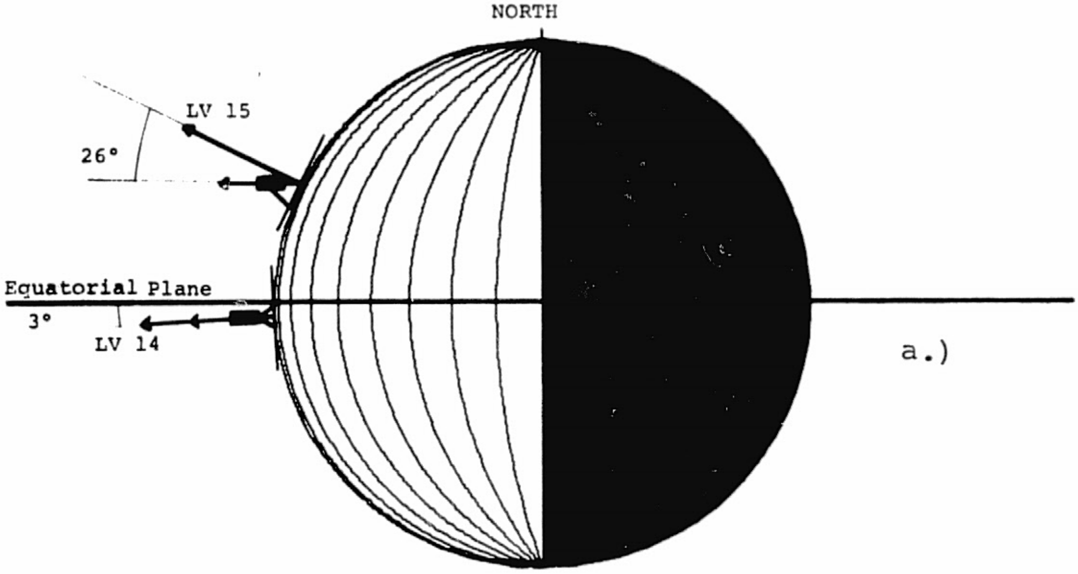

Time=Lunar Noon

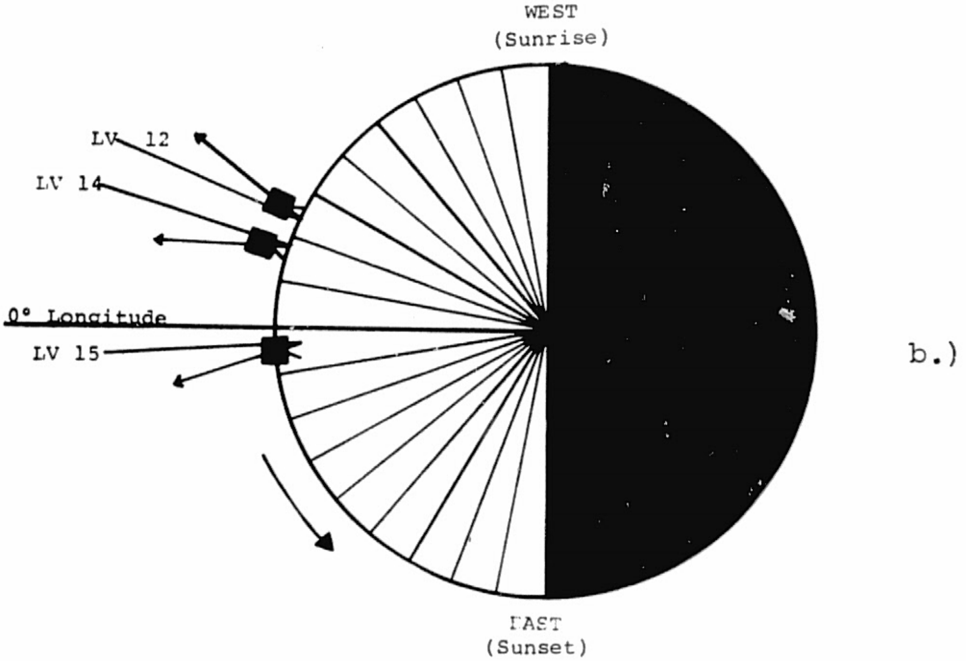

LV=Local Vertical

Figure 2-11

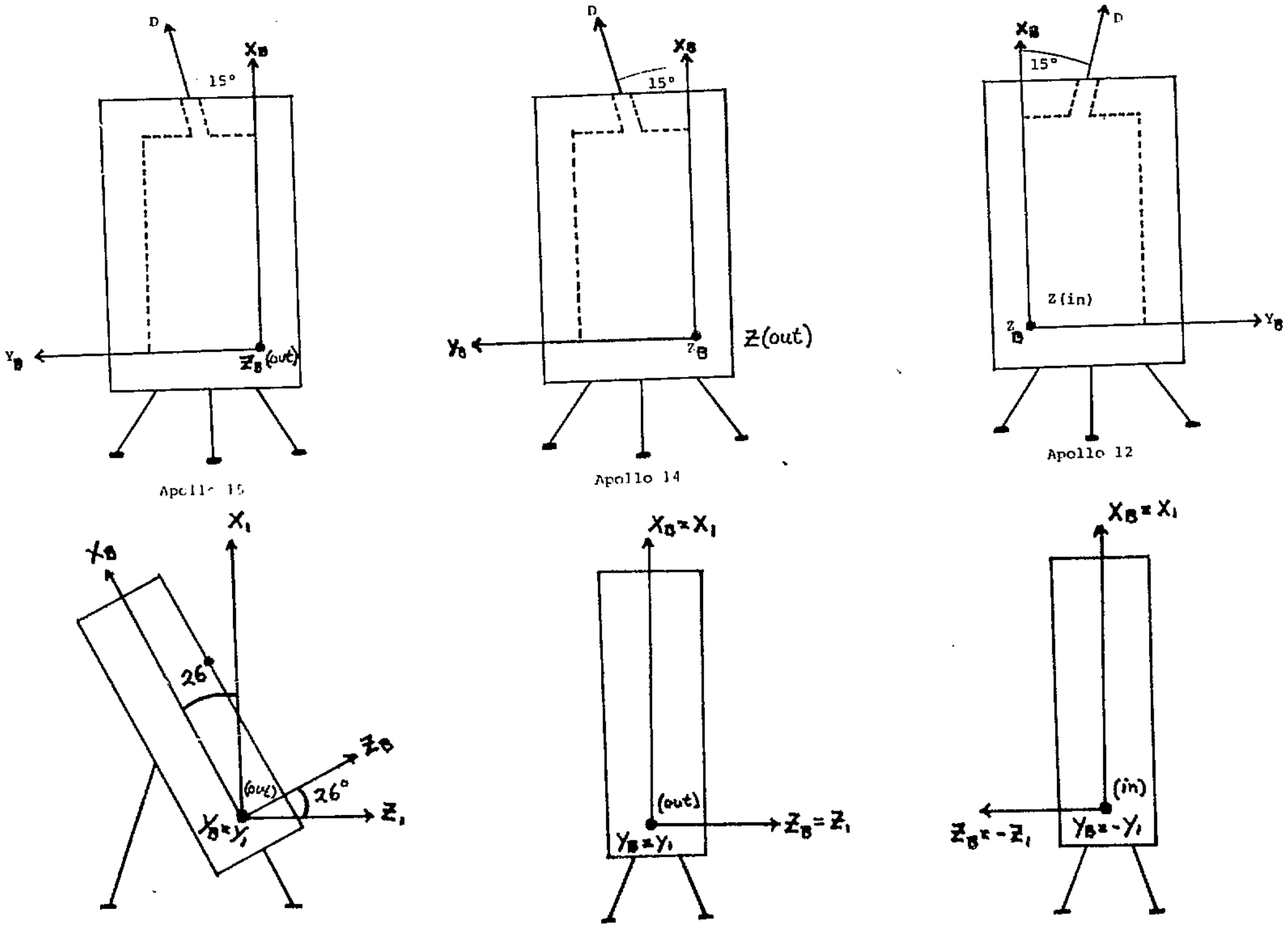
D
X_B
15°
Y_B
Z_B (out)
Apollo 15
D
X_B
15°
Y_B
Z_B
Z(out)
Apollo 14
X_B
D
15°
Z(in)
Z_B
Y_B
Apollo 12
X_B
X_1
26
(out)
Z_B
26°
Z_1
Y_B = Y_1
X_B = X_1
(out)
Z_B = Z_1
Y_B = Y_1
X_B = X_1
(in)
Z_B = -Z_1
Y_B = -Y_1

Figure 2-12

y- and z-axes of the 12 SIDE are the negatives of system 1.

For further discussion of the relation of the body axes to other relevant coordinate systems, see chapter 4 and Hills [1969].

The deployment of the instruments in this fashion allows a directional sampling of magnetospheric and solar wind particles at any given time. The look directions of the three detectors for various positions in the lunar orbit are shown in figure 2-13. Note that the Apollo 14 SIDE looks almost directly back at the earth at any position in the orbit, which makes this instrument particularly suitable for the observation of particles streaming outward from the earth's bow shock. Because of the excessively high background counting rate in the Apollo 15 instrument and the discontinuous nature of the Apollo 12 data for the period of interest in this thesis, only data from the Apollo 14 SIDE were used.

2.6 <u>Magnetometer</u> [Colburn, 1969]

The data on the interplanetary magnetic field and those from the geomagnetic field were collected by the NASA Ames magnetometer onboard the Explorer 35 satellite which achieved lunar orbit on July 17, 1967 with a periselene of 1.4 R_L (lunar radii), an aposelene of 5.4 R_L and an orbital period of 11.5 hours.

The magnetometer contains three orthogonal fluxgate sen-

Figure 2-13. Longitudinal look directions of the three SIDE's for various positions in lunar orbit. Note that the Apollo 14 SIDE looks most nearly toward earth. Different sunset and sunrise times are due to the difference in longitude of deployment. [Hills et al. (1971)].

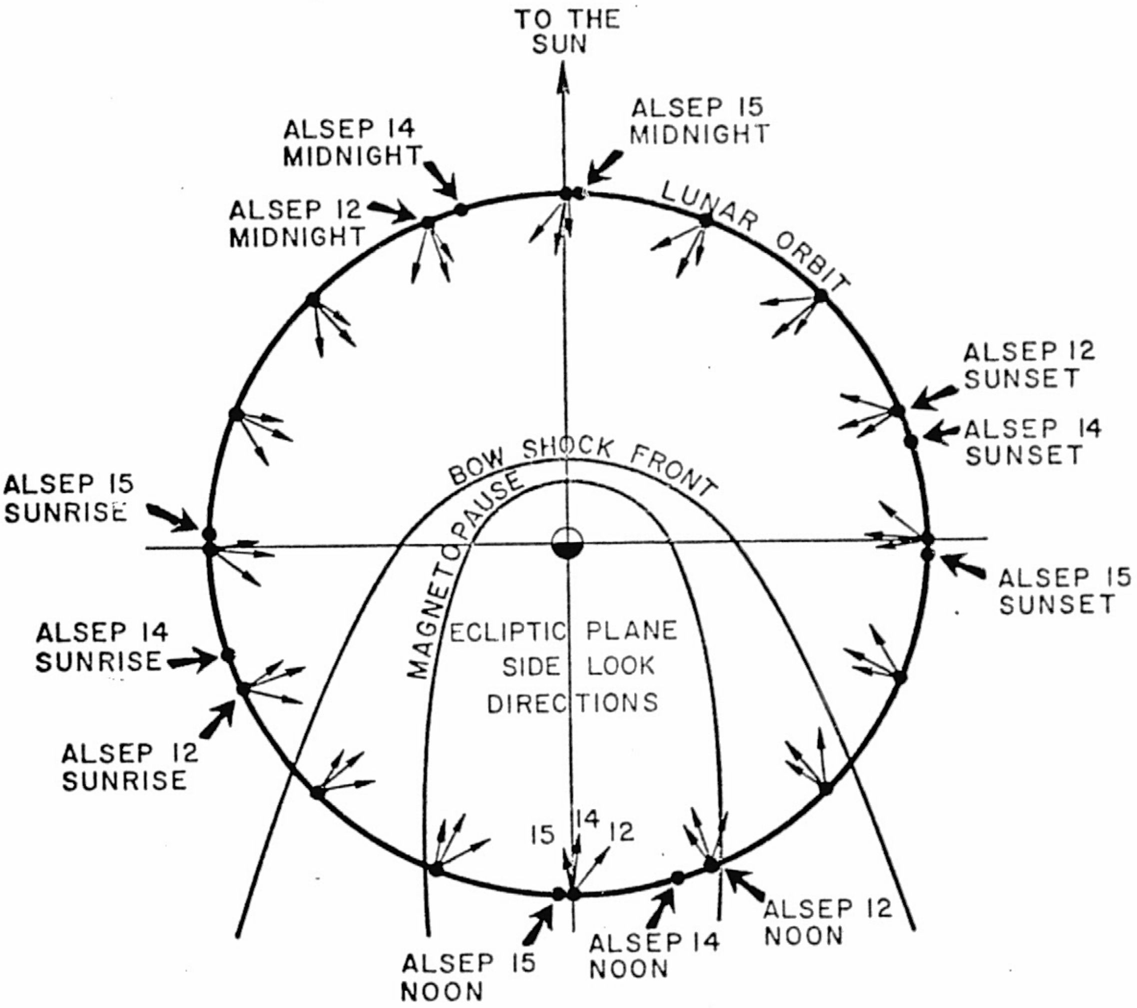
TO THE SUN
ALSEP 14 MIDNIGHT
ALSEP 15 MIDNIGHT
ALSEP 12 MIDNIGHT
LUNAR ORBIT
ALSEP 12 SUNSET
ALSEP 14 SUNSET
BOW SHOCK FRONT
ALSEP 15 SUNRISE
MAGNETOPAUSE
ALSEP 15 SUNSET
ALSEP 14 SUNRISE
ECLIPTIC PLANE SIDE LOOK DIRECTIONS
ALSEP 12 SUNRISE
15
14
12
ALSEP 12 NOON
ALSEP 14 NOON
ALSEP 15 NOON

Figure 2-13

sors which measure the ambient magnetic field in the neighborhood of the spacecraft and a vector measurement of the field is obtained every 6.14 seconds in the 20 gamma range. The signals from the sensors are spin-demodulated onboard to provide a vector in a fixed spacecraft coordinate system, with the final data available from Ames in Solar Equatorial or Solar Magnetospheric coordinates, averaged over 81.8 second intervals.

The data are further processed on the SDS 910 computer at Rice to provide the field components in Solar Ecliptic coordinates, [Lindeman,1972].

The solar ecliptic coordinate system is defined as follows. The x-axis is defined by the earth-sun line with positive x toward the sun. The z-axis is normal to the plane of the ecliptic and positive z is toward north. North is the direction defined by the direction of the orbital angular momentem vector of the earth. y completes the right-handed system. Solar ecliptic longitude is defined as

$$\phi = \tan^{-1}\left(y/x\right) \qquad 2\text{-}21$$

and solar ecliptic latitude is defined as

$$\theta = \tan^{-1}\ (z/(x^2 + y^2)^{1/2}) \qquad 2\text{-}22$$

Due to a failure in the sun sensor in the spinning spacecraft, the values of the solar ecliptic longitude are often in error. It is possible, however, to get a rough correction for this error by observing the longitude data in the geomagnetic tail region where stable neutral sheet crossings are observed.

If a neutral sheet crossing occurs when the spacecraft is near 180° in longitude, one would expect that while in the southern lobe of the field, the solar ecliptic longitude of the field would be about 180° and after the crossing, the field would have a longitude of approxiamtely 0°. By observing the actual measured values and knowing the nominal values of the field longitude, the correction angle can be determined. An example of this is shown in figure 2-14 where a correction angle of about 28° was obtained for the lunation with which this thesis is concerned. For the present analyses, the uncorrected values of the longitude were used. Any physical implications of using these uncorrected longitudes are discussed in chapter 5. It should also be noted that the Explorer 35 magnetometer has no onboard recorder and therefore there are frequent data gaps of about 5 hours during each orbit due to the passage of the satellite behind the moon.

2.7 Other lunar surface experiments

The SIDE is only one of a variety of instruments designed to investigate plasma properties in the vicinity of the moon. These other lunar surface experiments provide data which can potentially be correlated with SIDE observations.

Figure 2-14. Solar ecliptic longitude of the magnetic field near the anti-solar position in lunar orbit. The technique for determining the correction angle is illustrated.

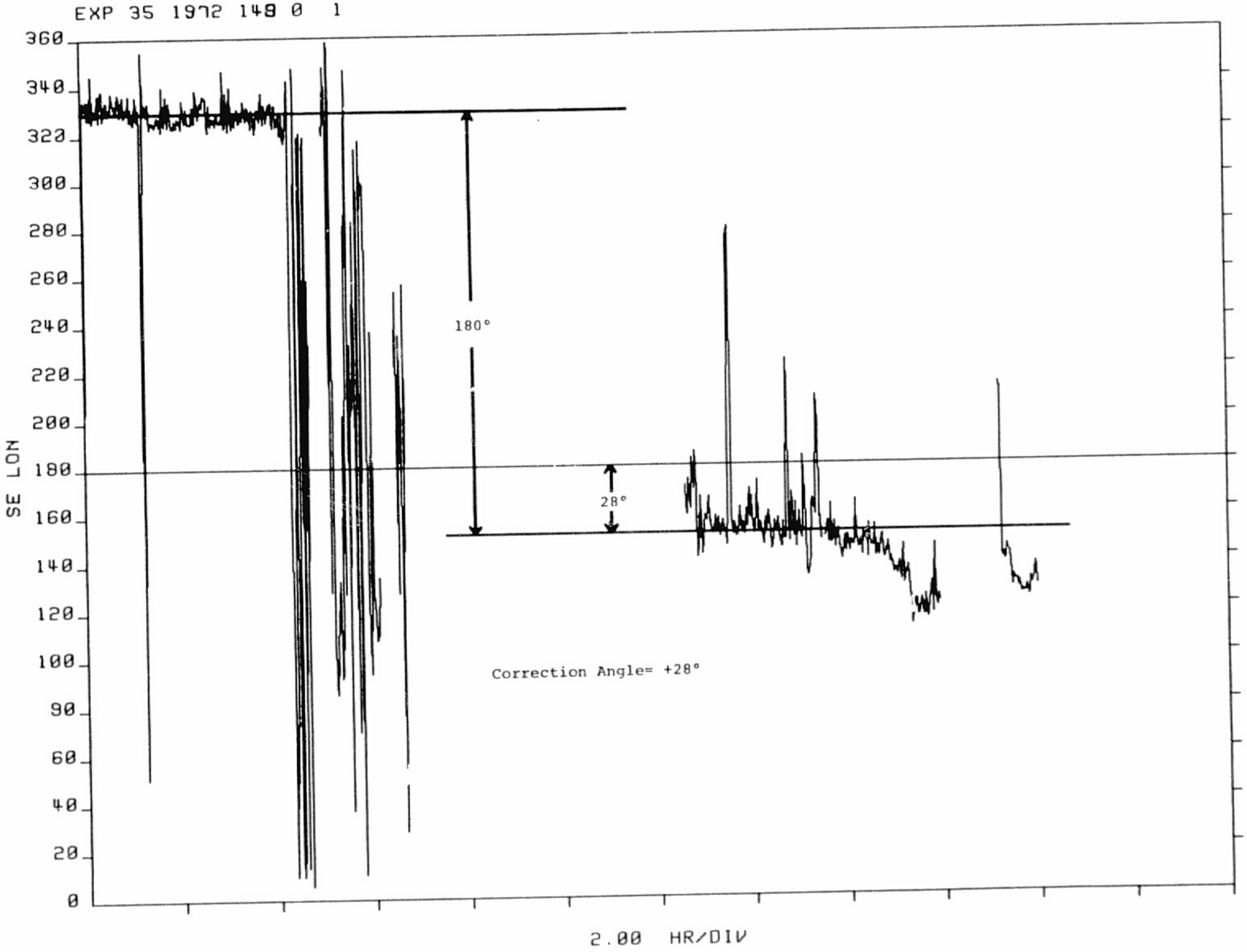
EXP 35 1972 148 0 1
360
340
320
300
280
260
240
220
200
180
160
140
120
100
90
60
40
20
0
SE LON
180°
28°
Correction Angle= +28°
2.00 HR/DIV

Figure 2-14

Although detailed discussions of these other experiments are beyond the scope of this thesis, the descriptions below are included to provide an insight into the flavor of the particles and fields research being conducted on the lunar surface.

2.8 CPLEE-Charged Particle Lunar Environment Experiment

The CPLEE consists of two charged particle analyzers, each containing five C-shaped channeltrons as negatively charged particle detectors and one channeltron as a positively charged particle detector, with electrostatic deflection plates providing the energy discrimination capability. Particles with energies from 50 eV to 50 keV can be detected by CPLEE from two directions simultaneously; one analyzer looks vertically with a 4°X20° field of view and the other detector is directed at 60° from the local vertical with the same field of view.

The CPLEE has observed such phenomena as a photoelectron layer at the lunar surface, solar wind particles and penetration of particles of auroral energies to lunar distances in the geomagnetic tail [O'Brien, 1971].

2.9 CCGE-Cold Cathode Gauge Experiment [Johnson et al., 1971]

The cold cathode gauge experiment is designed to measure the neutral gas pressure of the lunar atmosphere. The instrument is attached to the SIDE and is connected to the ALSEP central station through the SIDE, but it is a separate experiment consisting of a chamber in which a spool shaped cathode is connected to an electrometer. The cathode is surrounded by a cylindrical anode that is held at +4500 volts. When neutral gas enters the chamber, a self sustaining discharge occurs with the ion current through the cathode being a measure of the gas pressure.

Results from the CCGE set neutral gas number densities for lunar nightime of about 10^5 cm^{-3} and about 10^7 cm^{-3} for daytime with the daytime value partly due to local experiment outgassing.

2.10 LSM-LPM-Lunar Surface Magnetometer and Lunar Portable Magnetometer. [Dyal et al., 1972]

The lunar surface magnetometers each consist of three orthogonal fluxgate sensors, mounted on booms, with the electronics package located at the junction of the booms. This configuration provides a vector measurement of the static as well as the time varying magnetic fields at the ALSEP sites.

The lunar portable magnetometers are self contained and also provide vector measurements of the field at several different locations along the astronaut traverses. Table 2-2 shows the range and sensitivity of the Apollo 16 LSM and LPM [Dyal et al., 1972]. Several of these magnetometers have flown on Apollo missions and a summary of the preliminary

Apollo 16 Magnetometer Characteristics

Parameter	*Value*
Range, γ	0 to ± 200 0 to ± 100 0 to ± 50
Resolution, γ	±0.1
Frequency response	dc to 3 Hz
Angular response	Proportional to cosine of angle between magnetic field vector and sensor axis
Sensor geometry	3 orthogonal sensors at the ends of 100-cm booms; orientation determination to within 1° in lunar coordinates
No. of commands	
Ground	10
Spacecraft	1
Analog zero determination	180° flip of sensor
Internal calibration, percent of full scale	0, ±25, ±50, and ±75
Field bias offset capability, percent of full scale	0, ±25, ±50, and ±75
Modes of operation	Orthogonal field measurements, gradient measurement, internal calibration
Average power, W	
Day	3.5
Night	9.4
Weight, kg	8.9
Size, cm	25 by 28 by 63
Operating temperature, °K	223 to 358

Apollo 16 LPM Characteristics

Parameter	*Value*
Sensor	3 orthogonal fluxgate sensors
Range, γ	-256 to +256
Resolution, γ	±1.0
Frequency response	dc to 0.05 Hz
Battery lifetimes:	
Electronics, hr	8
Display, min	20
Mass, kg	4.6
Size, cm	56 by 15 by 14
Operating temperature, °K	273 to 323

Table 2-2

ORIGINAL PAGE IS
OF POOR QUALITY

Summary of Lunar Surface Magnetic Field Measurements

Site	*Coordinates, deg*	*Field magnitude, γ*	*Magnetic field components, γ*		
			B_{up}	B_{east}	B_{north}
Apollo 16 [a]					
ALSEP site	8.9 S 15.5 E	231	-174	-73	134
Site 2		180	-179	-10	19
Site 5		125	120	-25	-25
Site 13		313	-141	-209	-186
Final Rover parking site		121	-42	-93	66
Apollo 15 ALSEP site	26.1 N 3.7 E	6 ± 4	4 ± 4	1 ± 3	4 ± 3
Apollo 14 landing site	3.7 S 17.5 W				
Site A		103 ± 5	-93 ± 4	38 ± 5	-24 ± 5
Site C		43 ± 6	-15 ± 4	-36 ± 5	-19 ± 8
Apollo 12 ALSEP site	3.2 S 23.4 W	38 ± 2	-25.8 ± 1.0	11.9 ± 0.9	-25.8 ± 0.4

[a] The error in all components of the Apollo 16 field readings is ±25 γ. These limits will be reduced after further data reduction.

Table 2-3

Estimated ^4He Flux Averages During the Times of Foil Exposure

Mission	Exposure initiation		Exposure duration, hr:min	Average solar wind ^4He flux, $10^6 cm^{-2} sec^{-1}$
	Date	G.m.t., hr:min		
Apollo 11	July 21, 1969	03:35	01:17	6.2 ± 1.2
Apollo 12	Nov. 19, 1969	12:35	18:42	8.1 ± 1.0
Apollo 14	Feb. 5, 1971	15:15	21:00	4.2 ± 0.8
Apollo 15	July 31, 1971	19:36	41:08	17.7 ± 2.5
Apollo 16	Apr. 21, 1972	23:01	45:05	12.0 ± 1.8

Solar Wind Abundance Ratios Determined From the Foil Exposure Periods of the Apollo Missions

Mission	$^4He/^3He$	$^4He/^{20}Ne$	$^{20}Ne/^{22}Ne$	$^{22}Ne/^{21}Ne$
Apollo 11	1860 ± 140	430 ± 90	13.5 ± 1.0	–
Apollo 12	2450 ± 100	620 ± 70	13.1 ± 0.6	26 ± 12
Apollo 14	2230 ± 140	550 ± 70	13.65 ± 0.50	–
Apollo 15	2310 ± 120	550 ± 50	13.65 ± 0.30	31 ± 4
Apollo 16	2260 ± 100	570 ± 50	13.80 ± 0.40	31 ± 4

Preliminary Results on Argon Abundances in the Solar Wind

Mission	$^{20}Ne/^{36}Ar$
Apollo 14[a]	37^{+10}_{-5}
Apollo 15	20^{+8}_{-5}
Apollo 16	29 ± 6

First Results From the Analyses of the Aluminum Foil From the Apollo 16 SWC Experiment

Sample no.	Area, cm^2	^4He concentration, 10^{10} atoms/cm^2	$^4He/^3He$	$^4He/^{20}Ne$	$^{20}Ne/^{22}Ne$	$^{22}Ne/^{21}Ne$	$^{20}Ne/^{36}Ar$
Apollo 16:							
[a]2-1	5.02	108	2290	510	14.0	32	29
2-2	4.98	107	2300	490	13.9	27	30
[a]2-3	5.04	101	2280	500	13.5	31	27
2-4	5.17	108	2280	490	13.7	27	31
[a]2-5	10.35	100	2310	490	13.9	35	28
Apollo 15:							
[a]3-9	3.13	140	2370	480	13.8	33	19

Table 2-4

results of ambient field measurements at different locations is shown in table 2-3.

2.11 SWCE-Solar Wind Composition Experiment [Geiss et al., 1972]

The SWCE is one of the simpler lunar surface experiments and consists of exposing an aluminum foil strip, 30X140 cm, directly to the solar wind and then returning the foil to the laboratory for analysis. The foil is baked out in a vacuum chamber and in some cases melted to release the trapped solar wind particles which are subsequently analyzed with a mass spectrometer. The SWCE was one of the experiments flown on the Apollo 11 mission as well as several others and a summary of the results from these missions is shown in Table 2-4.

2.12 SWS-Solar Wind Spectrometer [Synder et al., 1970]

The solar wind spectrometer was designed to investigate properties of the solar wind and its interaction with the moon. It consists of seven symmetrically arranged Faraday cups, one directed vertically, and the other six at 60° angles from the vertical. This configuration allows observation of any solar wind anisotropies that may exist. Energy spectra may be obtained by modulating the voltage on the grids that precede the Faraday cups and noting the cup current changes. The SWS cycles through 14 energy steps ranging from 10 eV to

10.4 keV for protons and from 10 eV to 1480 eV for electrons in the high energy range and each energy step is reduced by a factor of 1.68 in the low energy range.

Solar wind proton spectra obtained in this way show proton velocities of typically 400 to 600 km/sec. The SWS does not generally see solar wind particles during the lunar night, indicating a plasma void behind the moon.

The power for all of the experiments described, with the exception of the LPM and the SWCE is provided by a Radioisotope Thermoelectric Generator (RTG) which provides a continuous 70 W. The individual experiments are connected to the ALSEP Central Station by Mylar coated ribbon-like cables where the data from each of them are collected and transmitted to earth through a high gain antenna mounted atop the central station and aimed at the earth. These data are received at various earth based tracking stations,recorded on magnetic tape and distributed by NASA to the various investigators.

Chapter 3

This chapter is a description of the model used to study the behavior of suprathermal protons that are ejected into the solar wind in an upstream direction from the earth's bow shock.

3.1 Equations of motion

Consider a particle being ejected from the earth's bow shock with some initial velocity $\vec{V}_p$ and define a coordinate system in which the z-direction is parallel to the interplanetary magnetic field $\vec{B}$, y is in the direction of $-\vec{V}_{sw} \times \vec{B}$ and x completes the right-handed system. If the origin of this coordinate system is fixed at some point on the surface of the shock, then the particle sees an electric field $\vec{E} = -\vec{V}_{sw} \times \vec{B}$, due to the convection of the interplanetary field lines past the earth at the solar wind velocity $\vec{V}_{sw}$.

The equation of motion that describes the particle's trajectory upon leaving the shock is,

$$m\frac{d\vec{V}_p}{dt} = q(\vec{E} + \vec{V}_p \times \vec{B}) \qquad 3\text{-}1$$

In a coordinate system with $\vec{B} = B\hat{z}$, one can choose $\vec{E} = E\hat{y}$ without loss of generality since $\vec{E}$ is always perpendicular to $\vec{B}$. The solution of equation 3-1 gives the time dependent coordinates of the particle trajectory.

$$x(t) = \left(\frac{v_{xo}-v_d}{\omega}\right)\sin\omega t + \frac{v_{yo}}{\omega}(1-\cos\omega t) + v_d t \qquad 3\text{-}2$$

$$y(t) = \frac{v_{yo}}{\omega}\sin\omega t + \left(\frac{v_{xo}-v_d}{\omega}\right)(\cos\omega t-1) \qquad 3\text{-}3$$

$$z(t) = v_{zo}t \qquad 3\text{-}4$$

Equations 3-2 and 3-3 are the parametric equations of a cycloid in the x-y plane. For a derivation and discussion of these equations, see the appendices. The motion in the z-direction is uncoupled to motion in the x-y plane and hence if there is no initial velocity in the z-direction, the particle will move entirely in the x-y plane.

If we transform the above equations to a frame of reference that is moving parallel to the x-direction with velocity V_d, we see that the particle describes circular motion with center,

$$X_c = \frac{mv_{yo}}{qB} \qquad Y_c = \frac{m}{qB}(v_d-v_{xo}) \qquad 3\text{-}5$$

and radius

$$R = (m/qB)\left[(v_{xo}-v_d)^2 + v_{yo}^2\right]^{1/2} \qquad 3\text{-}6$$

in the moving reference frame. That is, the guiding center of the circle moves in the x-direction with velocity V_d=E/B, the drift velocity. (see figure 3-1)

Figure 3-1a. Illustration of particle drift motion for a proton in crossed $\vec{E}$ and $\vec{B}$ fields when the initial velocity of the particle is zero.

Figure 3-1b. View of drift motion in the Y_{se}-Z_{se} plane showing the effect of adding a finite z-component of the velocity.

Figure 3-1c. View in the X_{se}-Y_{se} plane showing the particle's resultant guiding center trajectory.

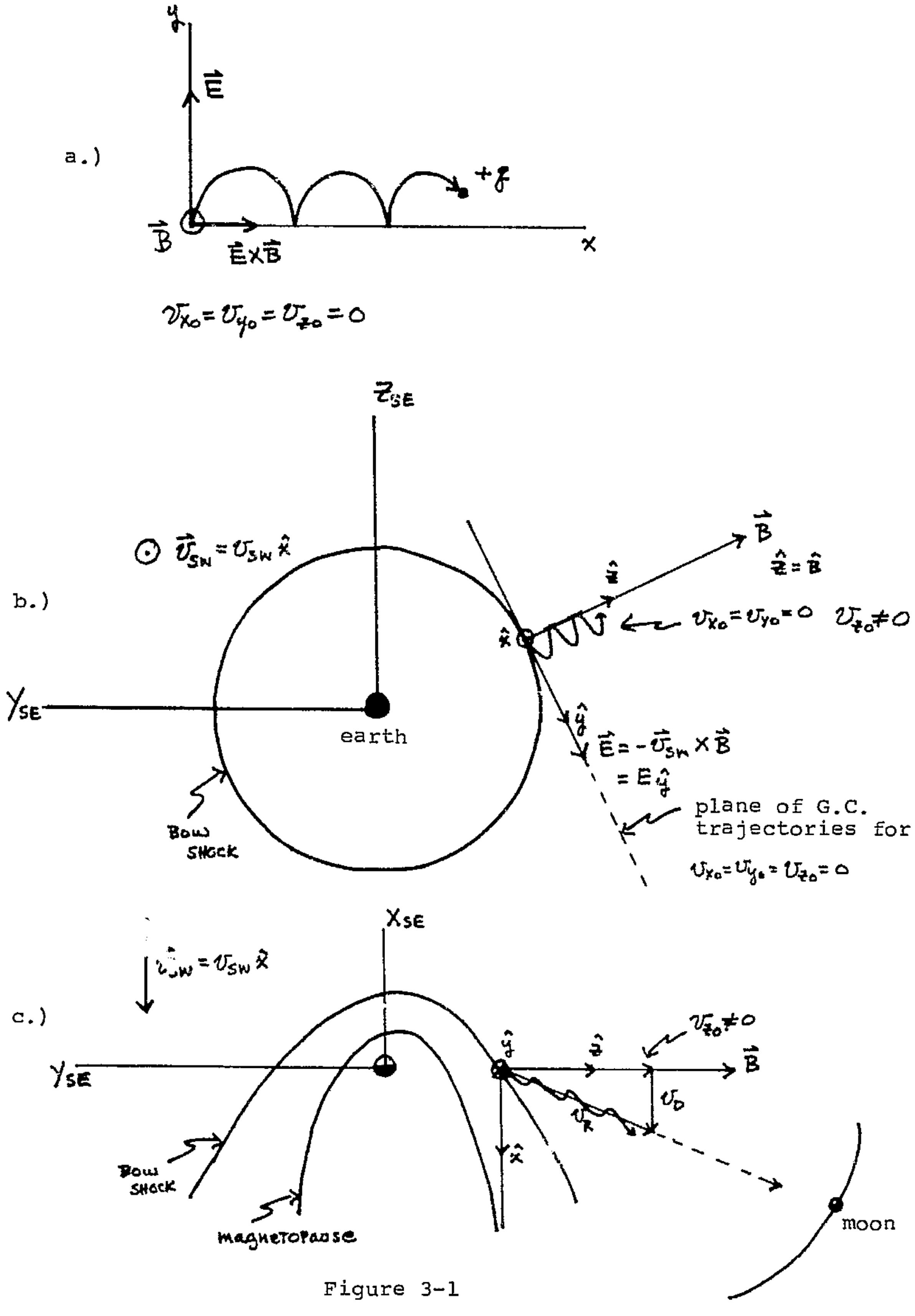
a.)
y
$\vec{E}$
+q
$\vec{B}$
$\vec{E}\times\vec{B}$
x
$v_{x0} = v_{y0} = v_{z0} = 0$
b.)
Z_{SE}
$\vec{v}_{SW} = v_{SW}\hat{x}$
$\vec{B}$
$\hat{z} = \hat{B}$
$\hat{z}$
$\hat{x}$
$v_{x0} = v_{y0} = 0$ $v_{z0} \neq 0$
Y_{SE}
earth
$\hat{y}$
$\vec{E} = -\vec{v}_{SW}\times\vec{B}$
$= E\hat{y}$
plane of G.C. trajectories for
$v_{x0} = v_{y0} = v_{z0} = 0$
Bow shock
c.)
X_{SE}
$\vec{v}_{SW} = v_{SW}\hat{x}$
$v_{z0} \neq 0$
Y_{SE}
$\hat{y}$
$\hat{z}$
$\vec{B}$
v_D
v_R
$\hat{x}$
Bow shock
magnetopause
moon

Figure 3-1

Due to the uncoupling of the z-direction motion from the x-y planar motion, a simple expression can be written that determines the resultant motion of the guiding center of a particle that leaves the earth's bow shock with some intial velocity $\vec{V}_p$. The resultant velocity $\vec{V}_r$ of the particle's guiding center is given by,

$$\vec{V}_r = \vec{V}_{p_{\parallel}} + \vec{V}_d \qquad 3\text{-}7$$

where $\vec{V}_{p_{\parallel}}$ is the component of the particle's initial velocity that is parallel to the interplanetary field and $\vec{V}_d$ is given by,

$$\vec{V}_d = (\vec{E} \times \vec{B})/B^2 \qquad 3\text{-}8$$

3.2 Guiding center behavior

Figure 3-2 is an idealized representation of the magnetospheric cavity as it exists in the free flowing solar wind. In a solar ecliptic coordinate system the interplanetary magnetic field has a solar ecliptic longitude of approximately 315°, the "garden hose angle", and lies more of less in the ecliptic plane.

To understand the basic longitudinal behavior of the model,

Figure 3-2. Diagram demonstrating the asymmetry of the $\vec{E} \times \vec{B}$ drift model and the basic guiding center behavior of a zero pitch angle particle.

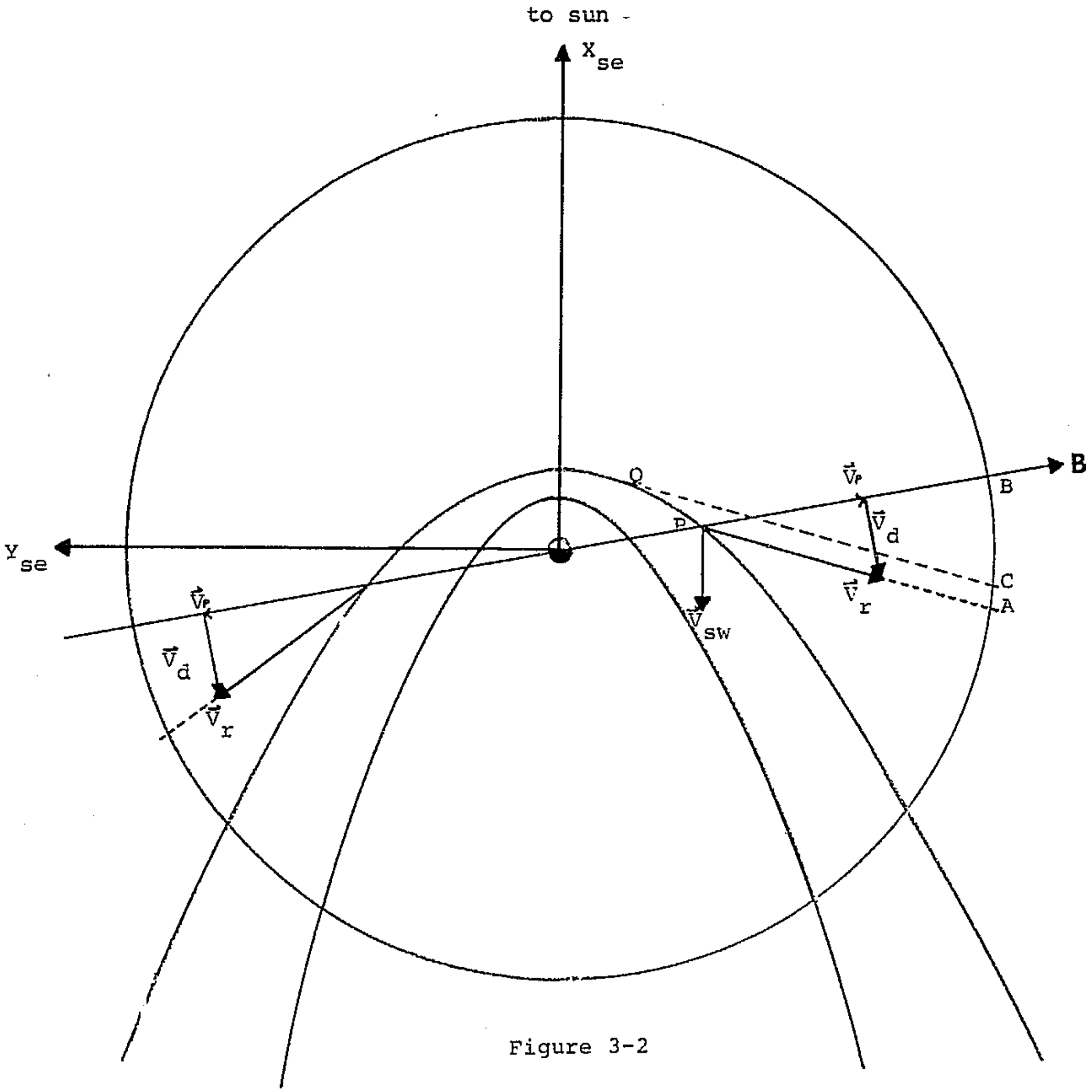
to sun
X_{se}
$\mathbf{B}$
Q
P
B
$\vec{V}_P$
$\vec{V}_d$
$\vec{V}_r$
C
A
$\vec{V}_{sw}$
Y_{se}
$\vec{V}_P$
$\vec{V}_d$
$\vec{V}_r$

Figure 3-2

consider a particle of zero pitch angle leaving the shock at point P in figure 3-2 and traveling along the field line with a velocity $\vec{V}_{p_{\parallel}}$, determined by its initial energy. If the interplanetary field were stationary, the particle would move along the path determined by $\vec{V}_{p_{\parallel}}$ and it would intersect the lunar orbit at point B. Due to the convection of the field lines past the magnetospheric cavity at the solar wind velocty, there exists an interplanetary electric field $\vec{E} = -\vec{v}_{sw} \times \vec{B}$ such that the particle's guiding center follows a path that is determined by,

$$\vec{V}_r = \vec{V}_{p_{\parallel}} + \vec{V}_{sw} - (\vec{V}_{sw} \cdot \hat{B})\ \hat{B} \qquad 3\text{-}9$$

and the particle will actually follow a guiding center path that intersects the lunar orbit at point A. If the moon is also at point A and the detector is looking in the right direction, then the particle can be seen there if it is of the proper energy to be detected by the SIDE.

Clearly, if a particle leaves point P with less energy or a higher pitch angle, i.e. a "shorter" $\vec{V}_{p_{\parallel}}$, the same drift velocity vector added to its $\vec{V}_{p_{\parallel}}$ will yield a resultant velocity vector that defines a guiding center path that intersects the lunar orbit at a point that is closer to the shock than point A. Conversely, a particle leaving the shock with greater parallel energy, i.e. a "longer" $\vec{V}_{p_{\parallel}}$, will have a resultant velocity vector that will define a guiding center path that intersects the lunar orbit at a point further away from the shock than point A.

That is, whether or not a particle of a given energy is detected at the lunar orbit is dependent upon the orientation of the interplanetary $\vec{B}$ field, the magnitude and direction of the solar wind and the particle's initial energy and pitch angle upon leaving the shock.

From the above description of the energy selection mechanism that is operating in the post shock region of the lunar orbit, it becomes clear that for a particle leaving the shock with a given parallel energy $\mathcal{E}_{p_{\parallel}}$, and hence a given initial parallel velocity $\vec{V}_{p_{\parallel}}$, that there exists a point Q on the bow shock that defines an energy cutoff point in the lunar orbit. If the moon has advanced in its orbit beyond the point C in figure 3-2, then particles of energy $\mathcal{E}_{p_{\parallel}}$ leaving the bow shock can no longer be seen by the detector.

The cutoff point varies with energy and interplanetary field conditions, but one expects that in the post shock crossing region of the lunar orbit, that the lower energy particles will begin to disappear from the data as the moon advances toward instrument nightime. This effect is observed in the data and will be discussed again in the chapter concerning the data. (chapter 5)

A completely analogous mechanism is operating on the inbound side of the bow shock and the appropriate vector diagram for that region is also illustrated in figure 3-2. Due to the geometric asymmetry in the field configuration, the data from the inbound side of the shock will show a somewhat different effect. The higher energy particles will be seen further away from the shock than will the lower energy ones, but none will be seen as far away from the shock as on the outbound side for a given field configuration. This is in agreement with the "dusk-dawn" asymmetry observed by Asbridge et al. [1968].

The above discussion required that the solar ecliptic latitude of the field be approximately zero since the moon's orbit lies approximately, (+ or - 5°), in the ecliptic plane. This would suggest that if the interplanetary $\vec{B}$ field were not in the ecliptic plane or close to it, then particles leaving the bow shock might not be seen by the detector. Indeed, if the field is far away from the ecliptic plane, particles leaving the shock along these lines could likely miss the lunar orbit entirely. (see figure 3-3)

In the above discussion, the interplanetary field was taken to be approximately in the ecliptic plane. If the solar wind vector also lies approximately in the ecliptic plane, this requires that $\vec{E}=-\vec{V}_{SW}\times\vec{B}$ be perpendicular to the ecliptic plane and hence $\vec{V}_d$ will also lie in the ecliptic

Figure 3-3. Illustration in three planes of the dependence of the resultant guiding center trajectory on the interplanetary field latitude.

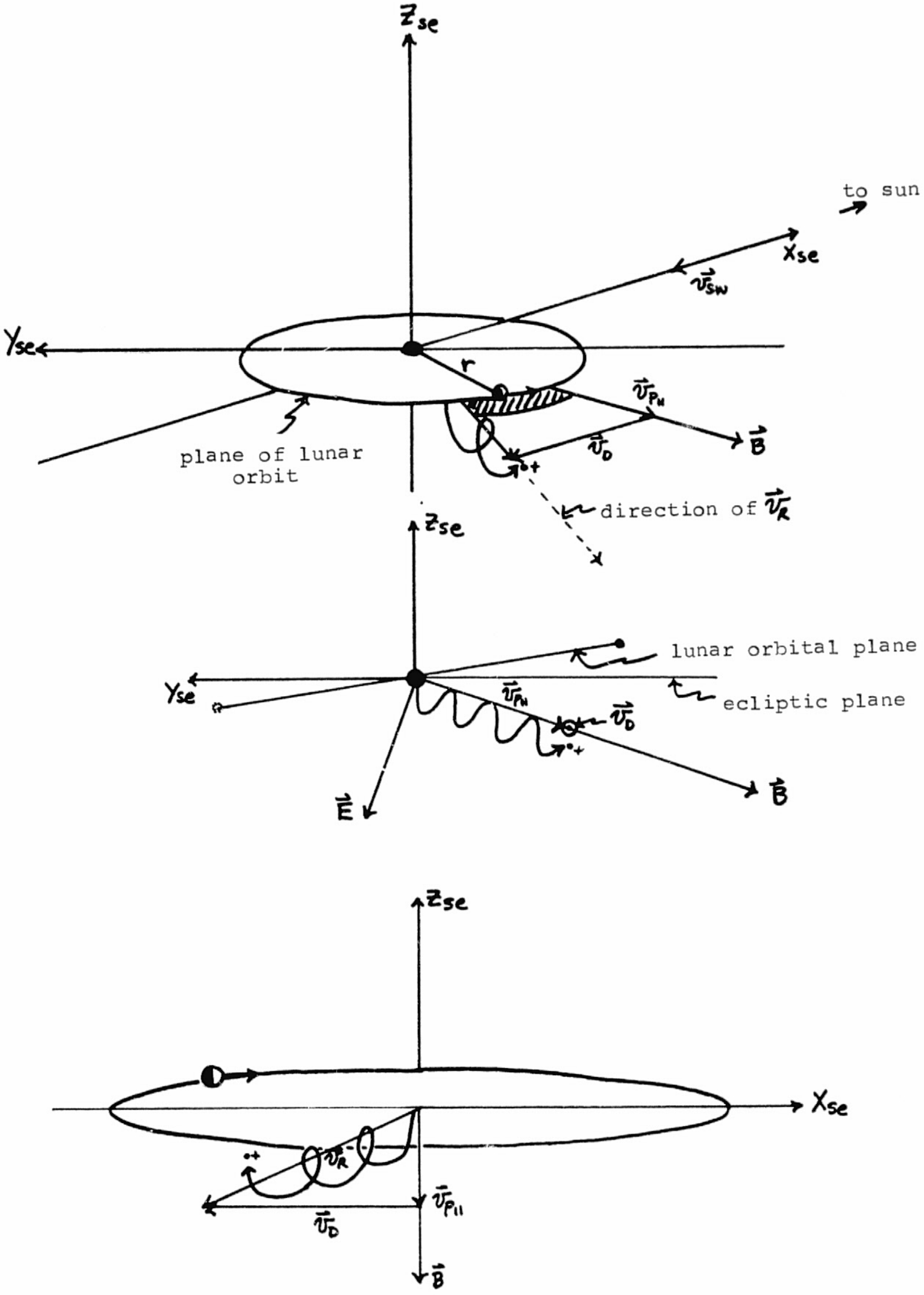
Z_{se}
to sun
X_{se}
$\vec{v}_{SW}$
Y_{se}
r
$\vec{v}_{P_\perp}$
$\vec{B}$
$\vec{v}_D$
plane of lunar orbit
+
direction of $\vec{v}_R$
Z_{se}
lunar orbital plane
Y_{se}
ecliptic plane
$\vec{v}_{P_\perp}$
$\vec{v}_D$
+
$\vec{E}$
$\vec{B}$
Z_{se}
X_{se}
+
$\vec{v}_R$
$\vec{v}_{P_{\parallel}}$
$\vec{v}_D$
$\vec{B}$

Figure 3-3

plane as will the resultant velocity vector $\vec{V}_r$. But if $\vec{B}$ is not in the ecliptic, the resultant velocity vector will be out of the ecliptic plane. As can be seen in figure 3-3, whether or not a particles's guiding center trajectory intersects the lunar orbit is fairly sensitive to the interplanetary field latitude. An analysis of the data shows this effect and will be discussed in chapter 5.

It should also be pointed out that there is an interesting dusk-dawn asymmetry in the direction of the interplanetary $\vec{E}$ field when the $\vec{B}$ field is at high positive or high negative latitudes. Figure 3-4 shows that for a $\vec{B}$ field latitude of +90° on the dawn side, that the interplanetary electric field points outwardly from the shock and similarly a $\vec{B}$ field latitude of -90° on the dusk side generates an $\vec{E}$ field that also points away from the shock. This gives rise to another mechanism, as discussed by Manka [1972], for getting particles into the detector that has a definite dusk-dawn asymmetry associated with it.

The foregoing description of the model has ignored any influence of the perpendicular energy of the particle and hence the size of its gyroradius. To gain understanding of this influence, the actual particle trajectories will now be discussed.

Figure 3-4. Diagram illustrating the dusk-dawn asymmetric interplanetary electric field $\vec{E}$ that occurs at high positive and negative values of the interplanetary B field latitude.

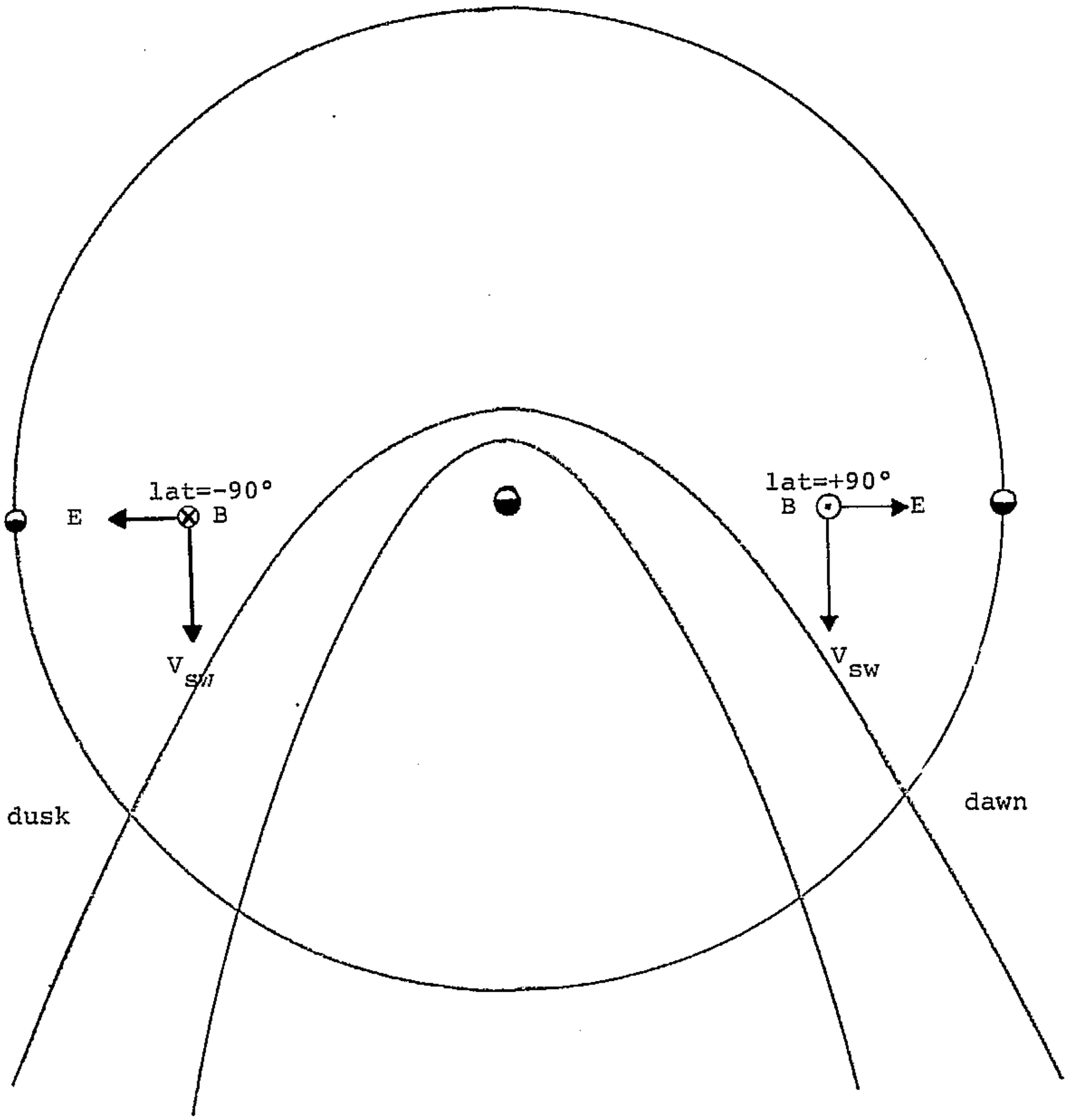

Figure 3-4

3.3 Actual particle trajectories

The gyroradius of a 3 keV proton in a 5γ field is about 1500 km which is comparable to the lunar radius ($\sim$1700 km). This implies that a strict interpretation of the above treatment, where the particle follows the guiding center path determined by $\vec{V}_r$, is not quite correct. The actual trajectories depend on the particle's initial velocity and pitch angle α and can be calculated from the parametric equations 3-2, 3-3, and 3-4. The pitch angle is the angle between the initial velocity vector and the direction of the field which implies that

$$V_{p_\parallel} = V_{zo} = V_o \cos\alpha \qquad \text{3-10}$$

where

$$V_o = \left(V_{xo}^2 + V_{yo}^2 + V_{zo}^2\right)^{1/2} = (2\mathcal{E}/m)^{1/2} \qquad \text{3-11}$$

and

$$V_{p_\perp} = V_o \sin\alpha = \left(V_{xo}^2 + V_{yo}^2\right)^{1/2} \qquad \text{3-12}$$

For typical conditions, V_{sw}=400 km/sec, B=5γ, several cases of proton motion are shown, to scale, in figures 3-5 through 3-9. It is evident from these figures that particles whose guiding center trajectories intersect the moon

Figure 3-5. Scaled illustration of cycloidal motion of typical bow shock protons. Top curve is the case of all parallel energy and the bottom curves are cases of 1 keV of perpendicular energy distributed in three different ways. V_x and V_y are the values of the particle's initial velocity in the x and y directions respectively in units of km/sec.

Figures 3-6 through 3-9. Additional cases of cycloidal motion for perpendicular energies higher than 1 keV. Note the interesting case in figure 3-6 where the x-component of the initial velocity is approximately equal to the drift velocity (283 km/sec). (See equation 3-6)

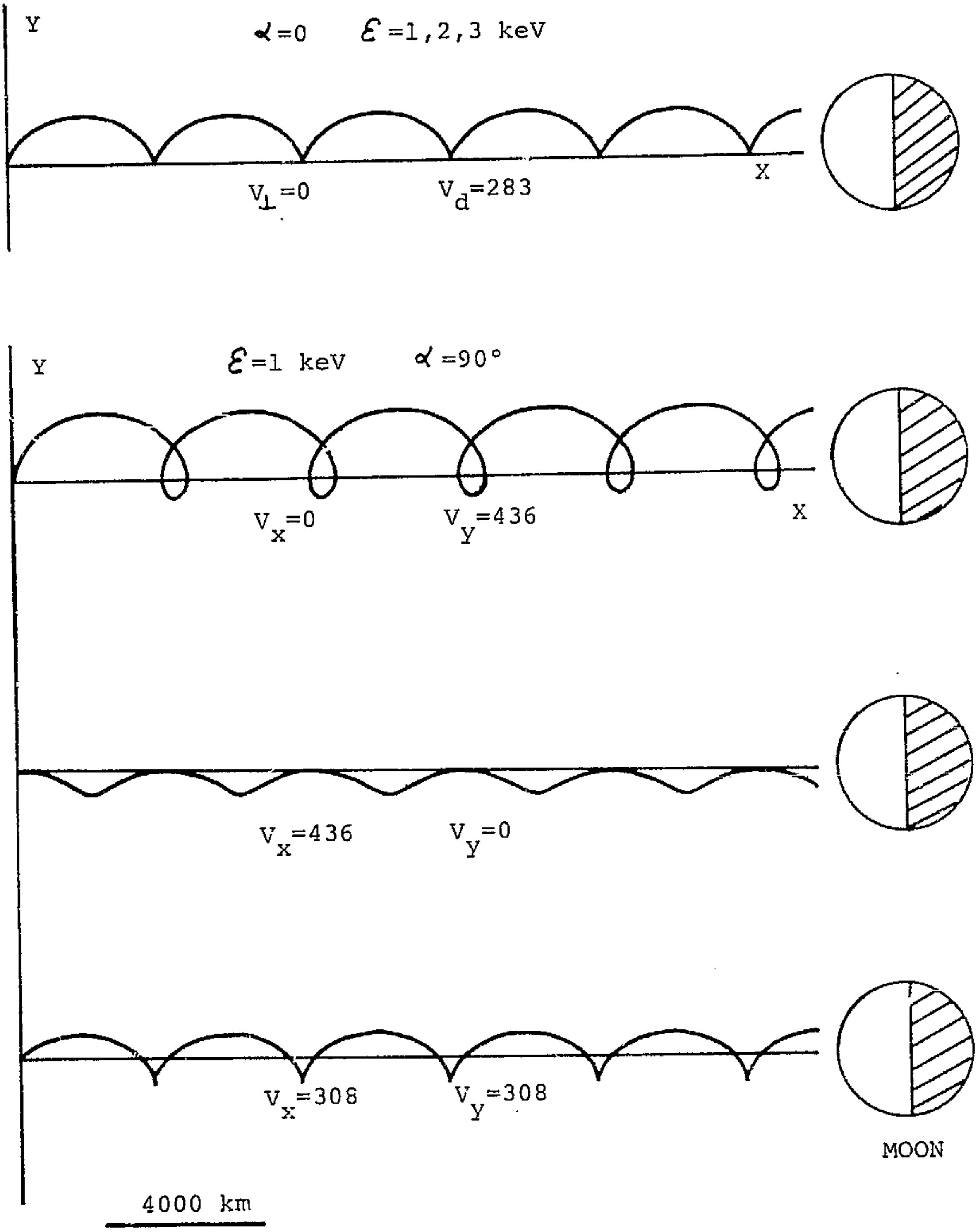
Y
$\alpha=0$ $\mathcal{E}=1,2,3$ keV
$V_\perp=0$
$V_d=283$
X
Y
$\mathcal{E}=1$ keV $\alpha=90°$
$V_x=0$
$V_y=436$
X
$V_x=436$
$V_y=0$
$V_x=308$
$V_y=308$
MOON
4000 km

Figure 3-5

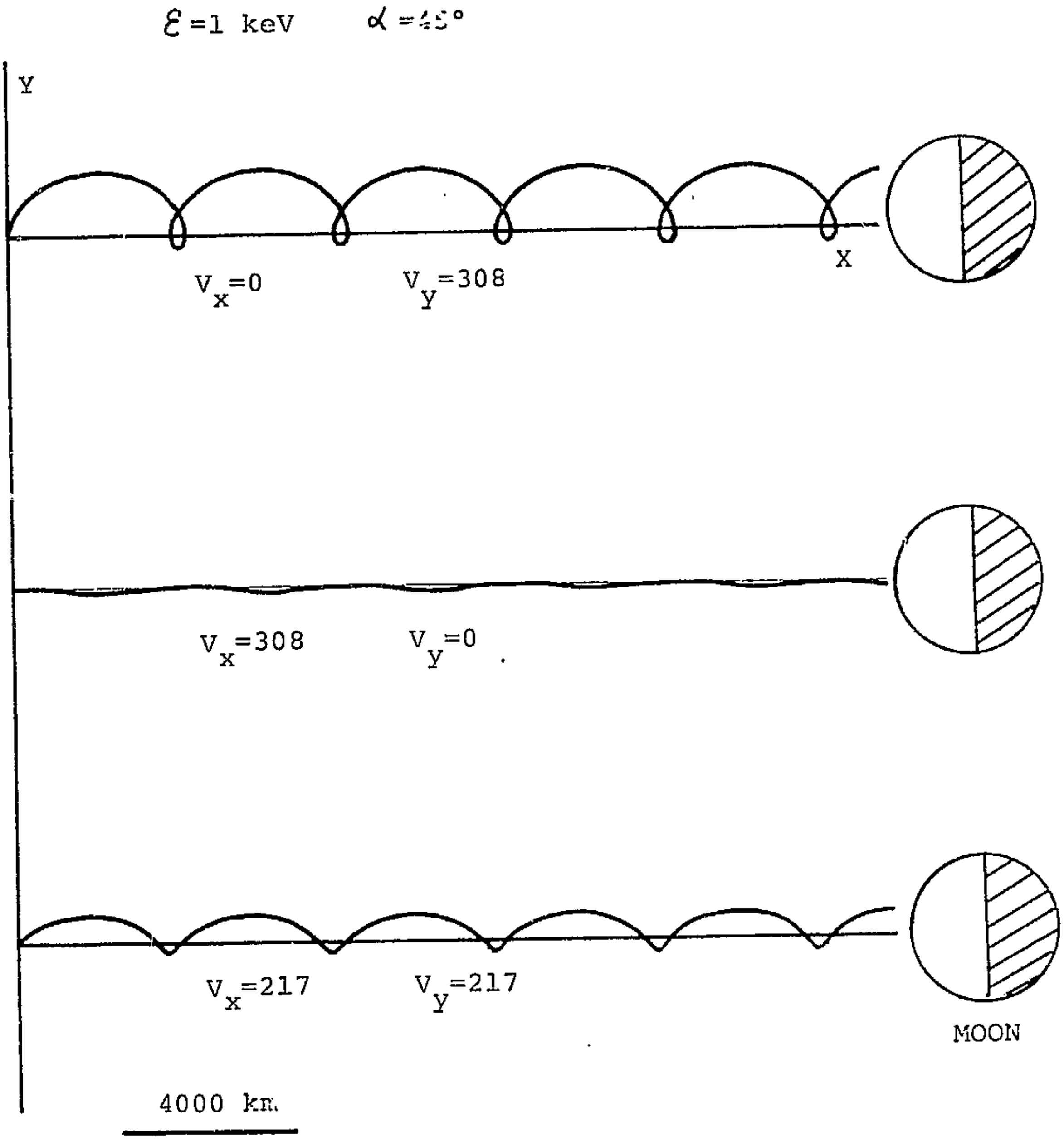

Figure 3-6

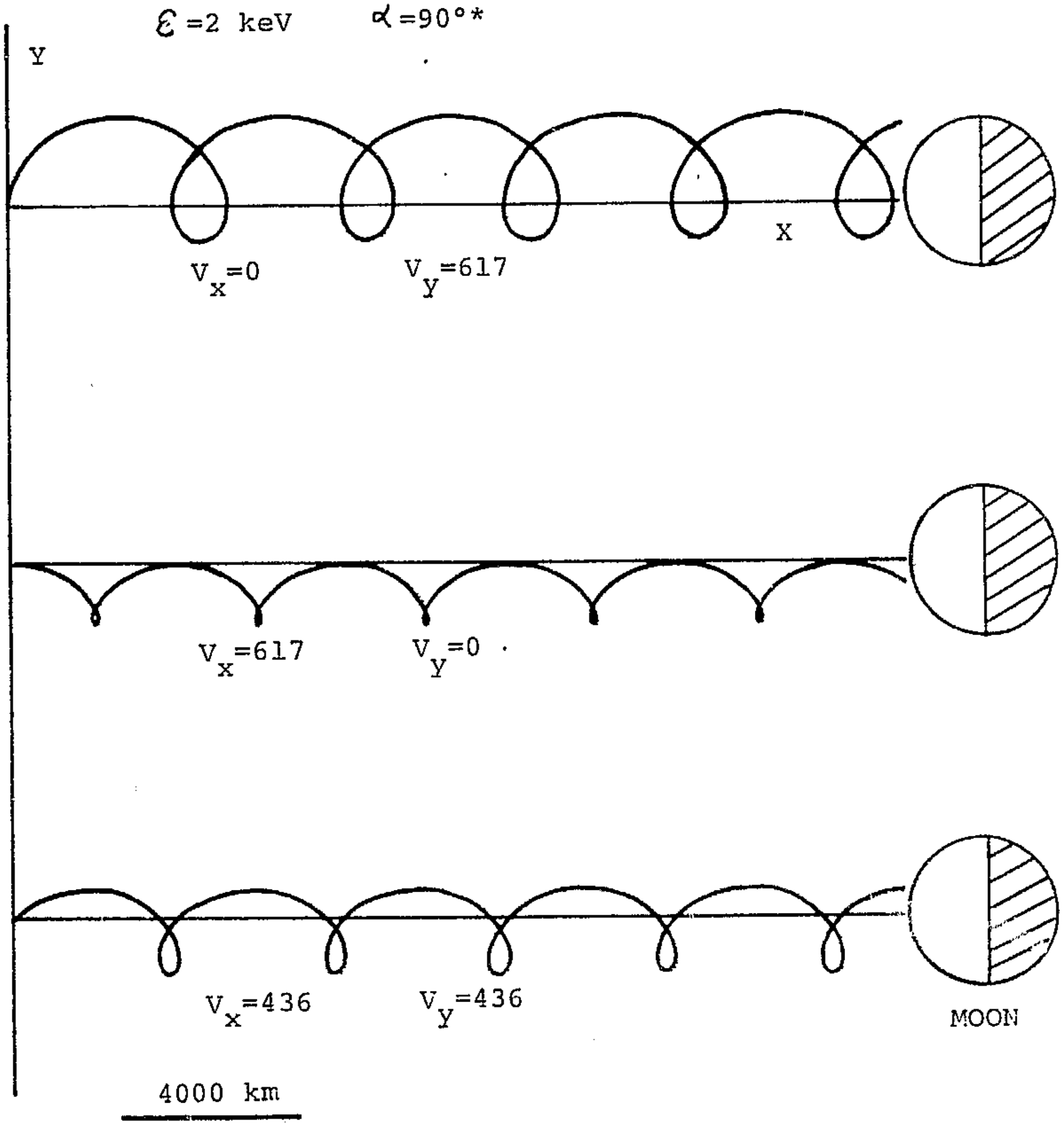

* $\alpha=45°$, $\mathcal{E}=2$ keV is the same as case for $\mathcal{E}=1$ keV $\alpha=90°$

Figure 3-7

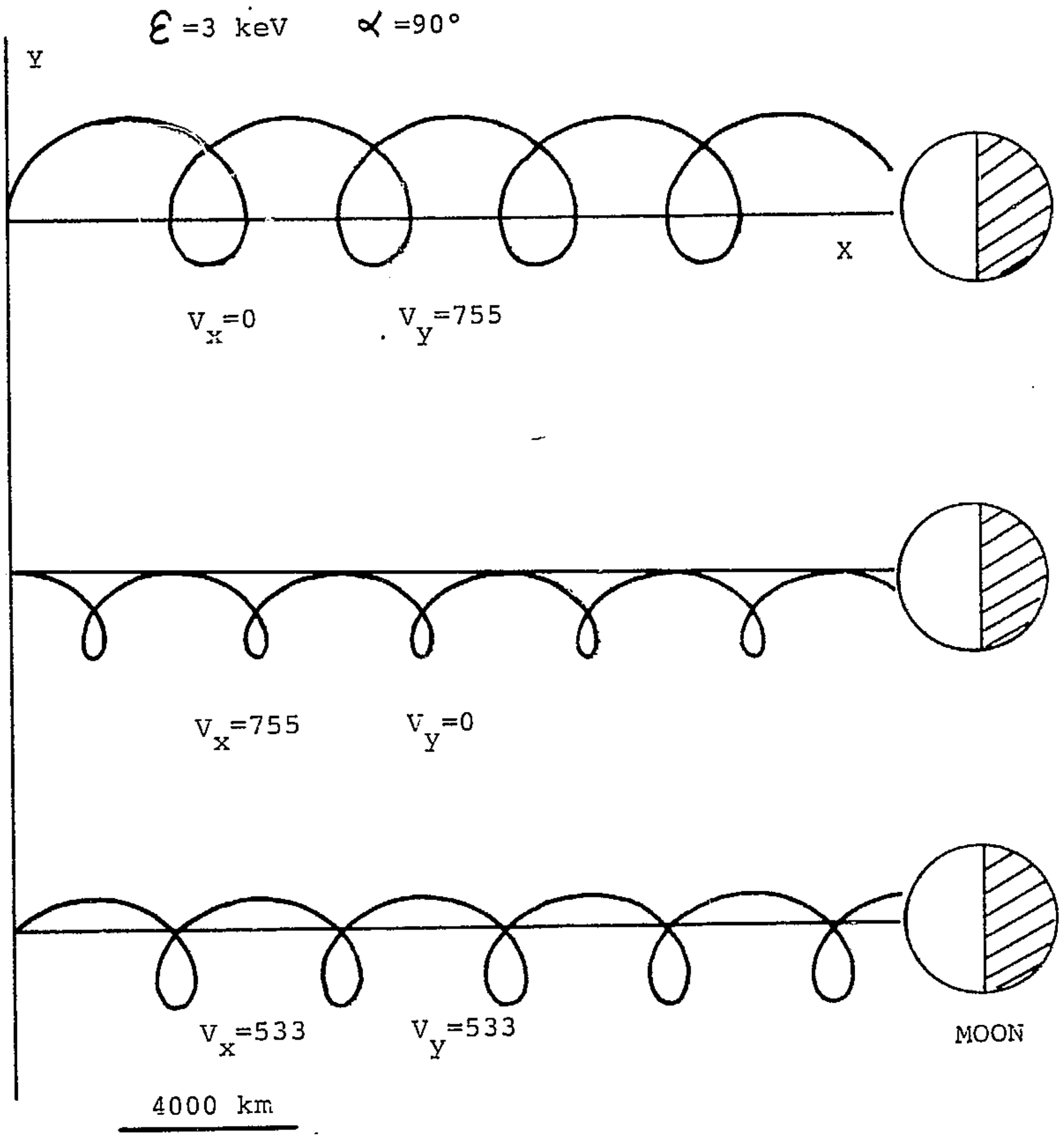

Figure 3-8

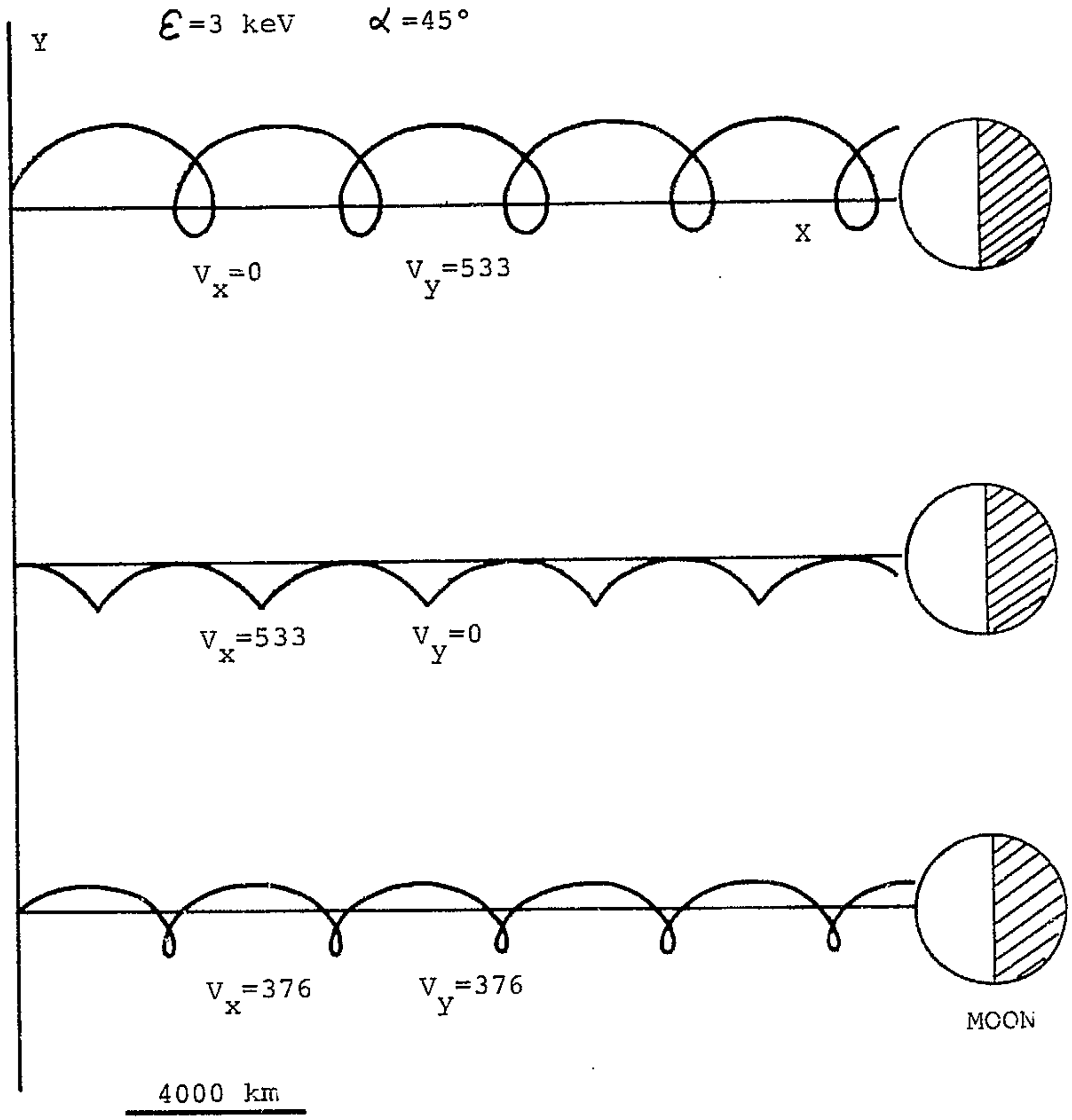

$\mathcal{E}$=3 keV
α =45°
Y
X
V_x=0
V_y=533
V_x=533
V_y=0
V_x=376
V_y=376
MOON
4000 km

Figure 3-9

can enter the detector from a wide range of angles. The implications of this on the interpretation of the data are discussed in chapter 5.

3.4 Asbridge Model

The model proposed by Asbridge et al. [1968] is very similar to the present treatment and the basic idea behind their model is illustrated in figure 1-6. The resultant velocity vector of the particle is determined by,

$$\vec{V}_f = \vec{V}_i + \vec{V}_{sw} \qquad 3\text{-}13$$

where, $\vec{V}_i$ is the particle's initial velocity parallel to the field. This differs from the expression for the resultant velocity vector given in equation 3-7 by the factor,

$$-(\vec{V}_{sw} \cdot \hat{B}) \hat{B} \qquad 3\text{-}14$$

which is just the component of the solar wind velocity parallel to the field. When $\vec{V}_{sw}$ is perpendicular to $\vec{B}$, the two expressions are equivalent.

The basic difficulty with eqation 3-13 is that it appears to give the resultant guiding center velocity vector in the frame of the bow shock for a particle that is injected into

C, 2

the solar wind along the $\vec{B}$ field in the shock frame. There is no question that if a particle left the bow shock in the direction defined by $\vec{V}_f$ that it would continue along this path undeviated by any electric fields since

$$\vec{E}_{\perp}' = (\vec{E}_{\perp} + \vec{V}_f \times \vec{B}) = 0 \qquad 3\text{-}15$$

nonrelativistically. However, if the particle actually had a velocity $\vec{V}_i$ in the shock frame as indicated in figure 1-6, it would not go in the direction defined by $\vec{V}_f$ as indicated by the Asbridge model.

This point can be clarified by considering the transformation between a frame of reference that is moving with the solar wind and the rest frame of the bow shock. Since $V_{sw} \ll c$, the transformation is Galilean,

$$\begin{aligned} x &= x' + V_{sw}t \\ y &= y' \qquad\qquad 3\text{-}16 \\ z &= z' \end{aligned}$$

where the moving frame is being translated along the x-axis at the solar wind velocity. This implies that,

$$\vec{V} = \vec{V}' + \vec{V}_{sw} \qquad 3\text{-}17$$

If $\vec{V}'$ is directed along $\vec{B}$ in the moving frame, then the velocity seen in the rest frame is $\vec{V}$. Equation 3-13 is actually just a transformation from a frame moving with the solar wind to the rest frame of the shock, i.e.,

$$\vec{V}_i = \vec{V}' \qquad 3\text{-}18$$

and

$$\vec{V}_f = \vec{V} \qquad 3\text{-}19$$

It is not realistic to assume that one knows the inital velocity of the particle in the moving frame and therefore equation 3-7, derived in this chapter, is the appropriate expression to determine the resultant guiding center trajectory of a particle in the rest frame of the shock. It is interesting to note that when $\vec{V}_{sw}$ is not perpendicular to $\vec{B}$, equation 3-9 yields a resultant guiding center trajectory that allows particles to travel to points at the lunar orbit that are more sunward than those predicted by equation 3-13.

3.5 Conclusions

The discussions in this chapter lead to the following conclusions.

a.) There are particlular interplanetary field longitudes that are favorable to the observation of particles of a given energy at a given point in the lunar orbit and this fact gives rise to energy cut-offs in the post shock region of the lunar orbit and energy cut-ons in the pre shock region.

b.) There are particular interplanetary field latitudes that are favorable to the observation of particles in the post and pre shock regions of the lunar orbit, viz. those in the neighborhood of zero degrees.

c.) There is an inherent dusk-dawn asymmetry in the model that should be observable in the data.

d.) There is a dusk-dawn asymmetric interplanetary electric field mechanism for getting particles into the detector that is dependent on high positive and high negative values of the interplanetary $\vec{B}$ field latitude.

e.) Although the Asbridge model of guiding center trajectories gives the correct qualitative picture of particles leaving the bow shock and the correct quantitative picture if interpreted correctly, the $\vec{E} \times \vec{B}$ model proposed in this thesis is more appropriate for the reasons discussed in this chapter.

Chapter 4

In light of the foregoing discussion, a computer model for the $\vec{E} \times \vec{B}$ mechanism has been generated. The description of this computer model and its connection to the physical model of the previous chapter will be given below. In order to generate a qualitative picture of what the detector should see as a function of time, it is necessary to calculate the components of a vector $\hat{D}(t)$ that represents the look direction of the detector as a function of time and use this vector in conjunction with the vectors $\vec{V}_r(\mathcal{E}, \alpha)$, the resultant guiding center trajectory vector, and $\vec{r}$, the position vector of the moon to determine whether or not a particle is seen. By defining a source with certain characteristics and "acceptance criteria" for the detector, a spectrum of counts vs. energy can be obtained and compared to the real data. What follows is a description of the computer model.

4.1 Orbit

In order to determine whether or not a particle leaving the bow shock will hit the moon, it is necessary to determine the position vector of the moon, $\vec{r}$. Figure 4-1 shows the orientation of the lunar orbit with respect to an inertial system whose x-y plane is in the plane of the ecliptic. The orbital inclination, θ, is exaggerated in the figure for clarity; it has a value of about 5°. The x' axis intersects the lunar orbit at perigee (denoted by π) in the figure.

Figure 4-1. Illustration of the relation of the lunar orbit to the solar ecliptic plane showing time dependent angles relevant to the calculation of the position of the moon. π denotes perigee. θ is exaggerated in the figure for clarity. In reality $\theta \sim 5°$.

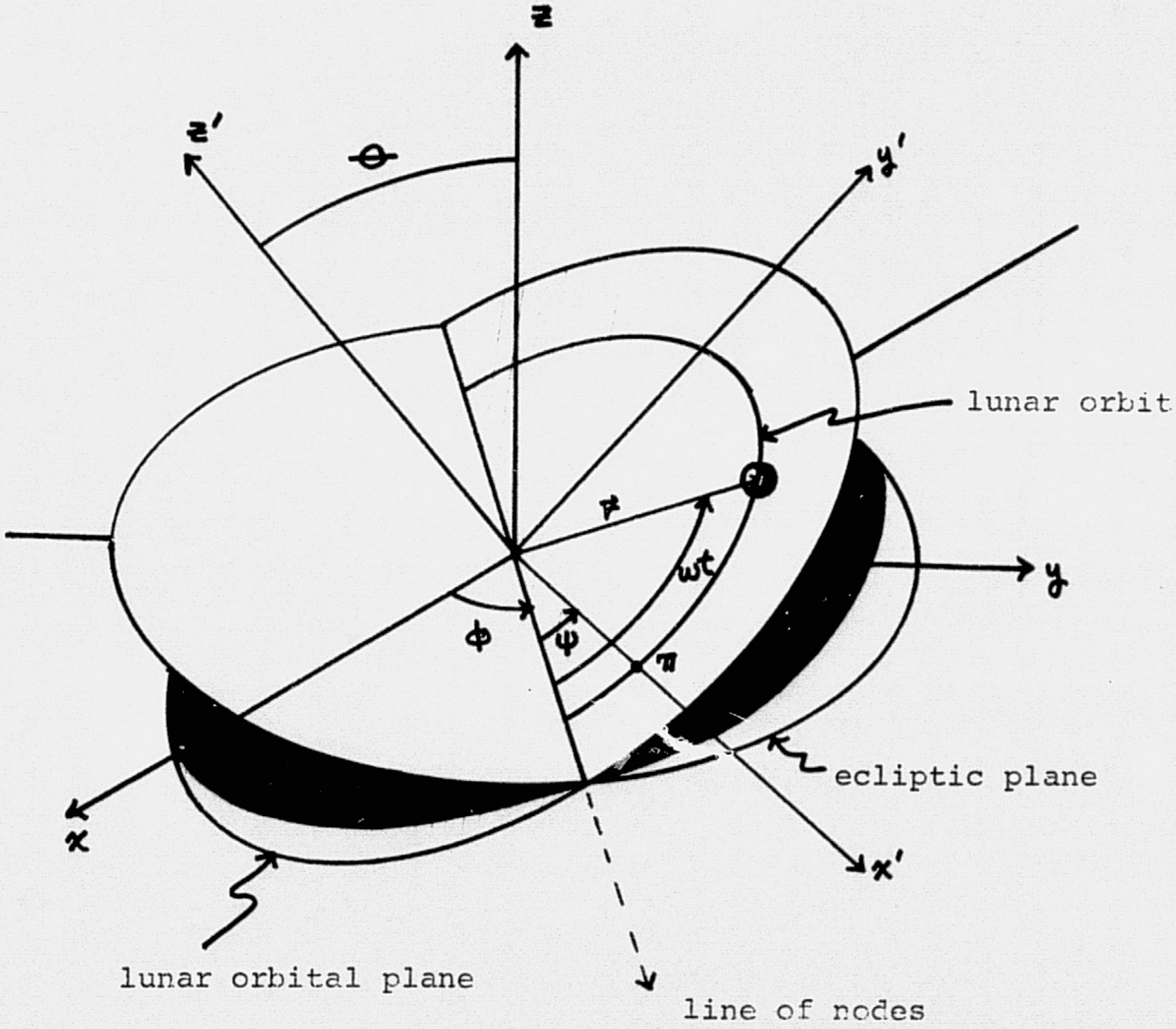
z
z'
θ
y'
lunar orbit
r
ωt
y
φ
ψ
π
ecliptic plane
x
x'
lunar orbital plane
line of nodes

Figure 4-1

and precesses with a period of approximately 8.5 years in a counterclockwise direction when viewed from a point on the z'-axis above the x'-y' plane. The line that divides the time between when the moon is above the ecliptic plane and the time when it is below the ecliptic plane is known as the line of nodes and it precesses in a clockwise direction when looking in the negative z-direction from a point above the ecliptic plane. The line of nodes precesses with a period of approximately 18.6 years.

The moon moves in a slightly elliptical ($\epsilon \sim .05$) orbit that lies in the x'-y' plane with perigee occuring on the x' axis. The distance from the earth to the moon as a function of time is given by

$$r = \frac{a\ (1-\epsilon^2)}{1+\epsilon\cos(\omega t-\psi)} \qquad 4\text{-}1$$

where, a = semi-major axis, ϵ = eccentricity, ω = angular velocity of the moon based on the sidereal period, ψ = argument of perigee, and t begins at ascending node.

The angles, relevant to the Eulerian transformation, as functions of time are determined by,

$$\phi(t) = \phi_o - \Omega_{1on} t \quad \text{(-) implies CW precession}$$

$$\phi_o = \text{argument of line of nodes at } t=0 \qquad 4\text{-}2$$

$$\Omega_{1on} = 2\pi/\tau_{1on} \qquad \tau_{1on} = 18.6 \text{ yrs.}$$

$$\psi(t) = \psi_o + \Omega_{1oa} t \quad (+) \text{ implies CCW precession}$$

$$\psi_o = \text{argument of perigee at } t=0 \qquad 4\text{-}3$$

$$\Omega_{1oa} = 2\pi/\tau_{1oa} \qquad \tau_{1oa} = 8.6 \text{ yrs.}$$

$$\theta(t) = \text{const.} \qquad \theta_o \cong 5^o$$

The transformation from a coordinate system, S'', that is fixed in the moon, to the solar ecliptic system, S_{se} is accomplished by first transforming from S'' to S' and then from S' to S and finally from S to S_{se}. That is if $\underline{A}$ represents the matrix transformation from S'' to S', $\underline{B}$ represents the transformation from S' to S and $\underline{S}$ represents the transformation from S to S_{se} then,

$$\vec{r}\,' = \underline{A}\,\vec{r}\,''$$

$$\vec{r} = \underline{B}\,\vec{r}\,' \qquad 4\text{-}4$$

$$\vec{r}_{se} = \underline{S}\,\vec{r}$$

which implies that,

$$\vec{r}_{se} = \underline{S}\,\underline{B}\,\underline{A}\,\vec{r}\,''$$

The coordinate system S'' is simply rotating with respect to S' so that the angle between the x''-axis and the x'-axis is,

$$\Theta = \omega t - \psi(t) \qquad 4\text{-}5$$

and since z'' = z',

$$\underline{A} = \begin{pmatrix} \cos\Theta & -\sin\Theta & 0 \\ \sin\Theta & \cos\Theta & 0 \\ 0 & 0 & 1 \end{pmatrix} \qquad 4\text{-}6$$

The transformation from S' to S is given by equation 4-7, shown on the next page.

The inertial system S is stationary with respect to the fixed stars but the x-y axes of the SE system rotate slowly with respect to the inertial system due to motion of the earth in its orbit about the sun. That is, the x_{se}-axis rotates with respect to the x-axis about a degree per day in the counterclockwise direction as viewed from above the ecliptic plane. Therefore, the transformation from the inertial system to the solar ecliptic system is given by the matrix,

$$\underline{S} = \begin{pmatrix} \cos\xi & -\sin\xi & 0 \\ \sin\xi & \cos\xi & 0 \\ 0 & 0 & 1 \end{pmatrix}$$

where,

$$\xi = \xi_o + (2\pi t)/\tau_e$$

τ_e = sidereal period of the earth

Therefore the components of the vector $\vec{r}$ in the SE system

$$\underline{B}= \begin{pmatrix} \cos\psi\cos\phi-\cos\theta\sin\phi\sin\psi & -\sin\psi\cos\phi-\cos\theta\sin\phi\cos\psi & \sin\theta\sin\phi \\ \cos\psi\sin\phi+\cos\theta\cos\phi\sin\psi & -\sin\psi\sin\phi+\cos\theta\cos\phi\cos\psi & -\sin\theta\cos\phi \\ \sin\theta\sin\psi & \sin\theta\cos\psi & \cos\theta \end{pmatrix} \tag{4-7}$$

are,

$$r_{se_x} = (\,S\,B\,A\,)_{xx}\, r_x'' \qquad r_{se_y} = (\,S\,B\,A\,)_{yx}\, r_x'' \qquad r_{se_z} = (\,S\,B\,A\,)_{zx}\, r_x'' \tag{4-8}$$

where,

$$r_x'' = r$$

and the matrix elements of SBA are shown on the next page.

4.2 Detector Look Direction

If one know the orientation of the detector look vector, $\vec{D}'''$ in a coordinate system, S''', that is fixed at the ALSEP site, then the components of this vector can be expressed in a S.E. system, S_{se}, by making an Eulerian transformation from S''' to S_{se}.

The moon's rotational axis makes an angle with the ecliptic plane of about 1.5 degrees and the rotational period is equal to the sidereal period. Figure 4-2 shows the relationship between the coordinate system fixed at the ALSEP site and the solar ecliptic system.

The Apollo 12 and 14 instruments were deployed very near the lunar equator and for the purposes of this treatment we

$$
\begin{aligned}
(SBA)_{xx} = {} & \cos\xi \left[\cos\Theta\,(\cos\psi\cos\phi - \cos\theta\sin\phi\sin\psi) - \sin\Theta\,(\sin\psi\cos\phi + \cos\theta\sin\phi\cos\psi)\right] \\
& -\sin\xi \left[\cos\Theta\,(\cos\psi\sin\phi + \cos\theta\cos\phi\sin\psi) - \sin\Theta\,(\sin\psi\sin\phi - \cos\theta\cos\phi\cos\psi)\right]
\end{aligned}
$$

$$
\begin{aligned}
(SBA)_{yx} = {} & \sin\xi \left[\cos\Theta\,(\cos\psi\cos\phi - \cos\theta\sin\phi\sin\psi) - \sin\Theta\,(\sin\psi\cos\phi + \cos\theta\sin\phi\cos\psi)\right] \\
& +\cos\xi \left[\cos\Theta\,(\cos\psi\sin\phi + \cos\theta\cos\phi\sin\psi) - \sin\Theta\,(\sin\psi\sin\phi - \cos\theta\cos\phi\cos\psi)\right]
\end{aligned}
$$

$$
(SBA)_{zx} = (\cos\Theta\sin\psi + \sin\Theta\cos\psi)\sin\theta
$$

Equations 4-9

Figure 4-2. Relationship of the ALSEP coordinate system S''', or system 1, to the SE coordinate system. For deployment at the sub-earth point, $\hat{x}'''$ points to earth and remains approximately that way due to the equality of the lunar sidereal period and the rotational period. Small changes are due to physical librations.

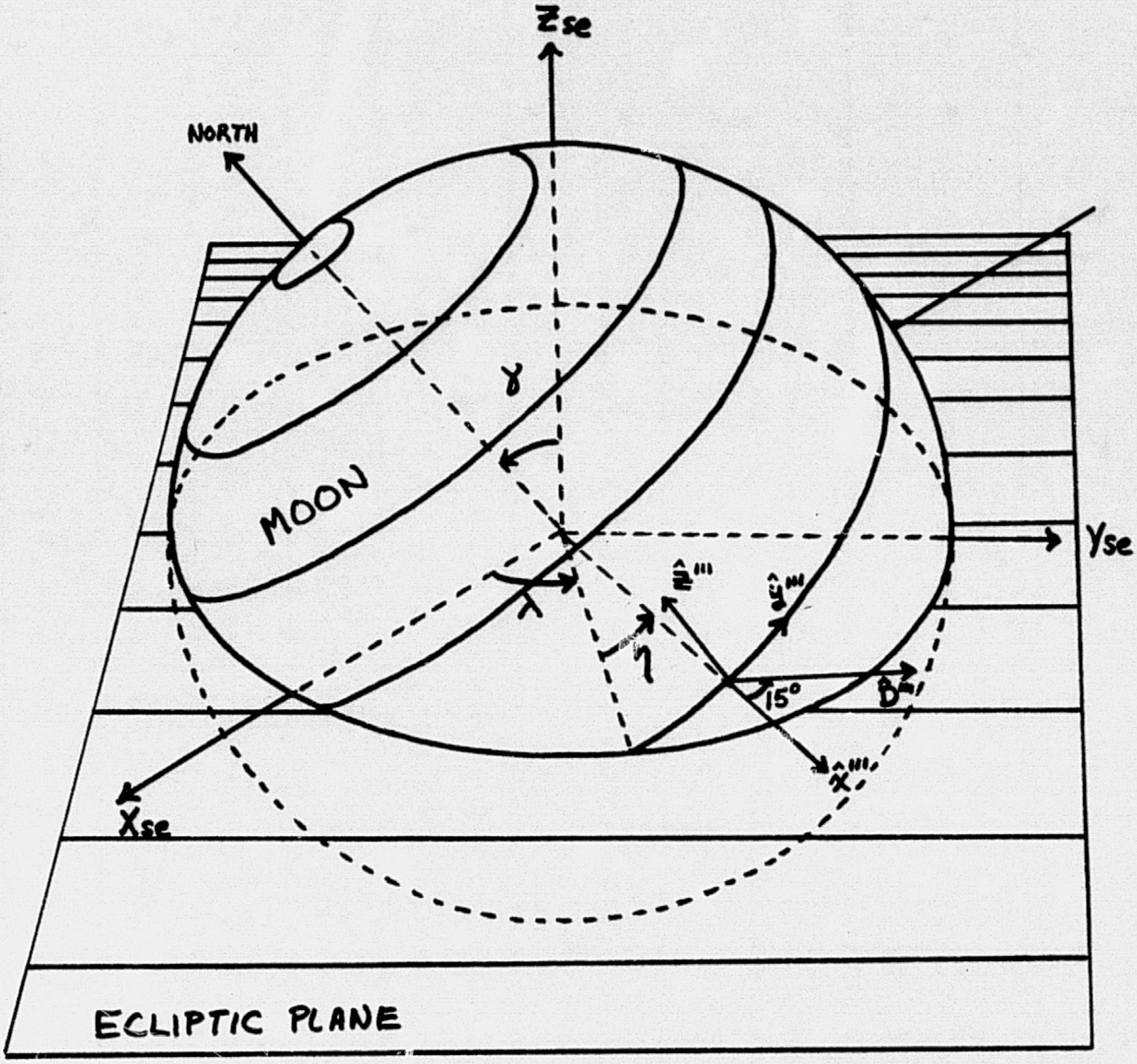

$$\gamma \approx 1^\circ 32' \approx \text{const.}$$

$$\eta(t) = \eta_0 + \frac{2\pi}{\tau_{sid}} t$$

$$\lambda(t) = \lambda_0 + \frac{2\pi}{\tau_e} t$$

τ_{sid} = sidereal period of moon

τ_e = sidereal period of earth

Figure 4-2

will assume that they were deployed exactly on the equator. Then at the ALSEP site the unit vector $\hat{x}'''$ is in the direction of the local vertical, $\hat{z}'''$ points north and in the case of equatorial deployment, $\hat{z}'''$ is parallel to the rotational axis of the moon. $\hat{y}'''$ completes the right-handed system and is directed eastward. S''' = system 1.

The instrument, (assume Apollo 14), was deployed at the ALSEP site so that the body axes were coincident with $\hat{x}'''$, $\hat{y}'''$ and $\hat{z}'''$. The vector that represents the look direction of the detector in the S''' system is then,

$$\vec{D}''' = \begin{pmatrix} D \cos 15° \\ D \sin 15° \\ 0 \end{pmatrix} \qquad 4\text{-}10$$

The Eulerian transformation from S''' to S_{se} is given on the following page. Using this transformation $\vec{D}$ in the SE system is,

$$\vec{D} = \underline{T}\,\vec{D}''' \qquad 4\text{-}12$$

that is,

$$\begin{aligned} D_x &= (\,T\,)_{xx}\,D_x''' + (\,T\,)_{xy}\,D_y''' \\ D_y &= (\,T\,)_{yx}\,D_x''' + (\,T\,)_{yy}\,D_y''' \qquad 4\text{-}13 \\ D_z &= (\,T\,)_{zx}\,D_x''' + (\,T\,)_{zy}\,D_y''' \end{aligned}$$

$$T_{xx} = \cos\xi\,(\cos\eta\,\cos\lambda - \cos\gamma\,\sin\lambda\,\sin\eta) - \sin\xi\,(\cos\eta\,\sin\lambda + \cos\gamma\,\cos\lambda\,\sin\eta)$$

$$T_{xy} = \sin\xi\,(\cos\eta\,\cos\lambda - \cos\gamma\,\sin\lambda\,\sin\eta) + \cos\xi\,(\cos\eta\,\sin\lambda + \cos\gamma\,\cos\lambda\,\sin\eta)$$

$$T_{xz} = \sin\gamma\,\sin\eta$$

$$T_{yx} = -\cos\xi\,(\sin\eta\,\cos\lambda + \cos\gamma\,\sin\lambda\,\cos\eta) - \sin\xi\,(\cos\eta\,\cos\lambda\,\cos\gamma - \sin\lambda\,\sin\eta)$$

$$T_{yy} = -\sin\xi\,(\sin\eta\,\cos\lambda + \cos\gamma\,\sin\lambda\,\cos\eta) + \cos\xi\,(\cos\eta\,\cos\lambda\,\cos\gamma - \sin\lambda\,\sin\eta)$$

$$T_{yz} = \sin\gamma\,\cos\eta$$

$$T_{zx} = \cos\xi\,\sin\gamma\,\sin\lambda + \sin\xi\,\sin\gamma\,\cos\lambda$$

$$T_{zy} = \sin\xi\,\sin\gamma\,\sin\lambda - \sin\gamma\,\cos\lambda\,\cos\xi$$

$$T_{zz} = \cos\gamma$$

Equations 4-11

At this point, it is possible to calculate the resultant velocity of particles leaving the bow shock, $\vec{V}_r$, the position vector of the room $\vec{r}$, and the detector look direction $\hat{D}$, all in a solar ecliptic coordinate system.

4.3 Shape of the shock surface:

The source of the particles in this computer model is an idealized mathematical representation of the magnetospheric cavity that emits particles with a flat energy spectrum, isotropically at each point on its surface. The mathematical shape is a paraboloid of revolution that is fitted to the true shape of the bow shock surface. This fitting procedure will be discussed below. The model retains all of the qualitative features of the real bow shock and at least two of the quantitative features, the distance of the nose to the center of the earth and the distance from the center of the earth to the intersection of the lunar orbit with the shock. The paraboloid is shown in figure 4-3 and the equation in solar ecliptic coordinates is,

$$x = \frac{-d}{D^2} (y^2 + z^2) + d \qquad 4\text{-}14$$

where d is the distance from the nose of the shock to the center of the earth and D is the distance from the center of the

Figure 4-3. Idealized bow shock surface represented by the equation $X^2=-d/D^2(Y^2+Z^2)+d$ in a SE coordinate system.

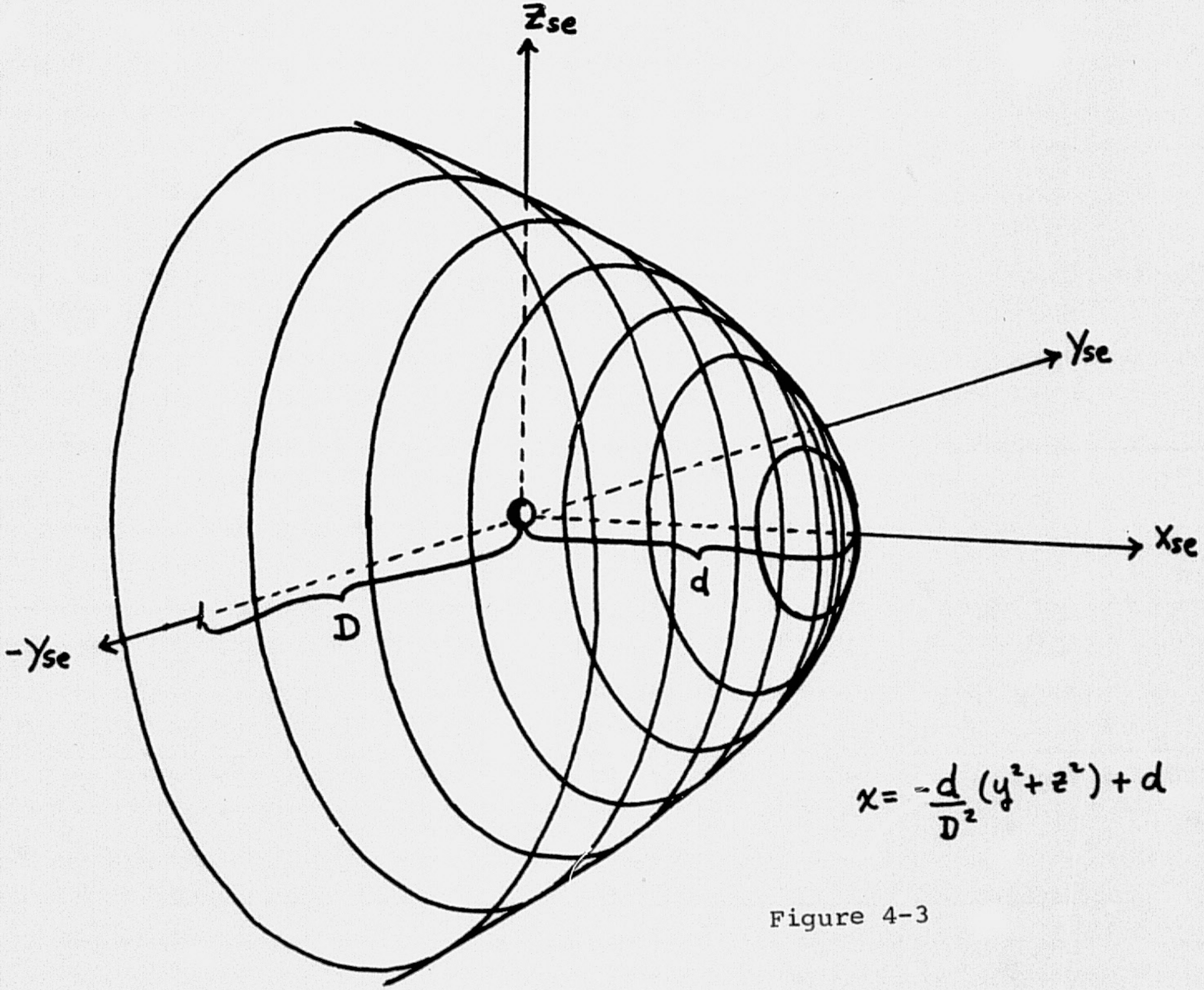

$$x = -\frac{d}{D^2}(y^2+z^2)+d$$

Figure 4-3

earth to the shock, measured along the y-axis. The shock stand-off distance d, can be calculated by equating the solar wind kinetic pressure to the magnetic pressure provided by the earth's dipole field so that

$$d \sim \left[B_o^2 \,/\, 4 \,\pi\, m \, n \, V^2 \right]^{1/6} \qquad 4\text{-}15$$

and the parameter D, can be determined from knowledge of the positions of actual bow shock crossings. cf. fig. 4-4a. That is by knowing the time of the bow shock crossing, the S.E. longitude can be obtained from the ephemeris data. The time of crossing can be determined accurately from the SIDE data. An example of this is shown in figure 4-4b. Solving equation 4-14 for D and neglecting any z dependence,

$$\begin{aligned} D &= \left(\frac{-d\, y^2}{x-d} \right)^{1/2} \qquad 4\text{-}16 \\ &= \left[\frac{-d\, r^2\, \sin^2}{r \cos \;-\; d} \right]^{1/2} \end{aligned}$$

D was calculated in this manner, but a constant value for d, ($\sim$12 R_e) was chosen over using the expression 4-15.

Figure 4-4a. Diagram illustrating the technique for fitting the idealized shock surface to the observed one. Knowing the distance d and measuring X_{bs} and Y_{bs} allows determination of D from equation 4-14.

Figure 4-4b. Illustration of how the postion of the bow shock is accurately determined for use in calculating D as discussed above.

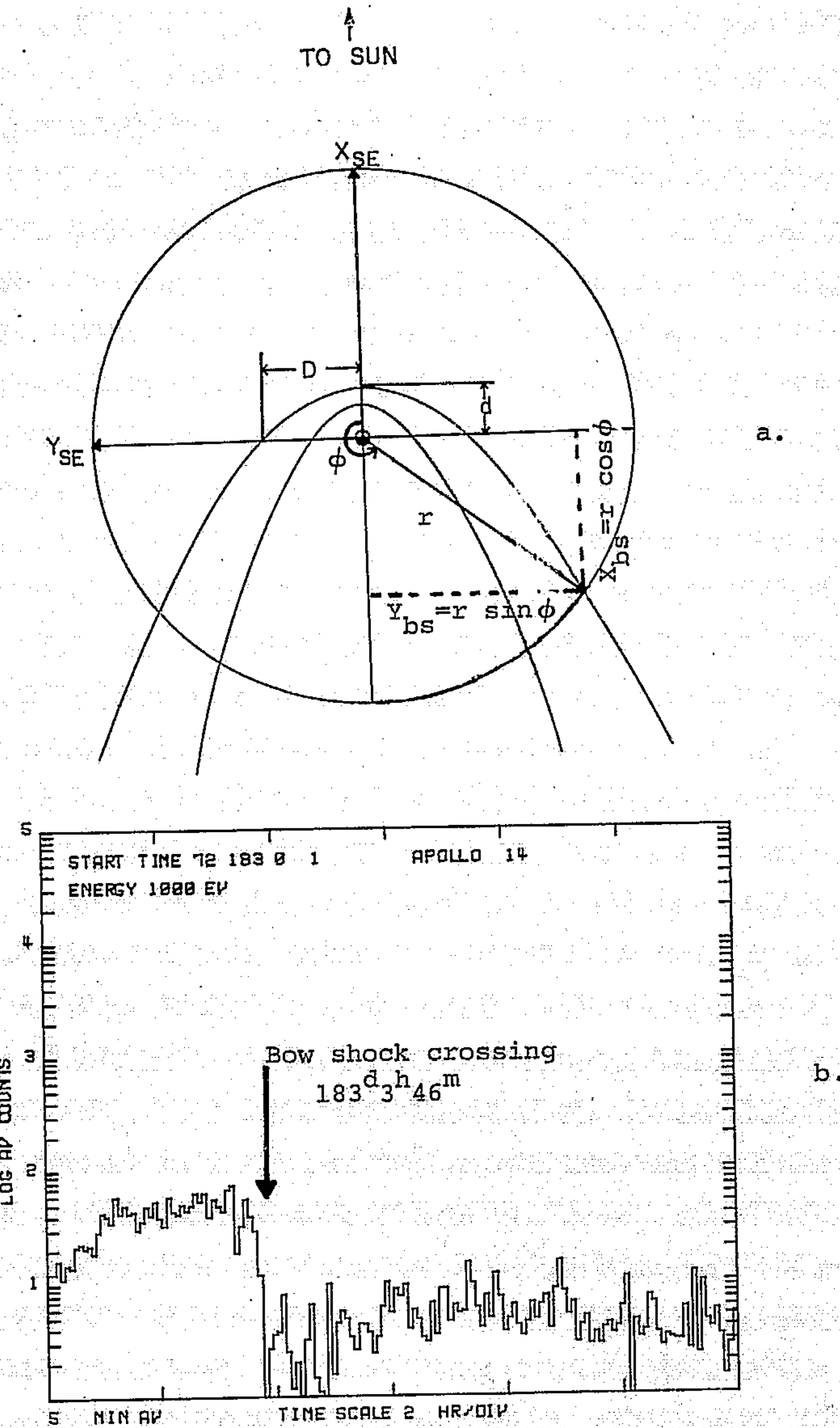
TO SUN
X_SE
Y_SE
D
d
φ
r
X_bs =r cos φ
Y_bs=r sin φ
a.
START TIME 72 183 0 1
APOLLO 14
ENERGY 1000 EV
Bow shock crossing
183^d 3^h 46^m
LOG AV COUNTS
5
4
3
2
1
5 MIN AV
TIME SCALE 2 HR/DIV
b.

Figure 4-4

4.4 Particle emission

Each point of the surface of the shock is taken to be an isotropic radiator of particles with a flat energy spectrum. That is, the same number of particles are emitted for each energy and the spectrum looks the same in all directions from each point of the surface. The total number of particles emitted at a given pitch angle α is proportional to the area on a unit sphere between $-\frac{\Delta\alpha}{2}$ and $+\frac{\Delta\alpha}{2}$. See figure 4-5a.

The number of particles available for detection is therefore weighted toward higher pitch angles by a factor of $\sin\alpha$. If n is the number of particles per square centimeter passing through a unit sphere centered at the point, then the number, dN, emitted at a given pitch angle α is,

$$dN = n\,dA$$

$$dN = 2\pi\, n \sin\alpha \, d\alpha$$

$$dN = \text{const.} \sin\alpha$$

for a constant interval $d\alpha$.

The total number N, emitted over the hemisphere, centered at each point, is,

$$N = \int dN = 2\pi n$$

Figure 4-5a. Shows that for an isotropic radiator the number of particles emitted at pitch angle α depends on α .

Figure 4-5b. Illustrates that all of the source points in the field of view of the detector are tested constituting a numerical integration over the source to determine the counts observed at the detector.

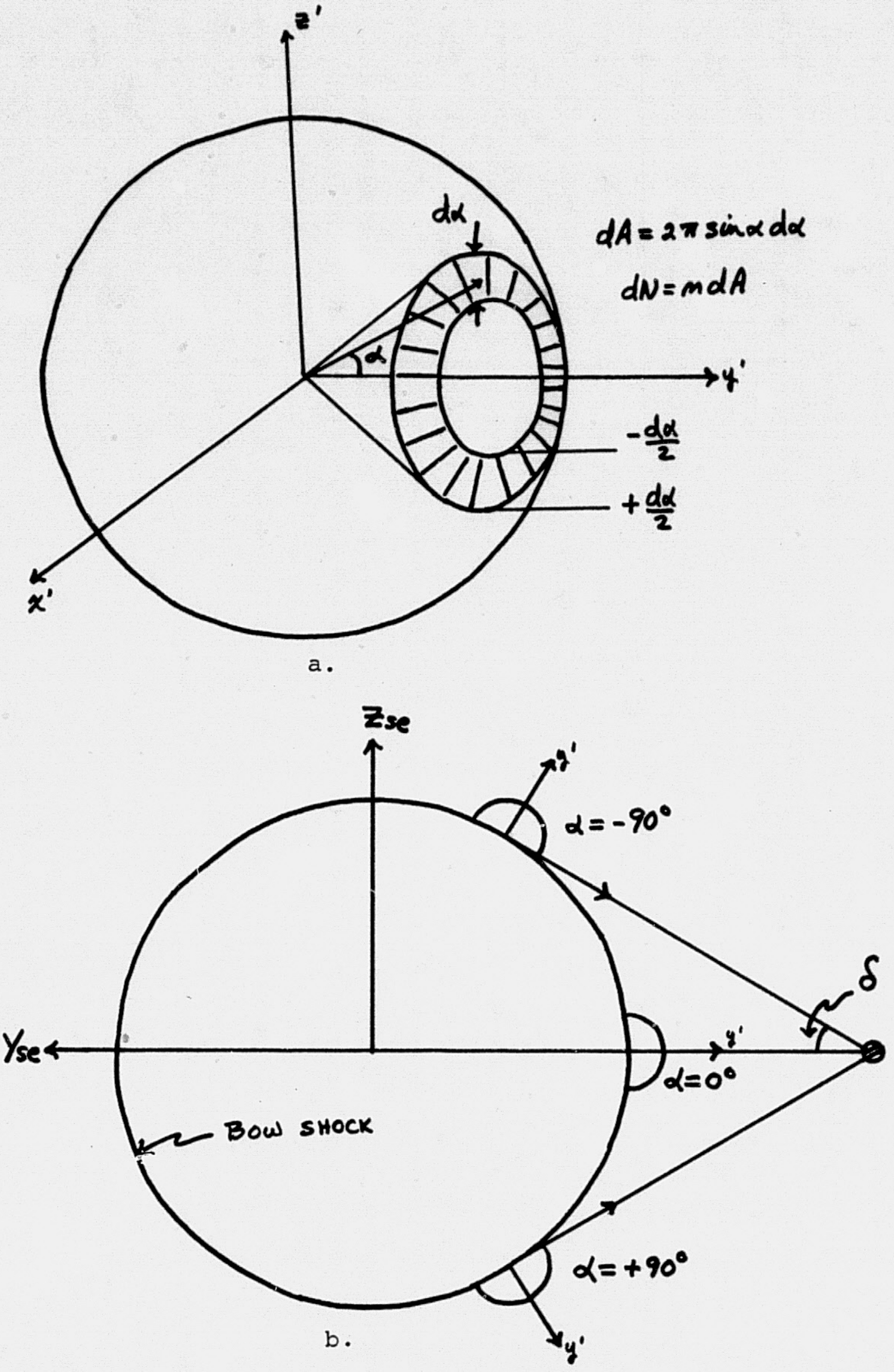
z'
dα
dA = 2π sinα dα
dN = m dA
α
y'
$-\frac{d\alpha}{2}$
$+\frac{d\alpha}{2}$
x'
Zse
y'
α = -90°
δ
Yse
y'
α=0°
BOW SHOCK
α= +90°
y'

a.

b.

Figure 4-5

In the computer model, n was chosen to be of the same order of magnitude as observed in the data and pitch angle intervals, $\Delta\alpha$, of 10° were used. The initial values of the energies ranged from 10 eV to 3500 eV.

4.5 Acceptance Criteria

There are essentially two criteria to consider in determining whether or not a particle is to be counted by the detector on the lunar surface.

1.) the particle must* come from the direction in which the detector is looking and

2.) the particle must have a source point on the surface of the shock.

*(it is possible to relax this criterion under certain circumstances; see discussion in chapter 5). Due to the finite size of the detector look cone, there is more than one direction from which the particles can come and still enter the detector. If δ is the angle associated with the look cone, then since $\vec{V}_r$ determines the direction of the guiding center path and $\hat{D}$ determines the look direction of the detector, a particle can enter the detector if the following relation is satisfied.

$$\hat{V}_r \cdot \hat{D} \geq \cos\delta \qquad 4\text{-}19$$

The vector $\vec{V}_r$, determines the direction in space of the guiding center trajectory and the vector $\vec{r}$ determines the point in space through which the particle must pass. If the line, determined by $\vec{V}_r$ and the point $\vec{r}$, intersects the surface of the shock, then a source point exists. The equation of a line in three dimensions, passing through the point $\vec{r}$, with direction $\vec{V}_r$, is,

$$\frac{x - r_x}{V_{rx}} = \frac{y - r_y}{V_{ry}} = \frac{z - r_z}{V_{rz}} \qquad 4\text{-}20$$

The simultaneous solution of this equation and the equation of the paraboloid of revolution eq. 4-14, yields a quadratic in any of the variables x,y, or z. Then if the discriminant, $(B^2 - 4 A C)^{1/2}$ is real, that is if

$$B^2 \geq 4 A C \qquad 4\text{-}21$$

a source point exists. In the case of a quadratic in y,

$$B = (D^2 V_{rx})/(d\ V_{ry}) - 2(V_{rz}/V_{ry})\left((V_{rz}/V_{ry})r_y - r_z\right)$$

$$A = 1 + \left(V_{rz}/V_{ry}\right)^2 \qquad 4\text{-}22$$

$$C = D^2(r_x/d) + \left[(V_{rz}/V_{ry})^2 r_y^2 - 2\, r_y r_z (V_{rz}/V_{ry}) + r_z^2\right]$$
$$-D^2 - (D^2 r_y\ V_{rx}/d\ V_{ry})$$

It is now possible to outline the scheme for generating data with the computer model.

a.) the moon is advanced in the orbit by incrementing the time, thus determining the position $\vec{r}(t)$, and the detector look direction $\hat{D}(t)$.

b.) at each position, the values of $\vec{V}_r\ (\xi, a)$ are calculated based on $\vec{B}$ and $\vec{V}_{sw}$.

c.) the tests $\hat{V}_r\ (\xi, a)\cdot\hat{D} \geq \cos\delta$, and $B^2 \geq 4\ A\ C$ are performed and if they are both satisfied, $dN\ (\xi, a)$ is stored in the appropriate energy channel.

To allow for the higher band pass at higher energies, all particles from energy $\xi - \frac{\Delta\xi}{2}$ to $\xi + \frac{\Delta\xi}{2}$ that satisfy the conditions described above, should be counted in the energy channel ξ. Due to the large amount of computer time required to test a nearly continuous range of energies, only the twenty center energies were used and each $dN\ (\xi, a)$ was multiplied by 10% of the center energy. This is in keeping with the qualitative nature of the model.

Hidden in this technique is a numerical integration of the source points over the surface of the bow shock. That is, by making the above tests at each position $\vec{r}$, over a wide range of energies and pitch angles, each source point that contributes a particle that satisfies the tests is counted. This can be seen by examining the special case shown in figure 4-5b.

Chapter 5

5.1 Introduction

Two basic approaches were followed in the analysis of particle data and interplanetary magnetic field data to determine whether or not the physical processes, discussed in chapter 3 are in operation in the pre and post bow shock regions of the lunar orbit.

The first approach consisted of searching for the expected correlation in interplanetary field configuration and observability of particles with the detector on the lunar surface while the second approach consisted of attempting to generate synthetic SIDE data, using the computer model and to discover in which ways these data resembled the real data.

Simultaneous particle and magnetic field data were available from the Apollo 14 SIDE and Explorer 35 magnetometer respectively, for three periods of interest during May and June of 1972. The magnetometer data tapes were provided by D.S. Colburn, Ames Research Center, Moffet Field, California. The regions in the lunar orbit corresponding to these periods and their associated times are shown in figure 5-1. Discussions of the analysis and results of the analysis of these data follow under the subtitles of Real Data and Synthetic Data.

Figure 5-1. The three regions of the lunar orbit in which magnetometer and ion data were collected for the analysis done in this thesis. The distance between the tick marks represents the distance traveled by the moon in 1 day.

Lunation 17, 1972

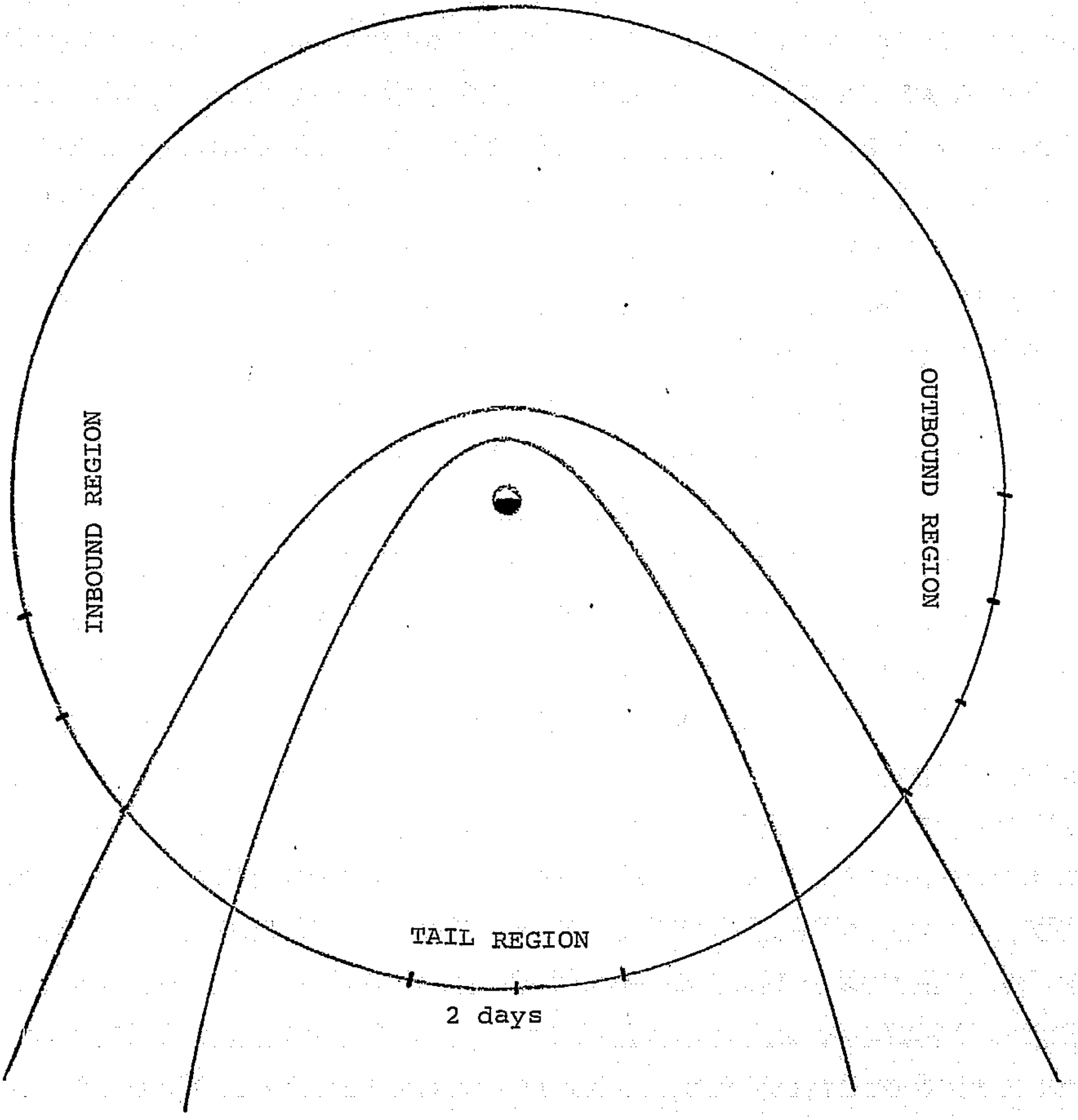

REGION	from	to	
INBOUND	$141^{d}16^{h}21^{m}$	$143^{d}16^{h}21^{m}$	141=May 20
TAIL	$148^{d}0^{h}1^{m}$	$150^{d}0^{h}1^{m}$	148=May 27
OUTBOUND	$153^{d}19^{h}24^{m}$	$156^{d}19^{h}24^{m}$	153=June 1

Figure 5-1

5.2 Real Data

In order to determine whether or not any correlation between B field configuration and particles observed exists in the data, it is necessary to devise a technique of comparing the known B field components with the known particle accumulations of the SIDE for the same time interval.

The obvious thing that comes to mind is to simply plot the component of the field of interest and the integral particle flux for the same time interval and visually inspect these plots for any correlation. An attempt at this procedure was made and the result is shown in figure 5-2. Although a weak visual correlation is evident from these data, it is obvious that no concrete conclusions can be drawn from this type of analysis. In order to overcome this problem, we could divide this plot into small time intervals and consider each interval separately, noting the value of the field latitude and the number of particles observed at that latitude for each interval. That is, we would be interested in constructing from the data, a plot of the average number of particles observed when the interplanetary $\vec{B}$ field has a particular configuration vs. the field configuration.

Such an analysis was done using the SDS 910 computer and data tapes from the Apollo 14 SIDE and the Explorer 35 magnetometer.

Correlations in solar ecliptic latitude of the field and solar ecliptic longitude of the field, separately, were sought as were correlations with the field latitude and longitude considered jointly. Details of the computer analysis can be found in the appendix on computer programs.

5.3 Results from the Real Data

The results of the analysis using the real data are shown in figure 3 through 12 of this chapter, for the three periods of interest, which will henceforth be referred to as the inbound, tail and outbound regions. The inbound region corresponds to the pre-shock crossing region and the outbound region corresponds to the post-shock crossing region of the lunar orbit. The inbound region consists of two days of data taken prior to entering the magnetosheath, beginning at $141^d\ 16^h$. The tail region begins at $148^d\ 0^h$ and continues for two days; this period is entirely in the geomagnetic tail and the analysis in this region was done as a check on the validity of this technique. The outbound regions begins about 3 hours after shock crossing at $153^d\ 19^h\ 24^m$ and extends for three days toward the sunset terminator.

The format of the first three graphs is designed to show the average number of counts observed at a given solar ecliptic latitude of the field vs. the latitude and the frequency of occurence of that latitude in units of, number of times

Figure 5-2. Visual correlation of field latitude and integral flux. A correlation is especially apparent in the second half of this event.

Figure 5-3. Correlation of average integral counts and SE latitude of B over the inbound region. Bottom part of the graph shows the number of times a particular value of the latitude was encountered in the two day period over which this analysis was done.

Figure 5-4. Lack of correlation in field latitude and counts in the tail region is apparent in this figure.

Figure 5-5. Correlation of field latitude and counts. Note the broad central peak indicating that particles are preferentially observed when the field is near the ecliptic plane. The enrichment of the high positive latitudes of this distribution is due to lunar atmospheric ions.

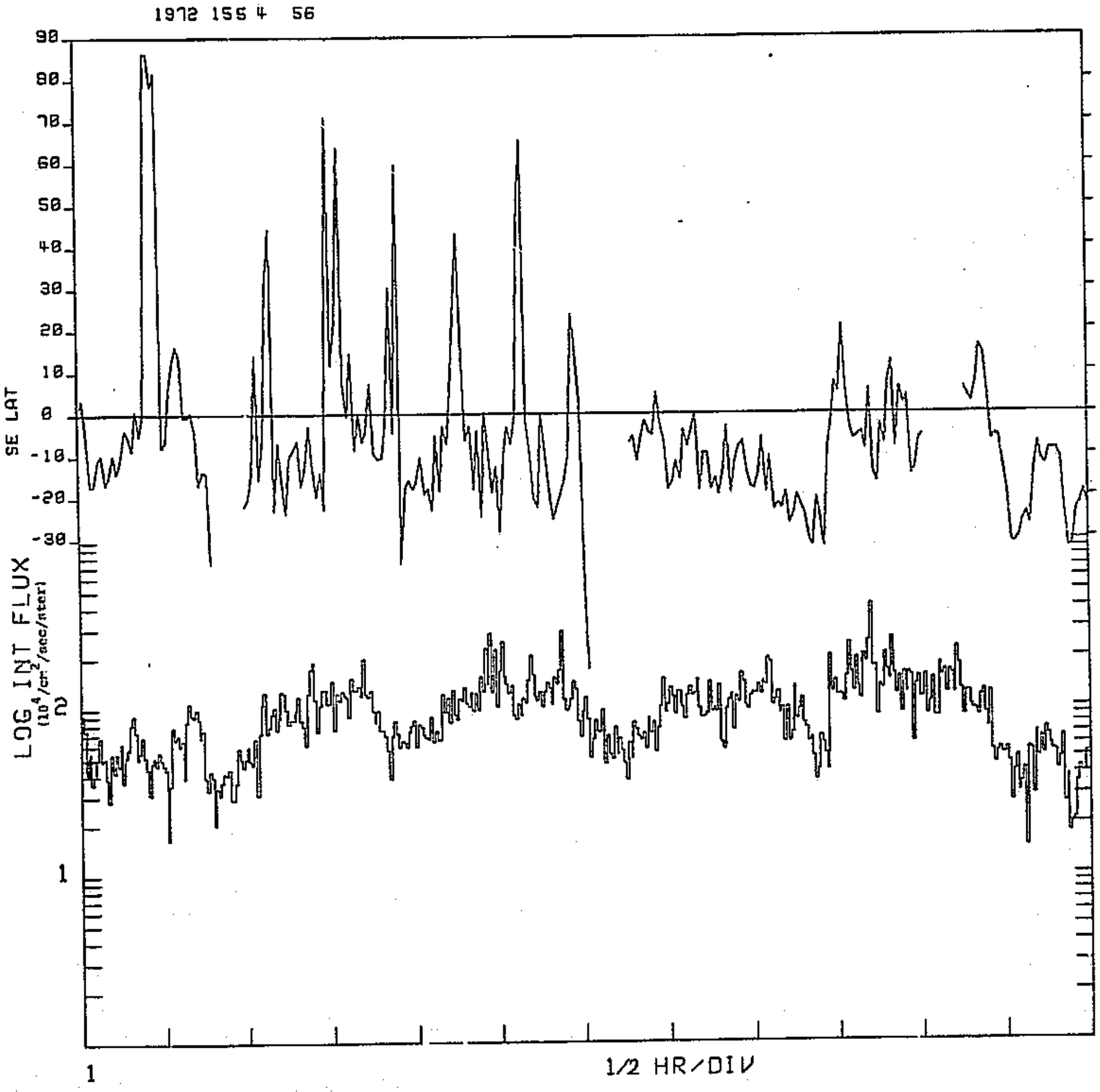
1972 155 4 56
90
80
70
60
50
40
30
20
10
0
-10
-20
-30
SE LAT
LOG INT FLUX
(10⁴/cm²/sec/ster)
2
1
1
1/2 HR/DIV

Figure 5-2

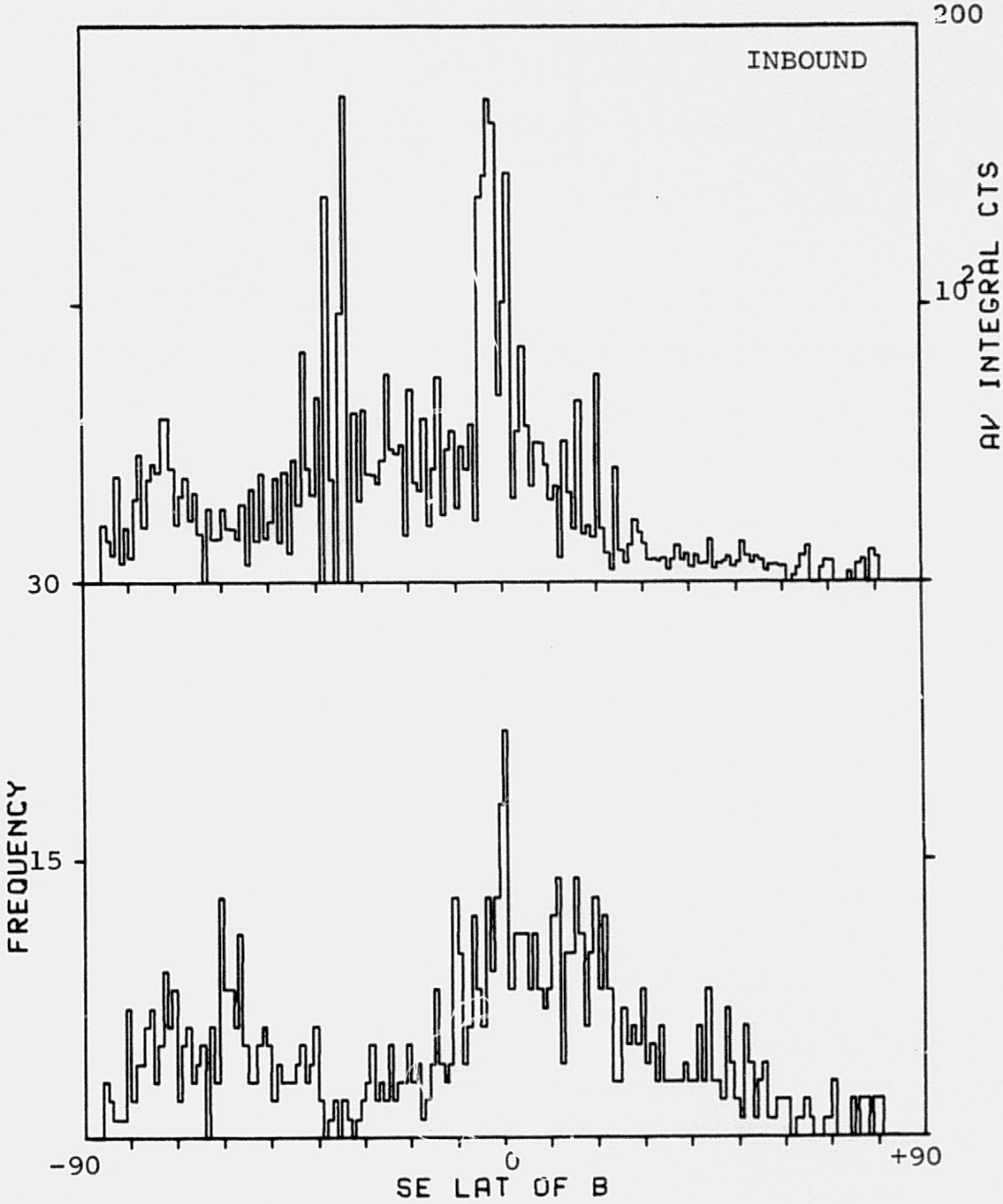
200
INBOUND
AV INTEGRAL CTS
10^2
30
FREQUENCY
15
-90
0
+90
SE LAT OF B

Figure 5-3

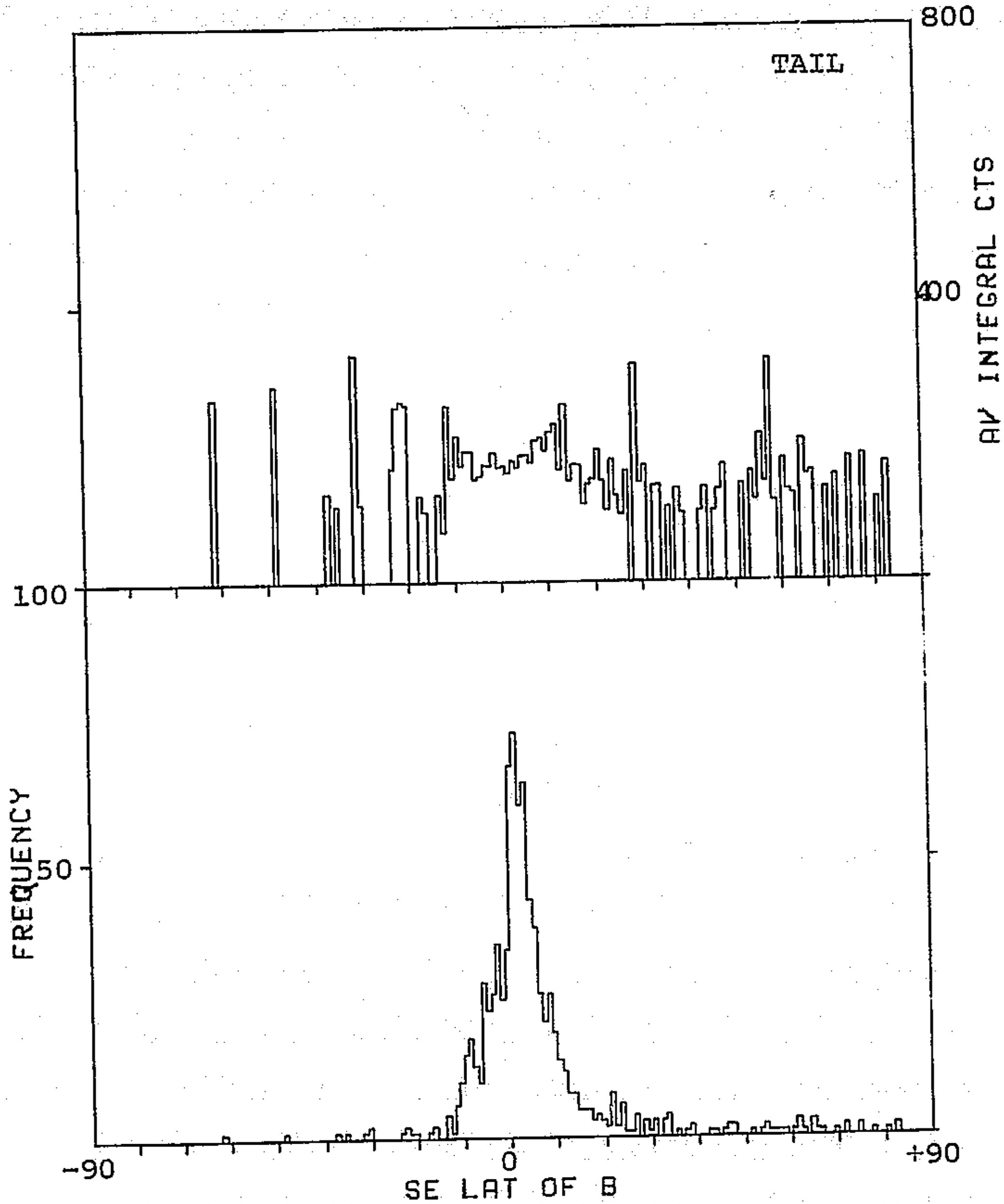
TAIL
800
400
AV INTEGRAL CTS
100
50
FREQUENCY
-90
0
+90
SE LAT OF B

Figure 5-4

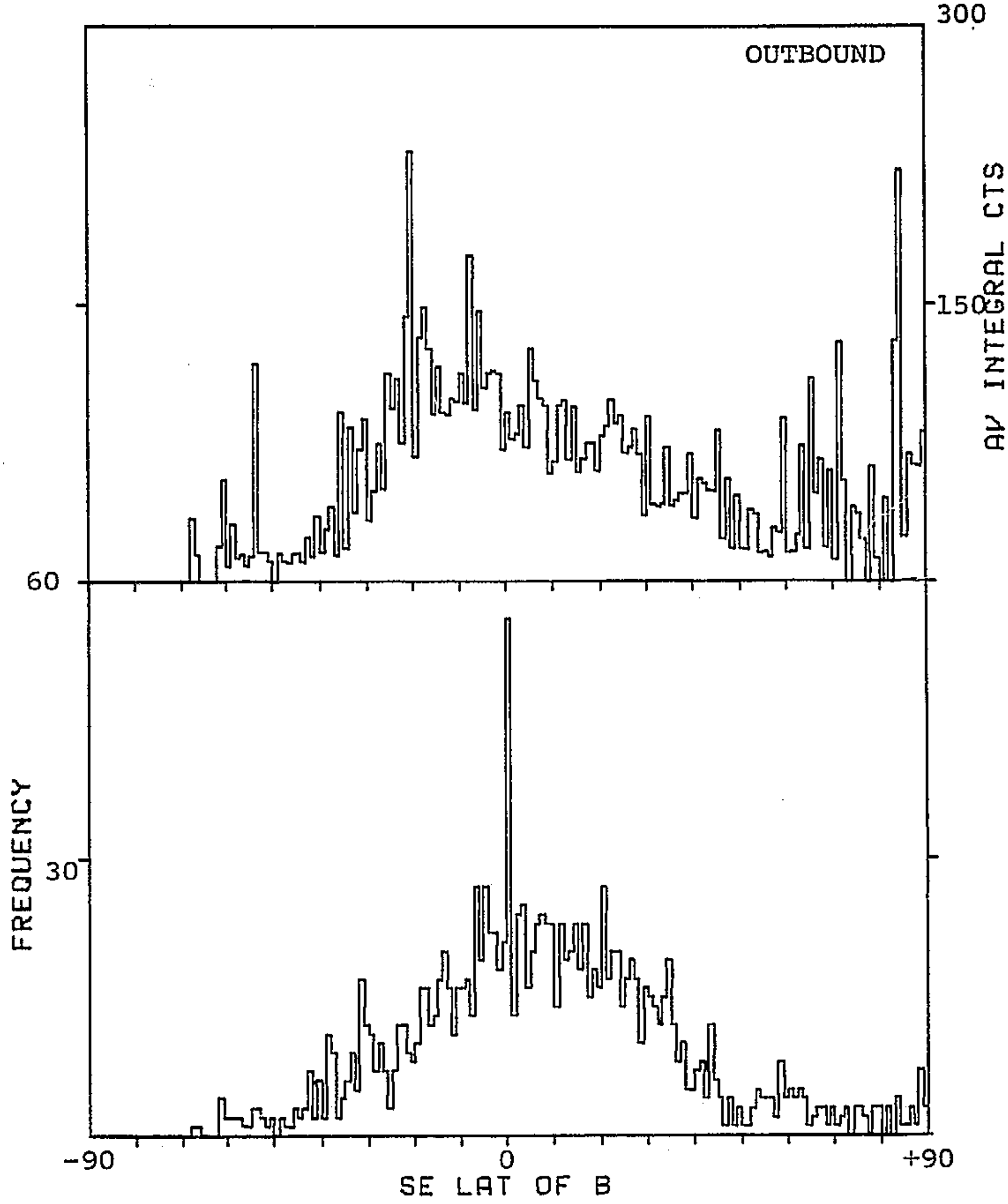
300
OUTBOUND
150
AV INTEGRAL CTS
60
FREQUENCY
30
-90
0
+90
SE LAT OF B

Figure 5-5

observed per number of days of observation vs. the latitude. That is the lower portion of each graph displays simply the number of times a particular value of the field latitude was observed during the two or three day period of observation and the upper portion of each graph displays the average number of particles observed when at that latitude. Average integral counts will be taken to mean the average that is obtained by dividing the total number of particles accumulated at a particular latitude over the period of observation by the total number of times that that particular value of the latitude was observed during the same period.

Due to the fact that the energy bandpass of the detector is proportional to the center energy, using counts instead of integral flux does not always provide a clear physical picture from the data. In view of this, the distributions of observed flux vs. field latitude were calculated for the three regions as a check on the validity of using counts for this analysis. The results are shown in figure 5-6. By comparing these results with those in figures 5-3 through 5-5, it is clear that using counts does not substantially change the form of the distributions. Comparison of the two results for the inbound region does show a fairly large inflation of the high negative latitudes in the integral flux representation that is not as apparent in the representation using counts. The reason for this is that the events that caused the inflation have lower energies ($\xi \leq 500$ eV) than those of the broad central peak. Using integral flux tends to amplify the lower energies due to the smaller bandpass at these energies. The particles found in the upper and lower ends of the distributions of figures 5-3 to 5-6 are due largely to lunar atmospheric ions that are accelerated by the interplanetary electric field and the effect of these particles on the present analysis is discussed more fully in chapter 6.

The distributions shown in figures 5-7 to 5-9 are analogous to those in figures 5-3 to 5-5 where the solar ecliptic longitude of the field was the parameter of interest. It should be noted that the analysis was carried out here using the uncorrected values of the field longitude. This has no bearing on the physical results, and in any physical interpretation of these results, the scale in longitude may be simply shifted by 28°, i.e. the corrected value of the longitude is obtained by adding 28° to the uncorrected value. For a discussion of the error in longitude and the technique used to correct for it, see chapter 2.

The last three graphs of this series display the results of considering the latitude and longitude jointly. The evaluation of the parameters in this treatment is over wider intervals, 10° latitude by 20° longitude, but the same procedure was used to determine the value in each two dimensional

Figure 5-6. Correlation in field latitude and integral flux. High latitude events are enhanced by the geometric factors. (see Appendix 3).

Figure 5-7. Correlation of field longitude with counts for the inbound region. The distribution exhibits a double peak but is not well defined due to the scarcity of data for this region.

Figure 5-8. Unexpected correlation in field longitude and counts in the geomagnetic tail. Note the well defined peaks in the frequency distribution and the difference in height of the two major peaks in the counts distribution.

Figure 5-9. Correlation in field longitude and counts for the outbound region. The two major peaks are about 180° apart.

Figure 5-10 through 5-12. Correlations of field latitude and longitude considered simultaneously with average integral counts. These plots contain basically the same information that is in figures 5-3 through 5-9.

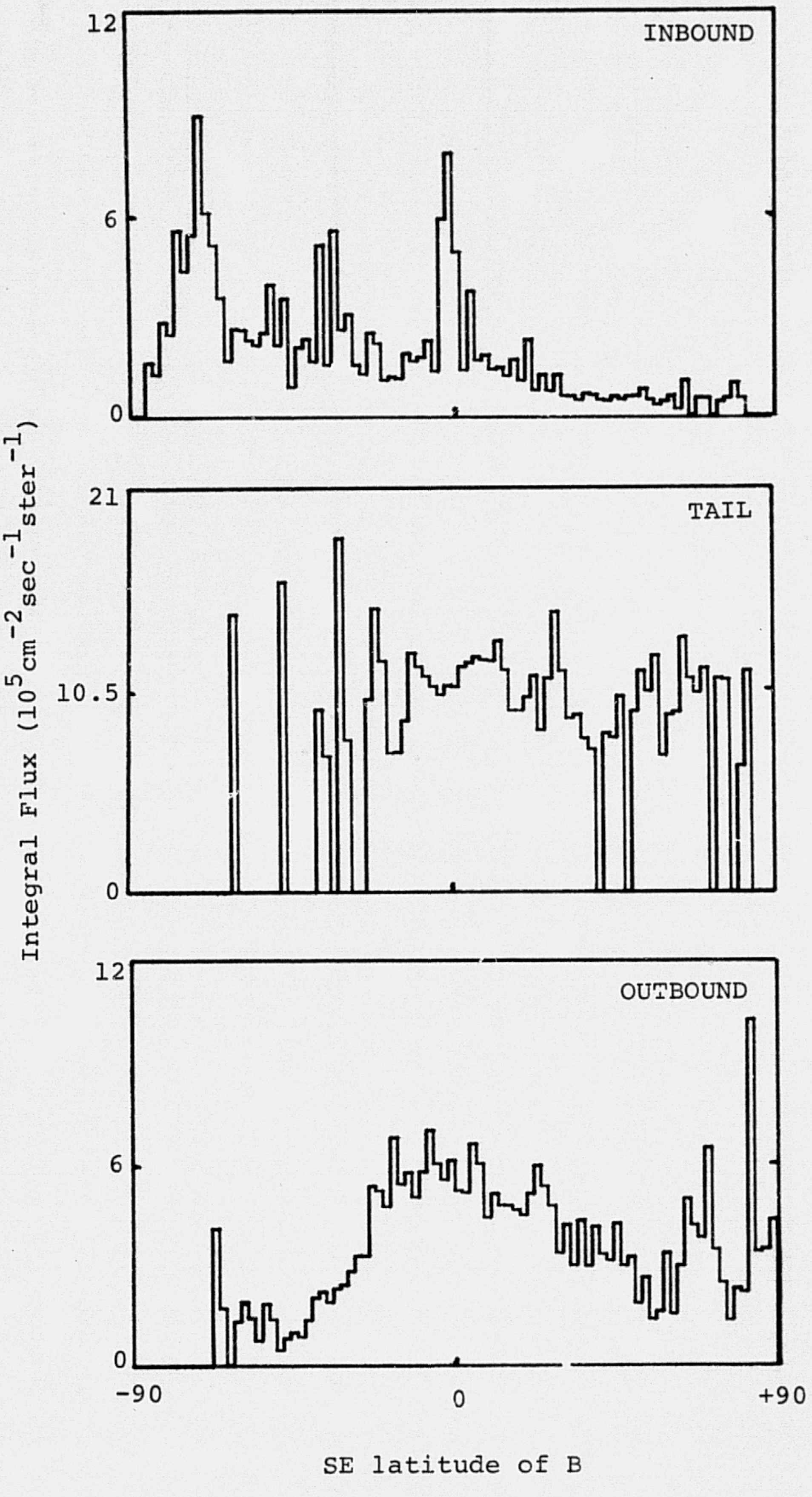
12
INBOUND
6
0
21
TAIL
10.5
0
12
OUTBOUND
6
0
-90
0
+90
Integral Flux $(10^5 cm^{-2} sec^{-1} ster^{-1})$
SE latitude of B

Figure 5-6

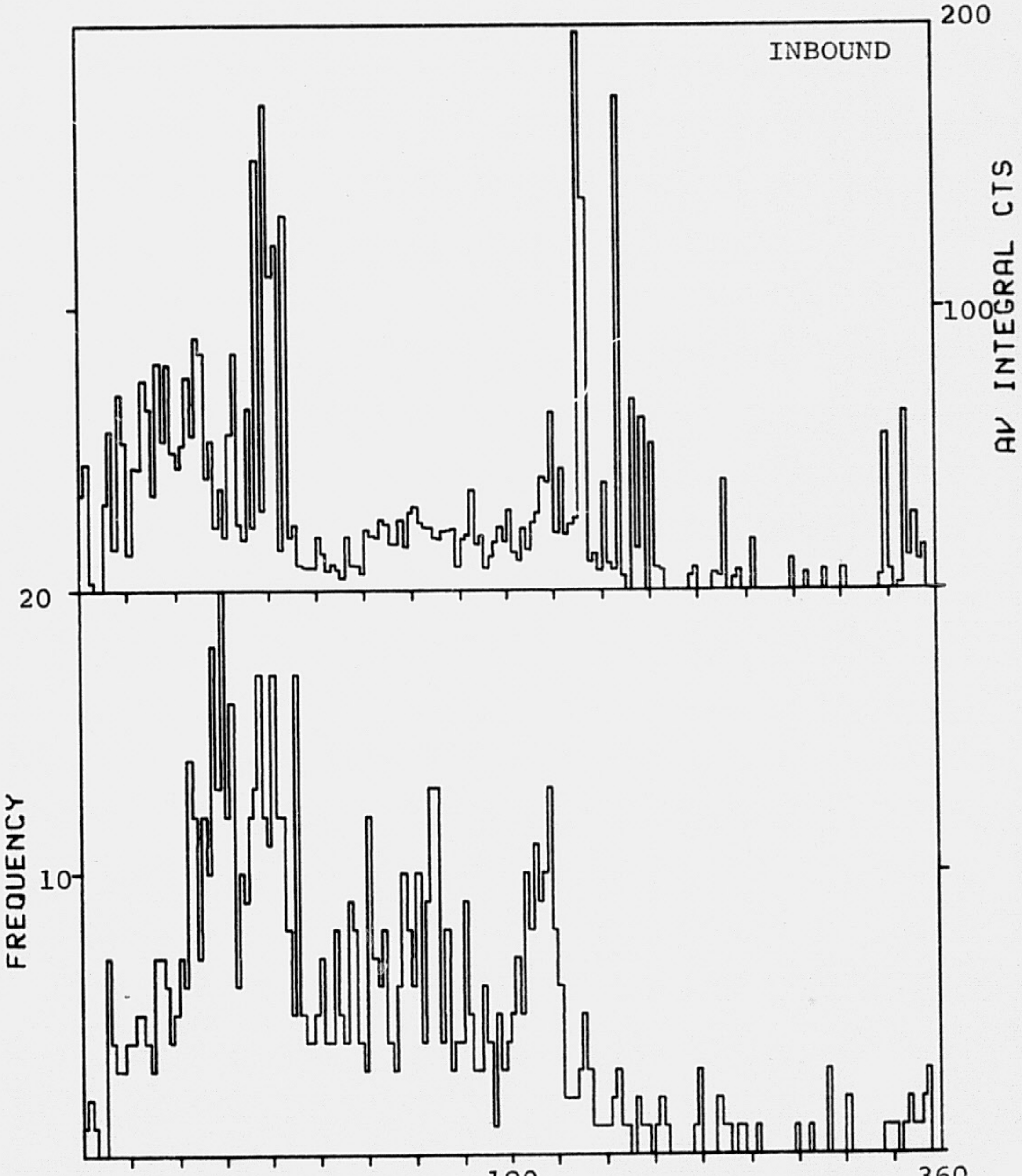
INBOUND
200
100
AV INTEGRAL CTS
20
10
FREQUENCY
0
180
360
SE LON OF B

Figure 5-7

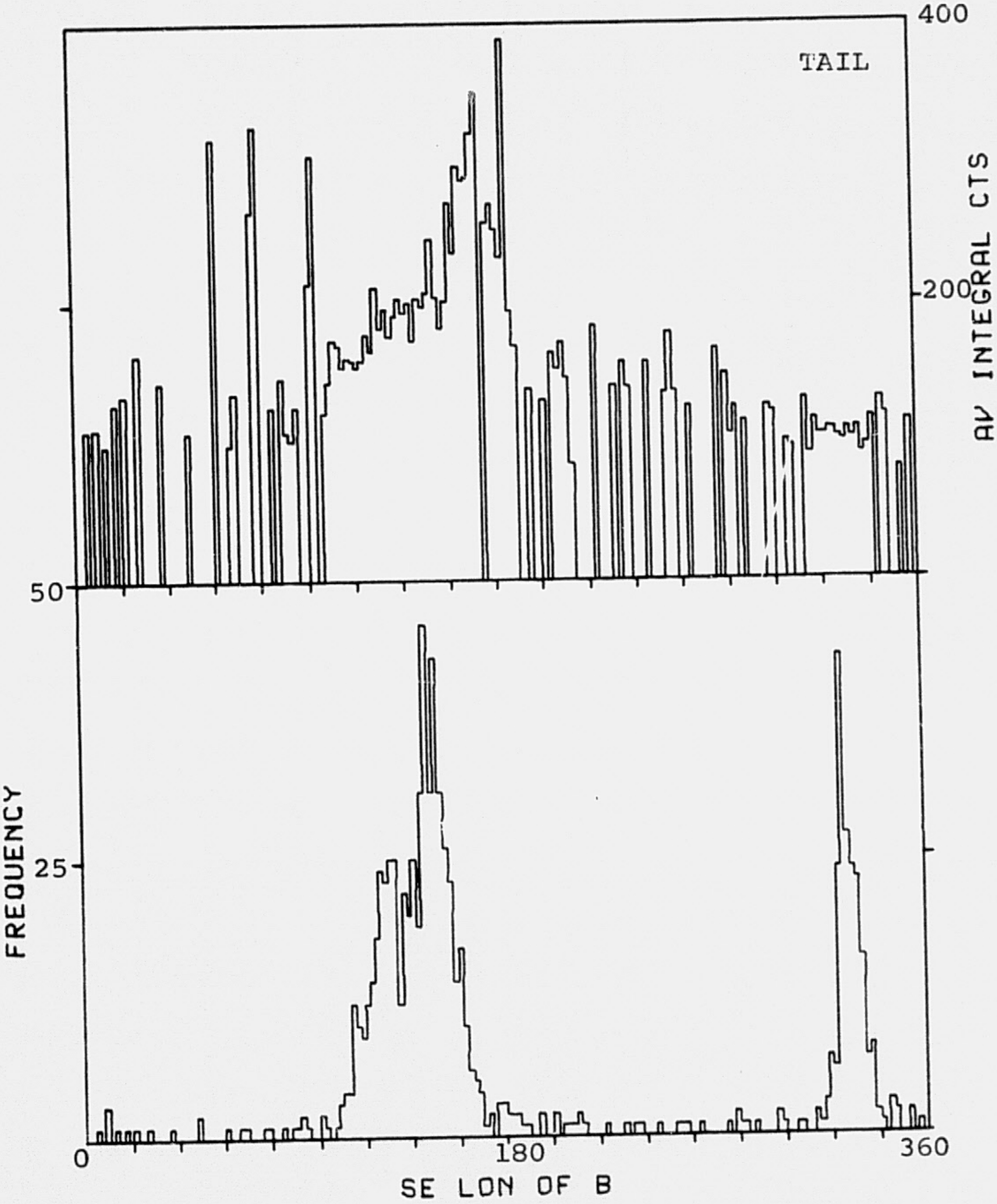
TAIL
400
200
AV INTEGRAL CTS
50
FREQUENCY
25
0
180
360
SE LON OF B

Figure 5-8

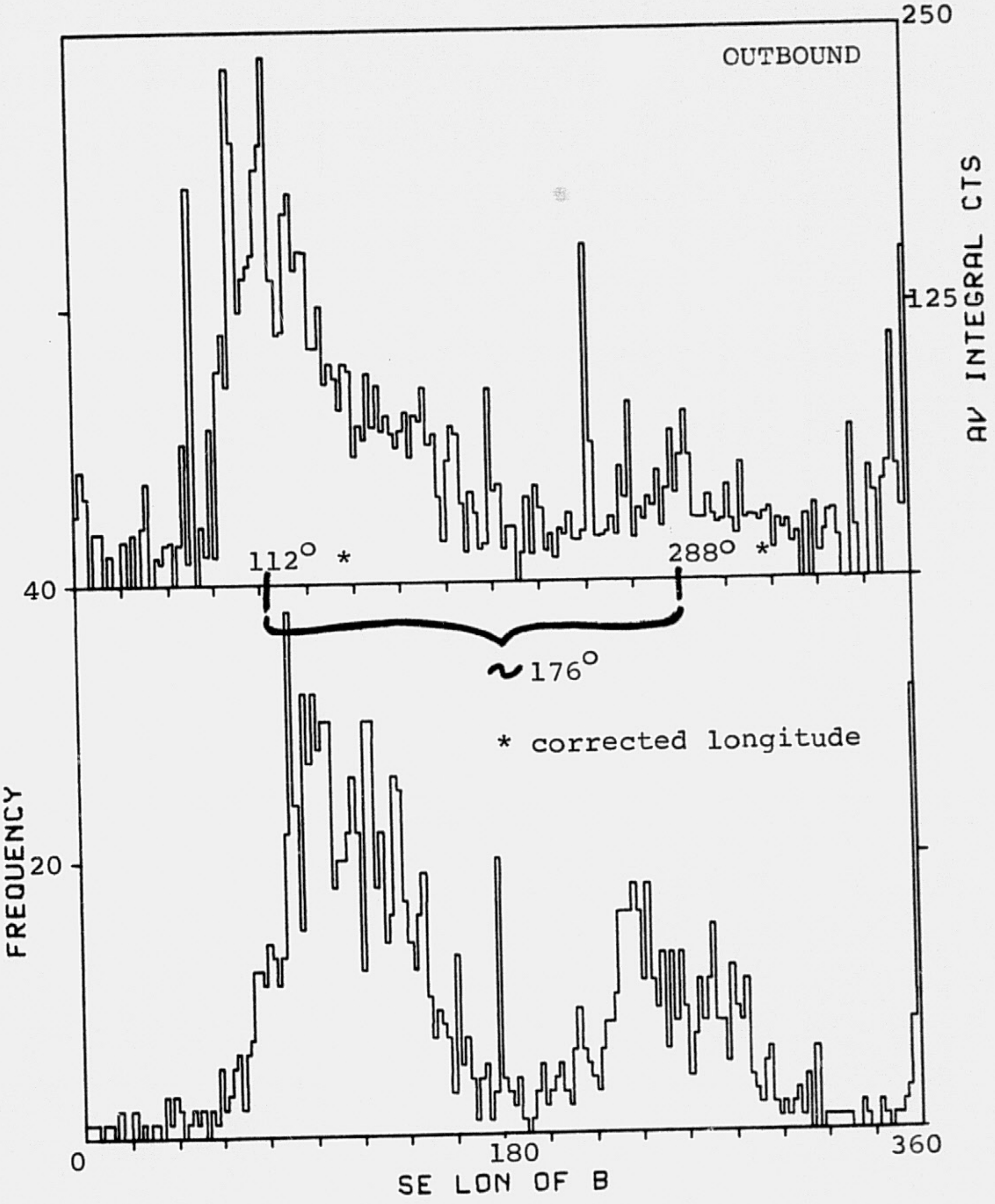
250
OUTBOUND
AV INTEGRAL CTS
125
112° *
288° *
40
~176°
* corrected longitude
FREQUENCY
20
0
180
360
SE LON OF B

Figure 5-9

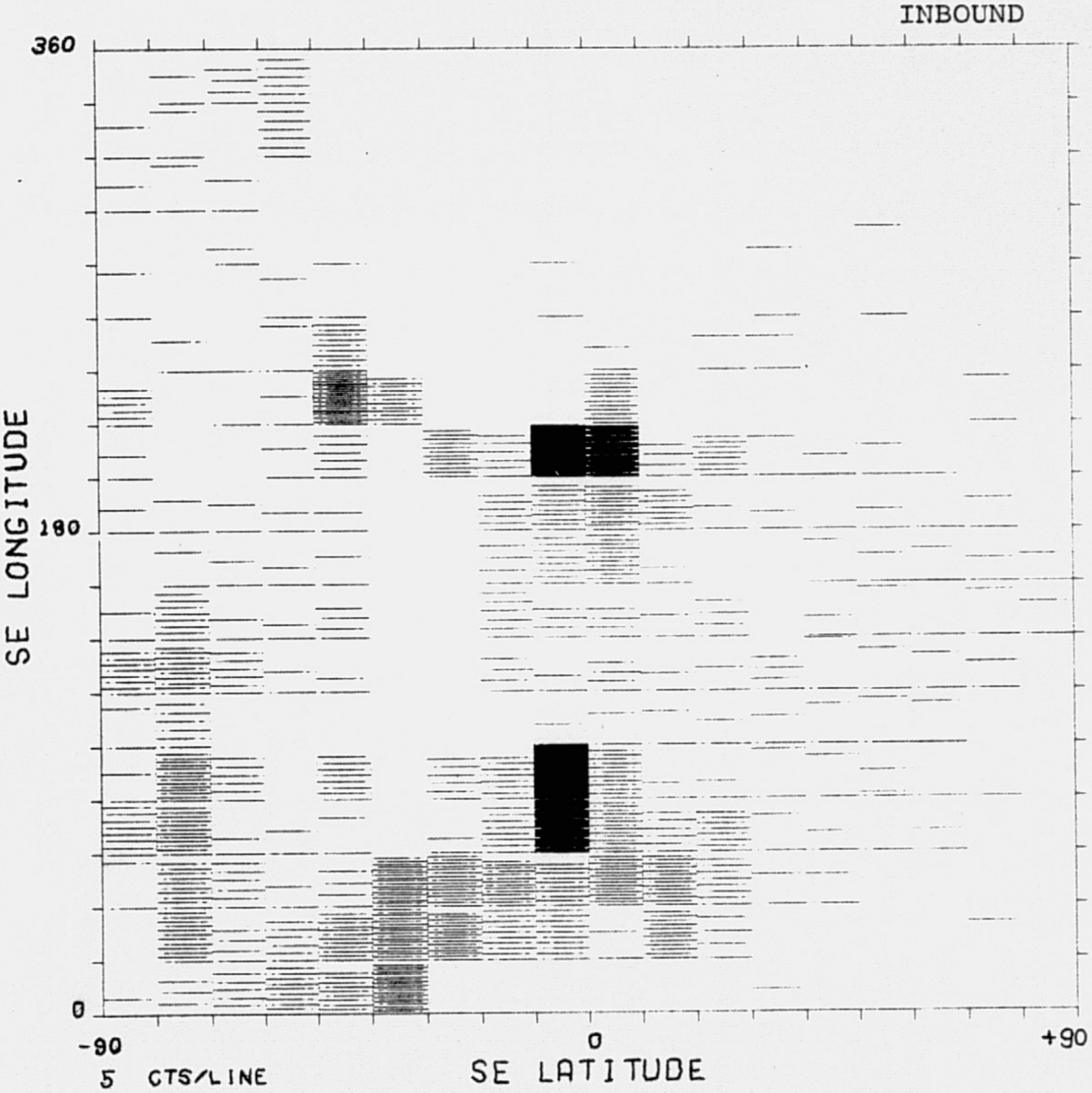

Figure 5-10

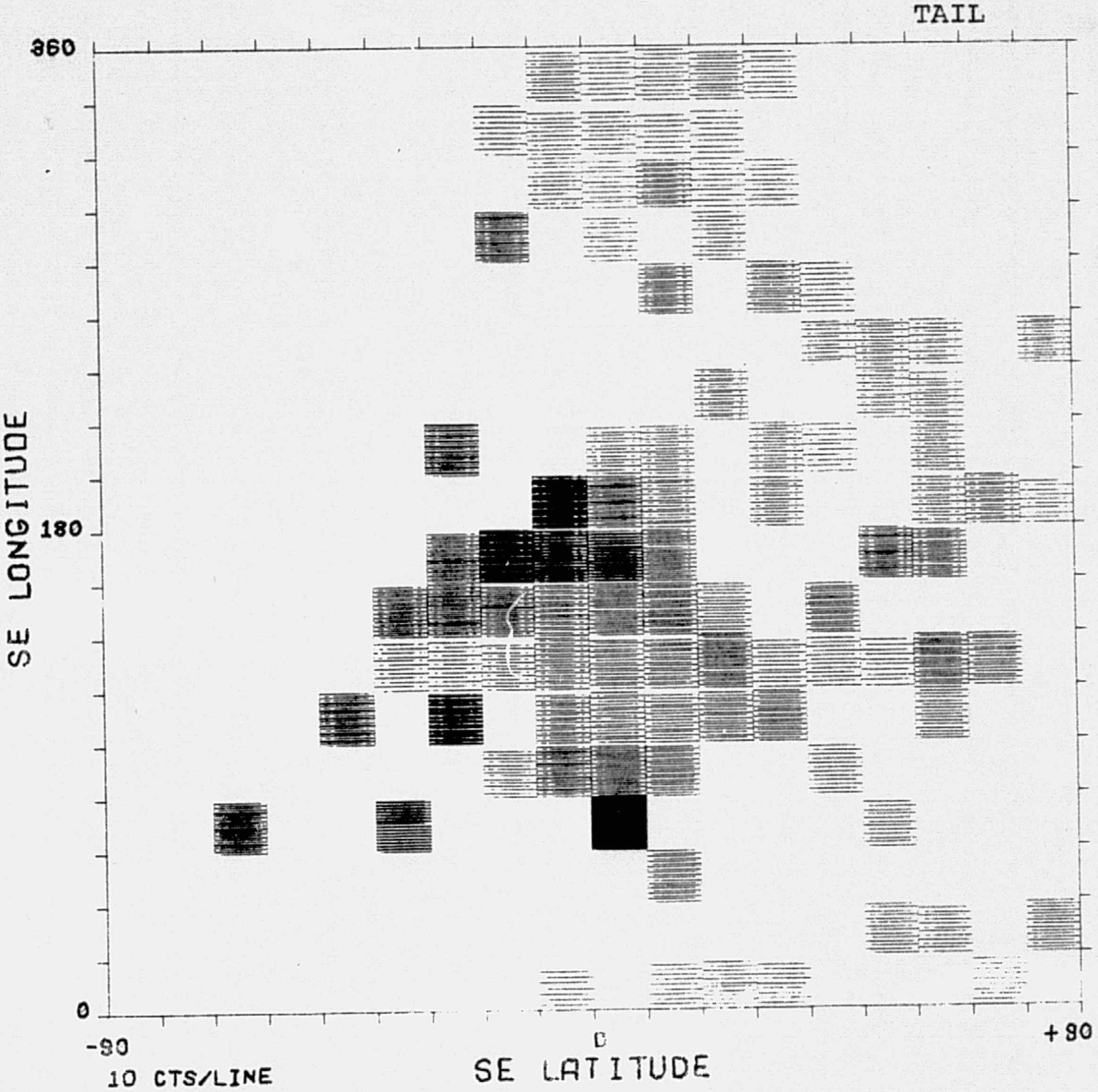

Figure 5-11

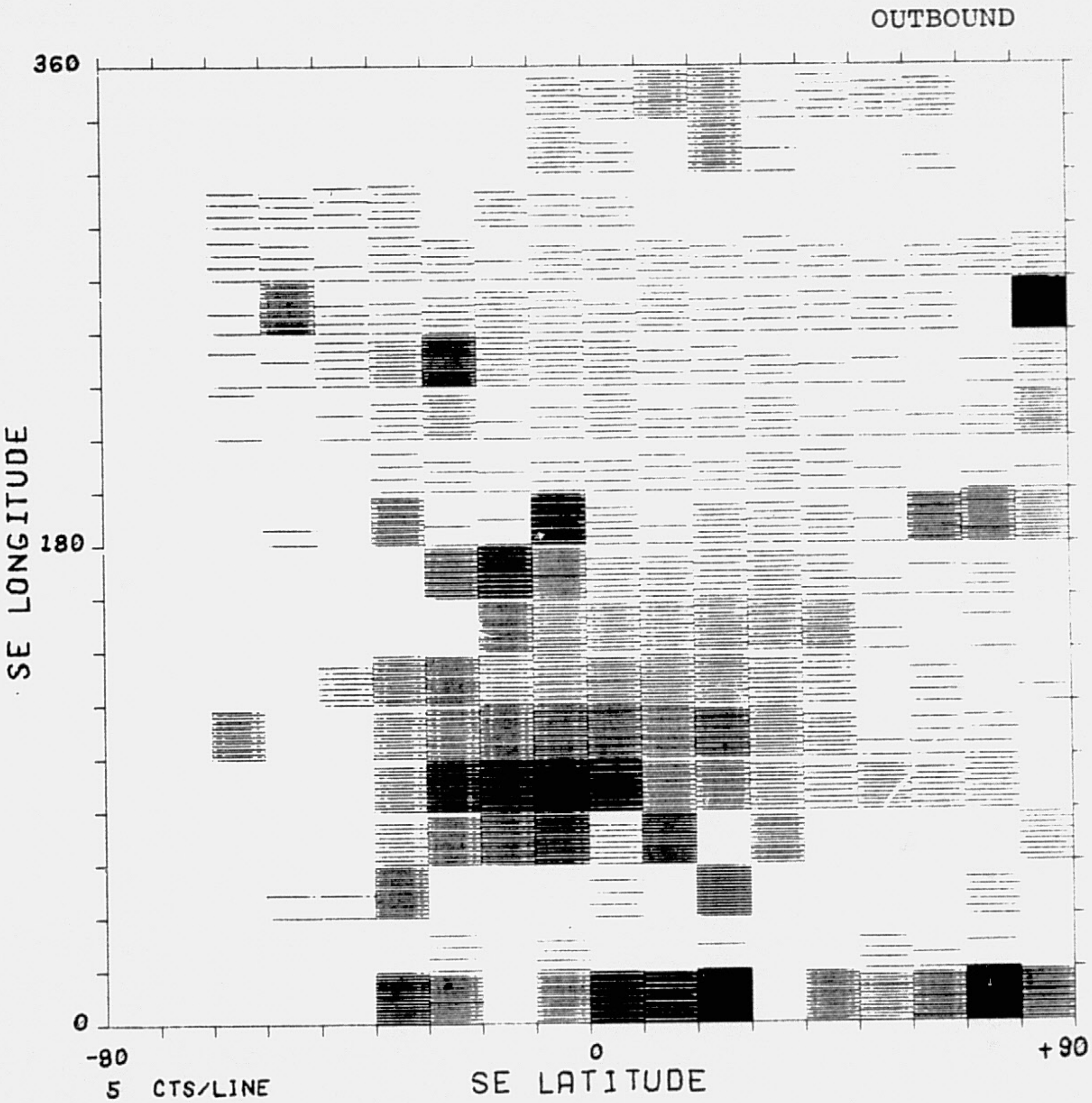

Figure 5-12

interval. The average integral counts in each interval of the grid is represented by the number of lines in that interval where each line represents five or ten counts. The absolute value of any of the numbers is of no consequence and no attempt is made here to display the numbers in a rigorously quantitative fashion. These graphs were also produced with uncorrected longitudes and the same correction angle may be applied to them as was done for the case involving only the longitude correlation.

After generally surveying these results, the first important conclusion that can be drawn is that there is indeed a correlation between interplanetary field parameters and particle observations by the SIDE at the lunar surface. This statement can be made on the assumption that if the number of particles observed by the detector did not depend on the configuration of the field, then the average number of particles observed at any given value of a field parameter would not be very different from the average number of particles observed at any other value of the field parameter. In fact, that is the reason for carrying out the analysis in the tail region. The mechanism of the model is not expected to be operative in the tail region and a lack of correlation in field latitude can be seen in figure 5-4. Although the latitude of the geomagnetic tail field is sharply peaked about 0° in frequency of occurence, the average number of particles observed at any of the latitudes is not too different from that observed at any other latitude. A clear lack of correlation in geomagnetic tail field longitude was not observed and this somewhat unexpected result will be discussed in a separate subsection below.

With the foregoing in mind, a correlation of interplanetary field latitude is apparent in figure 5-5 for the outbound region. A rather broadly peaked distribution is observed with the peak centered around -10 to -15 degrees, i.e. with the interplanetary $\vec{B}$ field near the ecliptic plane. Although the peak is not sharp, for reasons that will be discussed later, there is a tendency for more particles to be seen, on the average, when the field latitude has a value that is in the neighborhood of 0°, i.e. with $-25° \leq B_{lat} \leq +15°$. Particles are still seen, however, at high positive values of field latitude and these are probably due to the outwardly directed interplanetary E field at high positive latitudes that accelerates the particles directly into the detector. (see fig. 3-4)

The results for the inbound region, figure 5-3, are not as well defined, due primarily to the shorter period of observation, but again there is a broad peak that centers near 0° latitude with some particles still being seen at high negative values of the latitude. In the inbound region, if the field latitude has high negative values, the interplanetary

$\vec{E}$ field again points out into the detector on this side of the magnetosphere (see figure 3-4) accounting for these high negative latitude particles.

At this point it is possible to conclude that the observability of particles in the inbound and outbound regions of the lunar orbit is dependent on interplanetary field latitude and the dependence does roughly correspond to that expected from the model. In addition, there is indication from the data that the asymmetric interplanetary $\vec{E}$ field at high positive and negative values of the $\vec{B}$ field latitude is providing some of the particles observed by the detector in these regions.

Figure 5-9 shows a correlation in field longitude for the outbound region with a fairly obvious doubly peaked distribution, the first peak coming at about 84° uncorrected and the second smaller peak coming at about 264° uncorrected, a separation of 180° in longitude. One would also expect from the model a doubly peaked distribution with approximately the same size peaks, separated by about 180° since the polarity of the field is unimportant in determining the resultant guiding center trajectory of a particle for any particular value of the field latitude. For example, if the field latitude is say -10° while the longitude is 84° and +10° when the longitude is 264°, the same physical situation exists with respect to the model and the polarity is unimportant. If, however, the latitude is also -10° at the 264° position in longitude, a different physical situation doe exist and the guiding center trajectories will depend on the polarity of the field. Figure 5-13 illustrates this effect. Inspection of figure 5-12 reveals that the latitudes of the peaks in figure 5-9 are not too different. That is, different physical situations exist for the two peaks. The plane of the guiding center trajectories of case (1) in figure 5-13 makes a smaller angle with the plane of the lunar orbit than does the plane of guiding center trajectories of case(3), possibly accounting for the favorability of observing particles in case(1), i.e. the higher peak at about 84° longitude.

The data from the inbound region, figure 5-7, also show correlation in longitude of the field with the number of particles observed, but again, the shorter period of observation results in a less well defined distribution. Despite this, the distribution also shows a double peak with a less pronounced difference in height. A less pronounced difference in latitude for the two peaks is found by examining figure 5-10. The two peaks occur at latitudes much nearer the ecliptic plane thus lessening the effect shown in figure 5-13. These differences are consistent with the ideas discussed above concerning the actual physical situation occuring for the two different peaks.

Figure 5-13. Views in two different planes of the physically different situations ocurring for field configurations in which the longitudes are 180° out of phase and the latitudes are equal.

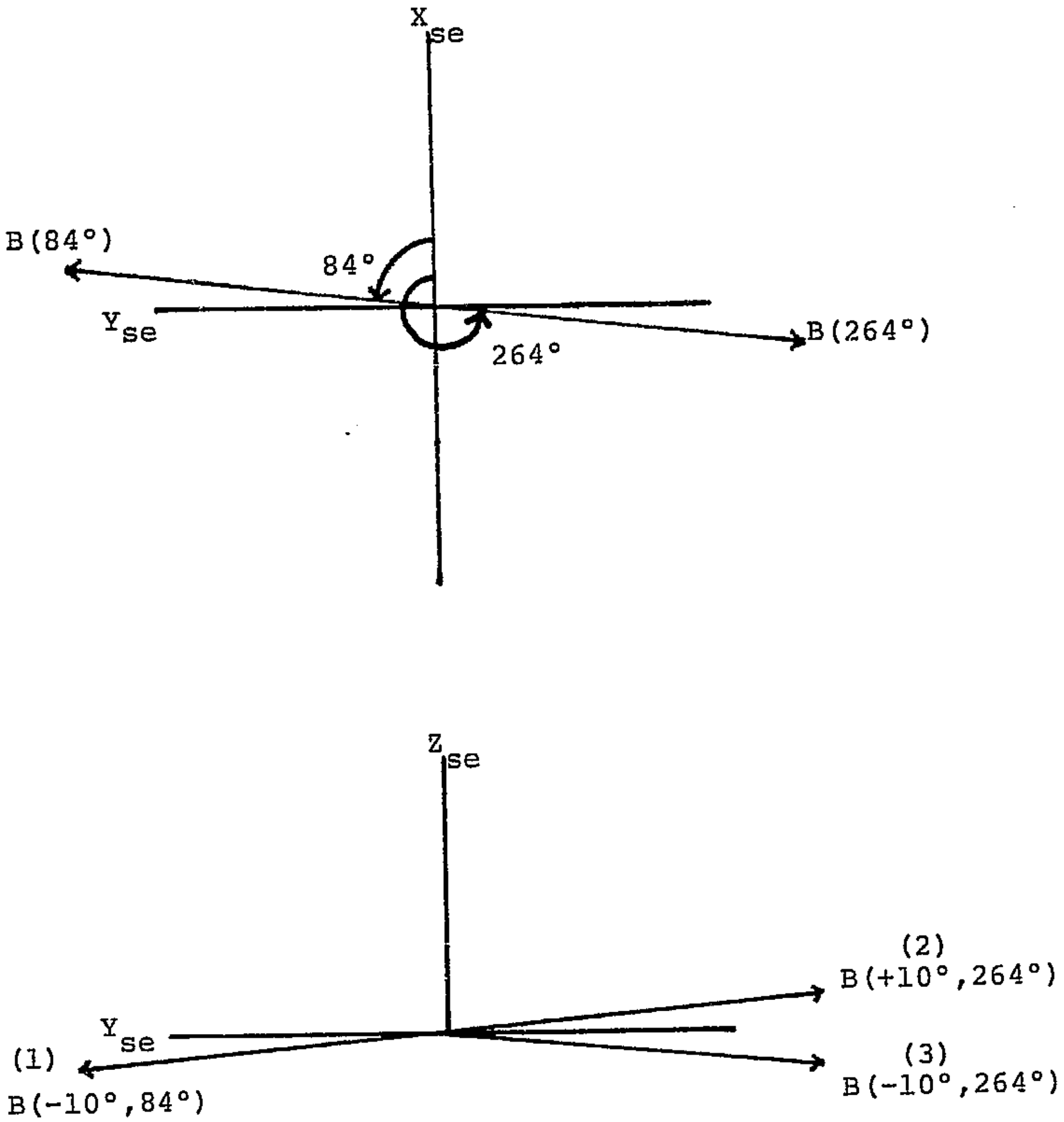

Cases 1 and 2 physically equivalent with respect to model

Cases 1 and 3 not physically equivalent

Cases 1 and 3 are favorable to observation of particles but case 1 is more favorable than case 3 according to the data in figure 5-8.

Figure 5-13

The results of the longitude analysis show that there is correlation in observability of particles with the SIDE and the solar ecliptic longitude of the interplanetary $\vec{B}$ field and this correlation further supports the model discussed in chapter 3.

5.4 Interpretation of tail passage

As mentioned above, figure 5-8, exhibits a doubly peaked distribution with the peak corresponding to the field of the geomagnetic tail pointing in an anti-solar direction at about a factor of 2 greater than the peak corresponding to the tail field pointing in the solar direction. This may not be significant, but since there is no obvious lack of correlation in longitude and number of particles observed, the physical situation in this region should be examined more closely.

At the beginning of the tail region, ($148^d\ 0^h\ 1^m$), the solar ecliptic longitude of the geomagnetic tail field is fairly stable around 358°, corrected, or with the tail field approximately in the solar direction. At approximately $148^d\ 5^h$, the field longitude changes abruptly and becomes stable about the value 178°, or the anti-solar direction and remains there throughout the two day period. The fact that no more abrupt changes in field longitude, i.e. neutral sheet crossings, are observed over this period can be understood by looking at a diagram of how the relative distances from the ecliptic plane of the moon and the neutral sheet at the longitude of the moon vary with time over the tail region at 60 R_e. The curve R in figure 5-14 represents the distance of the neutral plane from the ecliptic plane at the longitude of the moon, taking into account the seasonal offset and the diurnal variation; an off axis pivot point is also assumed due to the effect of the solar wind aberration angle of $\sim 4°$. The curve d of figure 5-14 is simply the distance of the moon from the ecliptic plane at 60 R_e as it moves toward higher longitudes. The sense of the geomagnetic tail field, in the region in figure 5-14 that is above the curve R, is in the solar direction and the field has the opposite sense in the region beneath the curve R. The motions in this diagram should be considered from the point of view of an observer on the earth, looking in the anti-solar direction. The moon spends a short time in the northern lobe region of the tail field and then crosses into the southern lobe for the rest of this period.

All that can actually be concluded from the result in figure 5-8, is that there is a tendency for more particles to be seen by the detector on the average, when the tail field points in the anti-solar direction, i.e. toward the detector, than when the field points in the solar direction, away from the detector. Note that the detector looks earthward in this region of the orbit. There is evidence here for a shadowing

Figure 5-14. View from earth, looking in the anti-solar direction. Curve R represents the distance in R_e of the magnetic neutral plane from the ecliptic plane as a function of time. Curve d represents the path of the moon with respect to the ecliptic plane for the same time period. Note that the moon spends most of the two day period in the southern lobe of the earth's field.

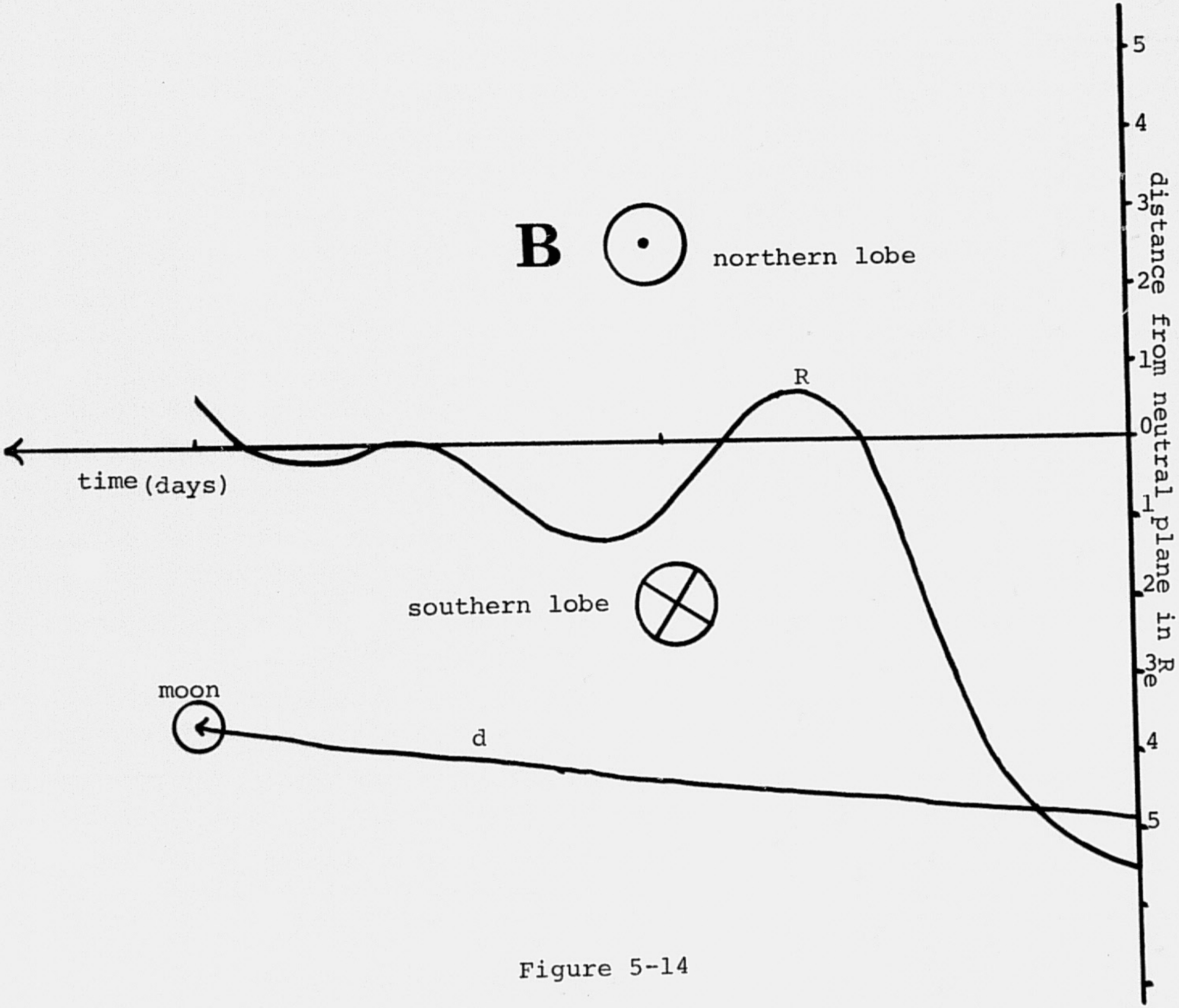

B
northern lobe
R
time (days)
southern lobe
moon
d
distance from neutral plane in R_e
5
4
3
2
1
0
1
2
3
4
5

Figure 5-14

effect by the moon. Van Allen et al. [1971], have suggested a model by which thermal anisotropies in the solar wind can provide an asymmetric access of protons to the magnetosphere. The basic idea of this model is that interplanetary field lines connect to geomagnetic field lines in the distant magnetotail ($\sim 100\ R_e$). When the interplanetary field has a southward component and is directed away from the sun it connects to the tail field lines as shown in figure 5-15. It can be seen from examination of this figure that the possible shadowing seen in the present analysis is consistent with the Van Allen model. By examining other features of the data in this region, for example the energy spectra, a better determination of the origin of this phenomenon could be made.

5.5 Synthetic Data

The basic philosophy underlying the second approach has been described in chapters 3 and 4 and the results of the application of that philosophy and a brief restatement of the scheme for generating the synthetic data are given in the following sections.

5.6 Brief restatement of the scheme

a.) the position vector $\vec{r}(t)$ and the detector look direction $\hat{D}(t)$ are calculated.

Figure 5-15. Van Allen model for asymmetric access of solar wind protons into the magnetosphere. The clustered arrows on the field lines represent proton thermal anisotropies in the solar wind. [Van Allen et al. (1971)].

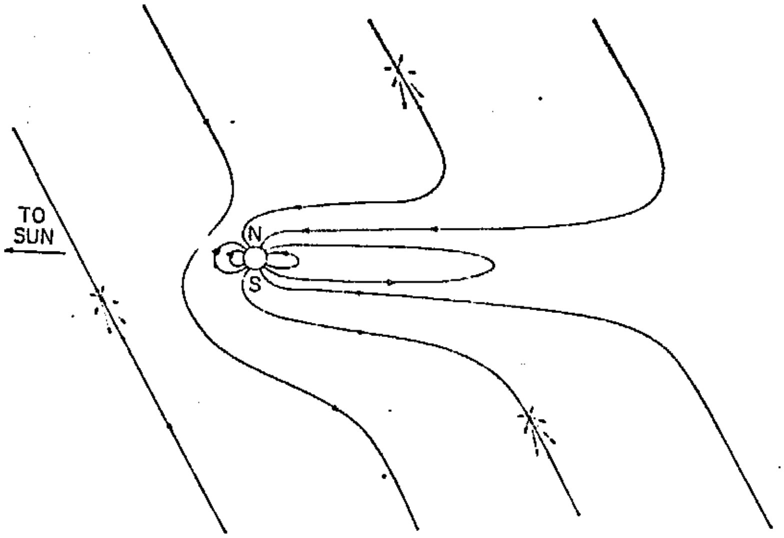

Figure 5-15

b.) at each value of t, the resultant velocity vectors $\vec{V}_r(\xi, \alpha)$ are calculated based on $\vec{B}$ and $\vec{V}_{sw}$.

c.) two constraints are then imposed to consider the particle countable.

1.) the angle between $\vec{V}_r(\xi, \alpha)$ and $\hat{D}$ is required to be less than some limiting angle, the value of which is the subject of the next subsection.

2.) the particle must have a source point on the shock surface.

5.7 Detector Look Cone

The detector look cone will be taken to mean the solid angle centered on the detector look direction $\hat{D}$ and having half angle δ . The nominal value of δ is ~3° as determined from the angular calibration of the instrument using a parallel ion beam in the lab. It must be kept in mind that when the detector is observing ions of large gyroradius compared to the dimensions of the entrance aperture of the instrument, the look cone of 3° half angle does not prevent the detector from seeing particles whose guiding center trajectories come from directions that are not in the field of view of the look cone. This is especially important in interpreting the data in this chapter since the gyroradii of bow shock protons are typically hundreds of kilometers and the guiding center trajectory does not represent the actual path of the particle. One would expect that if the SIDE could see particles only in the 6° look cone that the distributions shown in figures 5-3 through 5-8 would have sharp peaks about 6° wide. One would also expect that if the effective size of the look cone was say $\delta = 90°$, then when the detector was very near the shock it would always see particles since the angle subtended at the detector by the shock surface would be very large. The distributions are very broadly peaked indicating that the effective cone angle for observing bow shock protons is much larger than the nominal 6°, but that the half angle is not as large as 90°.

The influence of this effectively larger cone angle on the computer model is to relax the criterion that the resultant velocity vector lie within a 3° half angle of the detector look direction. It was determined from testing the computer model that a cone half angle of about 60° gave the best agreememt with the real data. For further discussion of the detector look cone and its relation to a particle's pitch angle see the discussion of the range of observable pitch angles later in this chapter.

5.8 Application of Computer model with idealized conditions.

The first application of the computer model was done using the Rice IBM 370 computer, using artificial input parameters, with the exception of those parameters relating to the lunar orbit. Explorer 35 data was not available at this time so typical values of the interplanetary field parameters and solar wind velocities were used to test the qualitative behavior of the model. The result, shown in figure 5-16, was generated using a solar wind velocity of 400 km/sec, a field latitude of 0° and a field longitude of 315°. Ninety pitch angles were tested at each energy and a spectrum was generated for every 40 minutes of lunar travel for the 5 day period shown.

Particles with energies of less than about 500 eV were not observed and only the highest three or so energy channels (3 to 3.5 keV/q) contained counts when the last spectrum was generated. The cutoff shoulder moved steadily toward higher energies with increasing time for each spectrum some particles were seen. The behavior of the model exhibited in figure 5-16 is roughly characteristic of what is actually observed during the post bow shock crossing regions one each lunation. The spectra from the real data just after bow shock crossing are generally peaked around 500 eV to 1250 eV and after 4 or 5 days only higher energy particles are seen if any at all. Figure 5-17 shows a typical post bow shock region for comparison.

It should be noted that in this highly idealized case, at least the gross features found in the real data are reproduced. The low energy peaks in the real data are due to

<u>Figure 5-16.</u> Synthetic data using typical interplanetary field conditions, namely $B_{lat}=0$ and $B_{long}=315°$. The 20 energy channels of the instrument are plotted on the horizontal scale representing 10 eV to 3500 eV; $\log_{10}$ of the average counts is plotted vertically and time runs up the oblique axis.

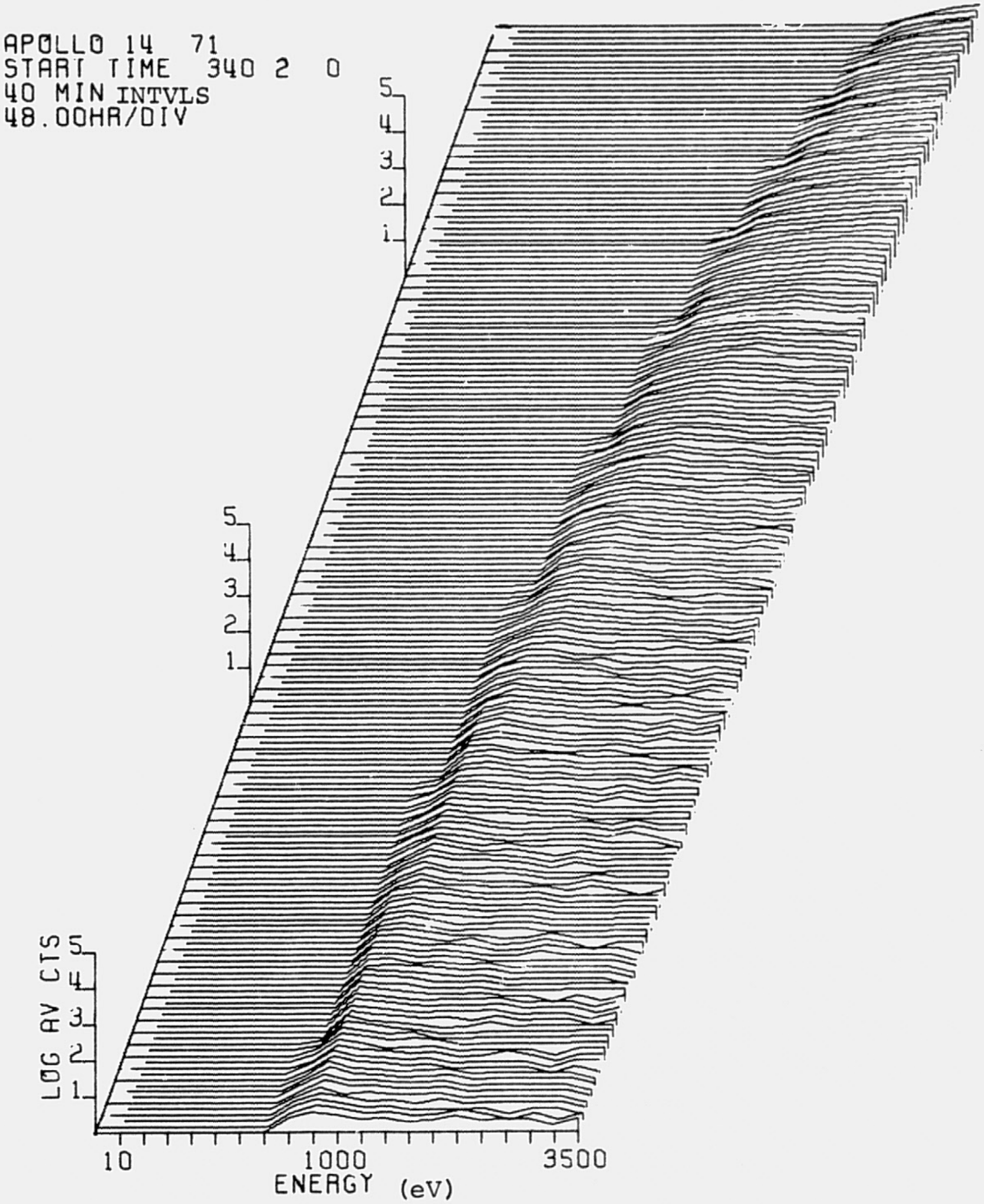
APOLLO 14 71
START TIME 340 2 0
40 MIN INTVLS
48.00HR/DIV
5
4
3
2
1
LOG AV CTS
10
1000
3500
ENERGY (eV)

Figure 5-16

Figure 5-17. Typical SIDE counting rate spectra from the dawn-side bow shock region.

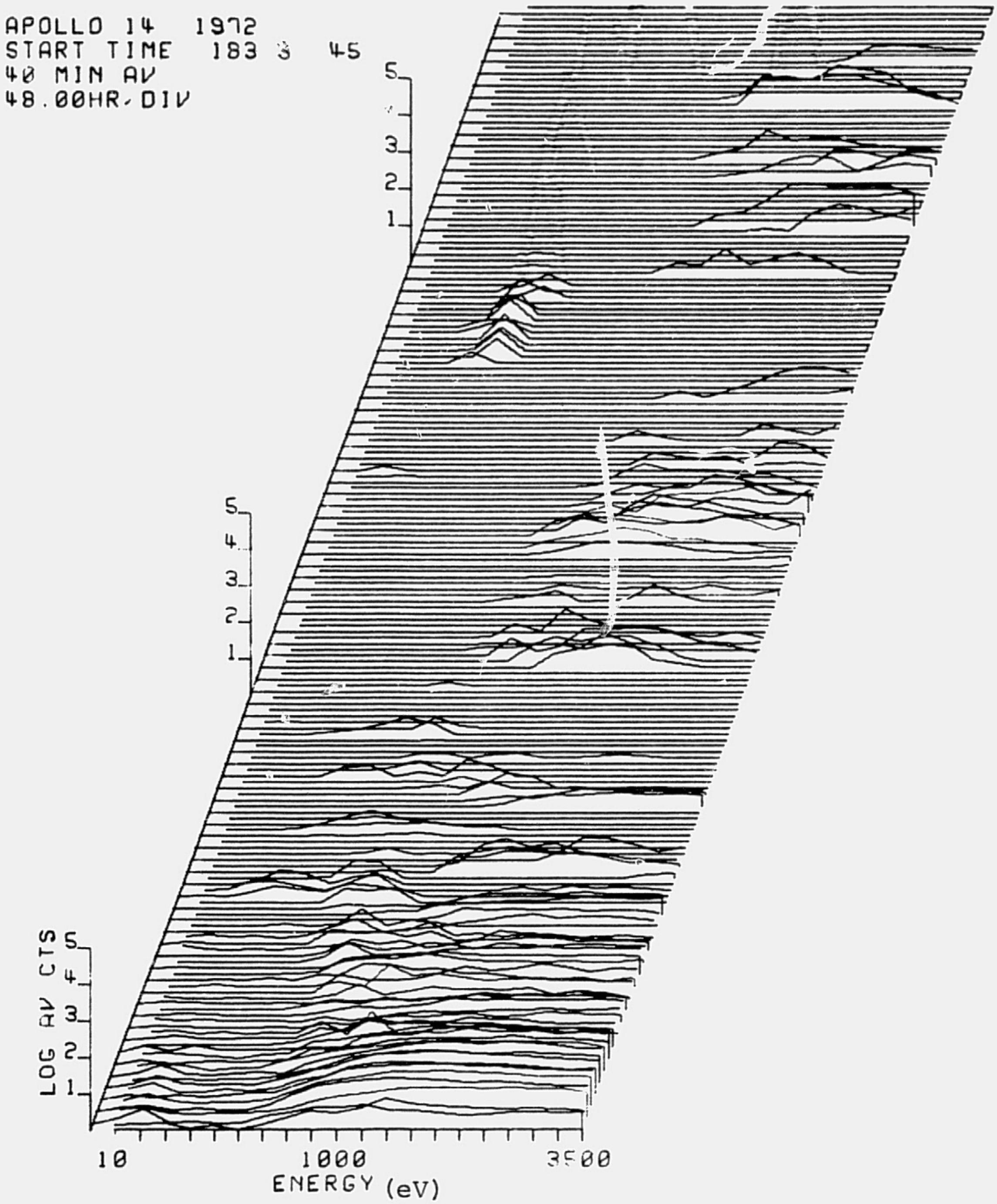
APOLLO 14 1972
START TIME 183 3 45
40 MIN AV
48.00HR/DIV
LOG AV CTS
1
2
3
4
5
10
1000
3500
ENERGY (eV)

Figure 5-17

lunar atmospheric ions.

The solar wind velocity and the interplanetary magnetic field are highly time varying quantities and only if this is taken into account in generating these spectra can one expect to effectively test the model of chapter 3 by generating synthetic data. A more elaborate procedure for generating synthetic data would be to calculate actual particle trajectories which may be done in future analyses of this problem.

5.9 Inclusion of interplanetary magnetic field data.

When Explorer 35 magnetometer data became available for the outbound region, discussed above, the computer model was refitted for the SDS 910. Ephemeris data tapes for Apollo 14, containing information on lunar position and detector look direction also became available so that it was no longer necessary to calculate the orbital parameters as described in chapter 4. The field information from the magnetometer and the position information from the ephemeris were synchronized and fed into the model and analyzed at 8 minute intervals using the scheme discussed above. The solar wind velocity was still taken to be 400 km/sec throughout.

The counting rate spectra from the computer model, at 8 minute intervals, for the outbound region are shown in figures 5-18 and 5-19. The gaps in time are due to the non-continuous data from the Explorer 35 magnetometer. It is

Figure 5-18. Synthetic data generated using the real values of the magnetic field parameters and the real ephemeris data as input to the program (see Appendix 3). Data gaps are due to the gaps in the Explorer 35 tapes.

Figure 5-19. Continuation in time of figure 5-18.

Figure 5-20. Real ion counting rate spectra for the time corresponding to that in figure 5-18. The high sharp peaks are transmission noise.

Figure 5-21. Continuation in time of figure 5-20.

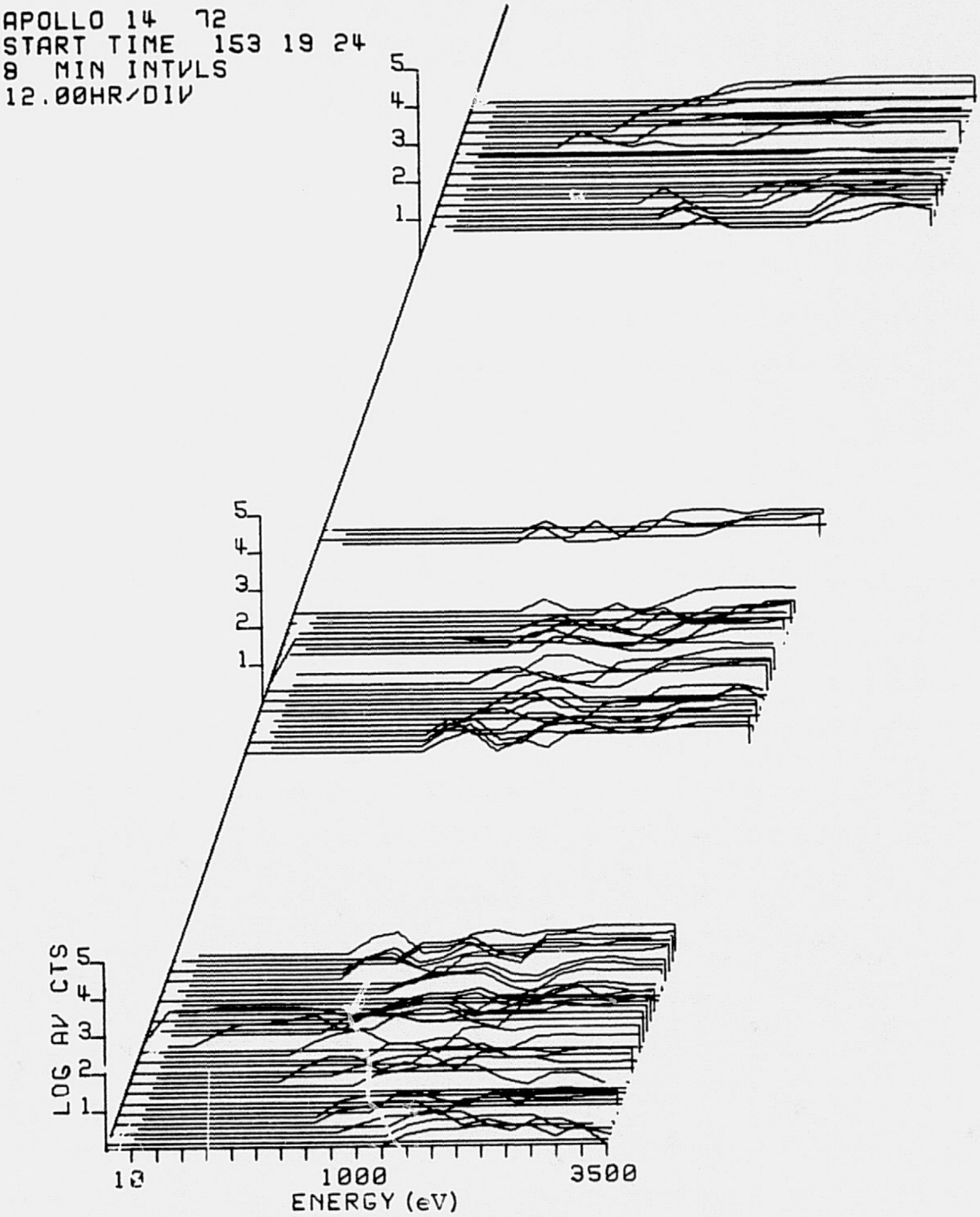
APOLLO 14 72
START TIME 153 19 24
8 MIN INTVLS
12.00HR/DIV
5
4
3
2
1
5
4
3
2
1
LOG AV CTS
5
4
3
2
1
10
1000
3500
ENERGY (eV)

Figure 5-18

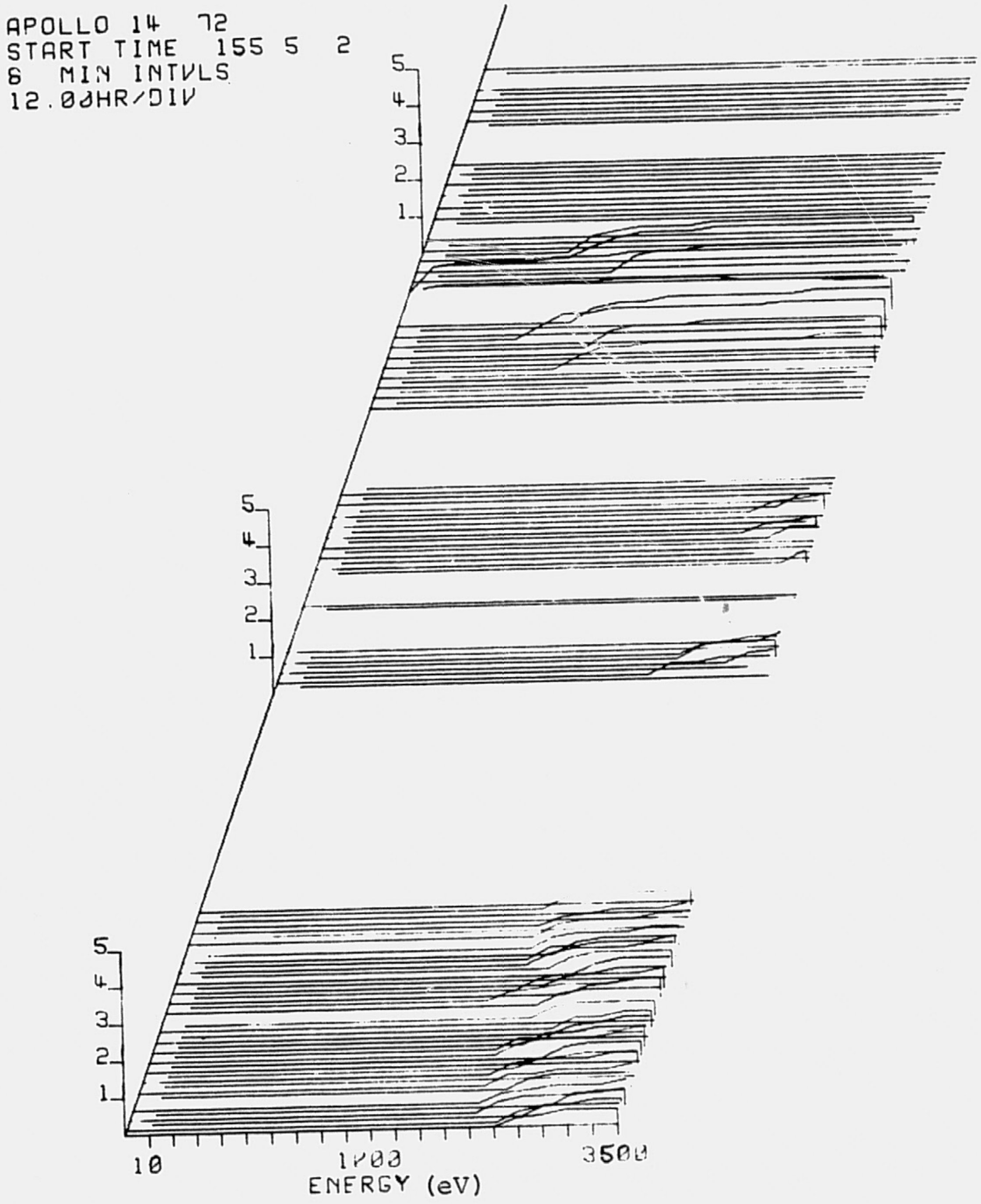
APOLLO 14 72
START TIME 155 5 2
6 MIN INTVLS
12.00HR/DIV
5
4
3
2
1
5
4
3
2
1
5
4
3
2
1
10
1000
3500
ENERGY (eV)

Figure 5-19

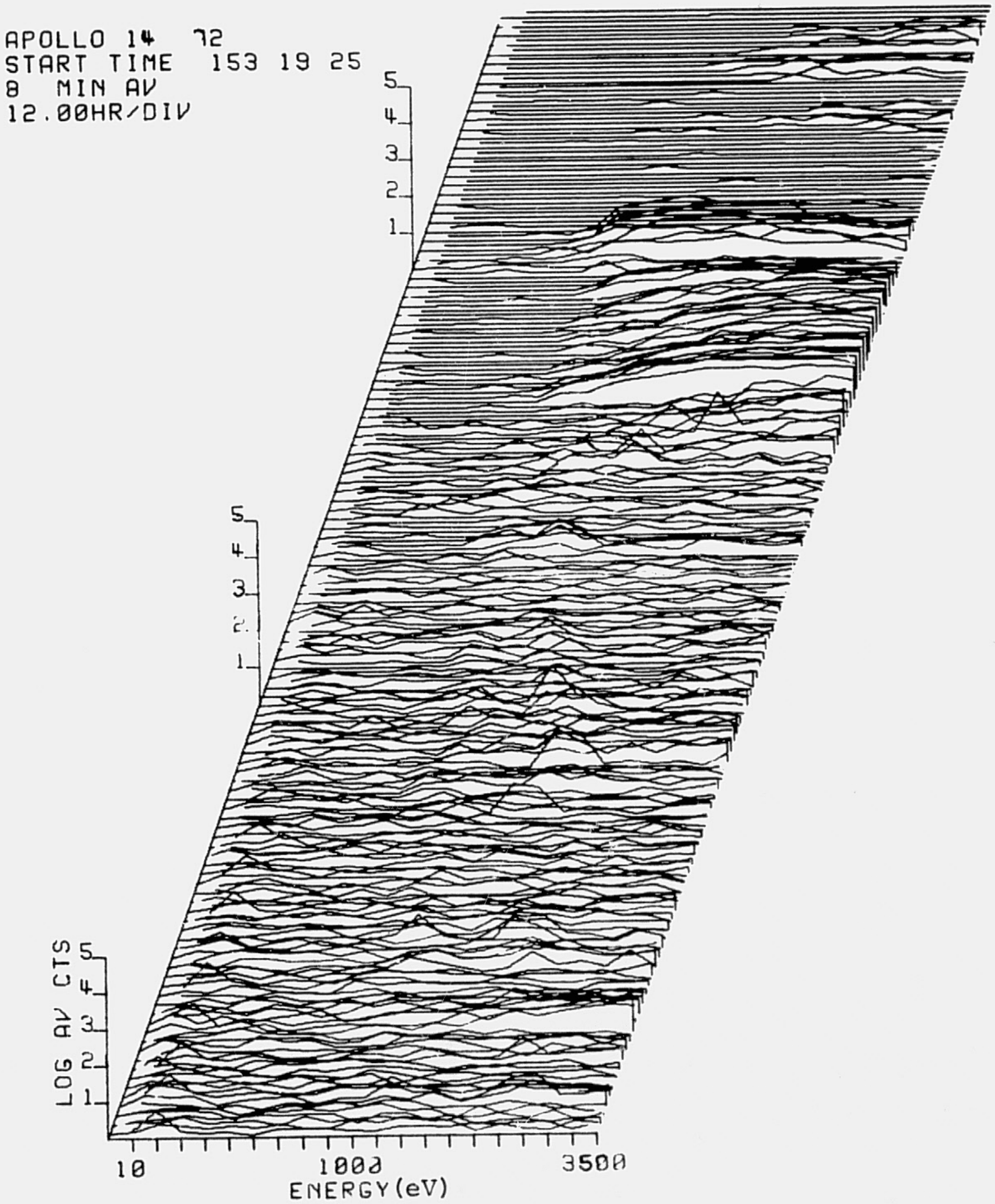
APOLLO 14 72
START TIME 153 19 25
8 MIN AV
12.00HR/DIV
LOG AV CTS
1
2
3
4
5
10
1000
3500
ENERGY(eV)

Figure 5-20


APOLLO 14 72
START TIME 155 3 13
8 MIN AV
12.00HR/DIV
5
4
3
2
1
5
4
3
2
1
LOG AV CTS
5
4
3
2
1
10
1000
3500
ENERGY (eV)

Figure 5-21

immediately obvious that the inclusion of the magnetic field data causes more structured synthetic counting rate spectra, but again it can be seen from examining these results that the observed particle energies are in the higher regions of the spectrum. That is, particles with energies less than about 500 eV are generally not observed. It is also interesting to note that the spectra are no longer always continuous in energy after reaching the cut-on energy; multiply peaked spectra are readily apparent. The results shown in figures 5-18 and 5-19 resemble real counting rate spectra much more closely than those of figure 5-16, even without including the changes in solar wind velocity.

The real counting rate spectra for the outbound region are shown in figure 5-20 and 5-21 for comparison. Although there are some obvious differences, the data generated by the computer model are not completely unlike the real data with both exhibiting structured spectra with counts mostly in the higher energy channels. The noisy spectra observed in the early post bow shock region of this lunation is not always present and could be due to some turbulent effect, seen only while the moon is close to the shock itself or possible temperature effects on the instrument are responsible for this noise. Unfortunately, event by event comparisons cannot readily be made due to the time gaps.

After generating the data shown in figures 5-18 and 5-19, an analysis, using the real data, was applied and this result is shown in figure 5-22. Due to the fact that the spectra were generated only every 8 minutes, the number of times a particular value of the field latitude was observed is considerably less than the number observed in the analysis of the real data and hence, the distribution of average integral counts is not as well defined. The results for the real data for the same period are shown in figure 5-23 for comparison.

It may seem circular to analyze the generated data under the philosophy for the first approach since the model was forced to operate in generating these data whereas in analyzing the real data, we were looking for evidence that the model was operating. It is, nevertheless, interesting to note that by forcing the model, a distribution is obtained that is very much like the actual distribution.

5.10 Range of observable pitch angles.

Due to the rather narrow field of view of the detector, (3° half angle), and the finite extent of the bow shock surface, some particles leaving the shock surface with large pitch angles may not be seen by the detector. It is possible to estimate the range of observable pitch angles at any given position in orbit by considering the simple geometry of fig-

Figure 5-22. Correlation in field latitude and counts using synthetic ion data as input.

Figure 5-23. Correlation of field latitude and counts for the same time period using real ion data.

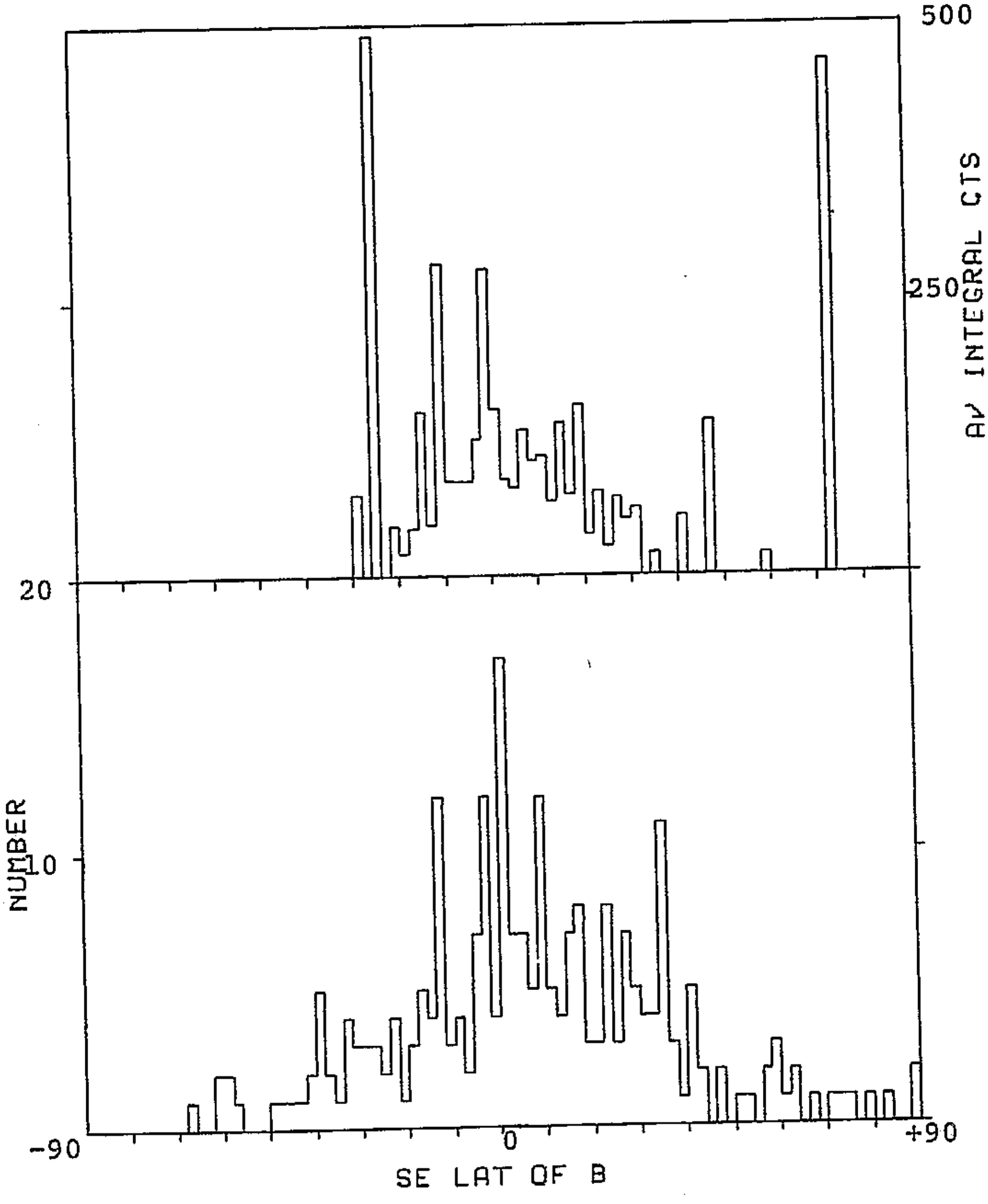

Figure 5-22

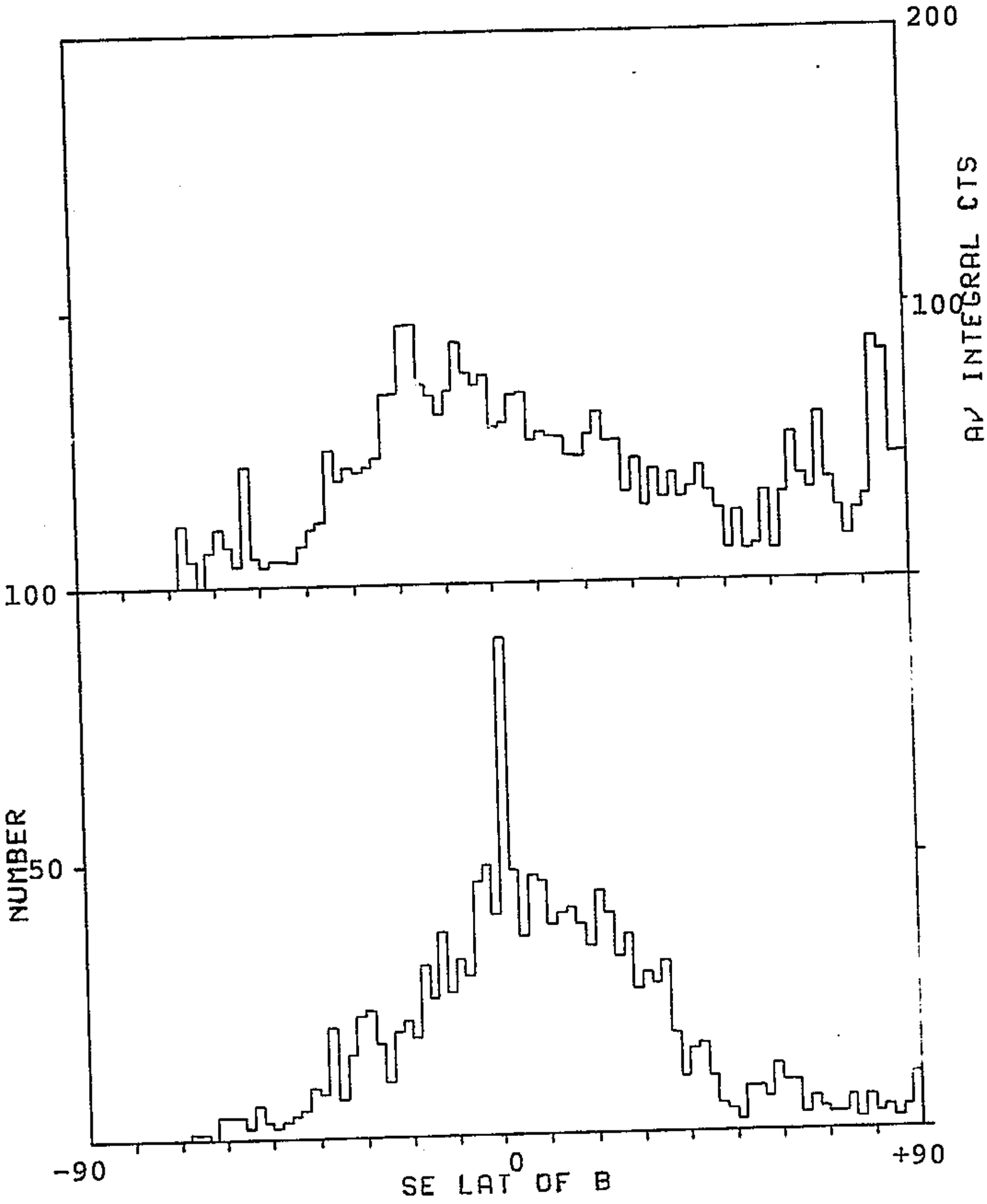

Figure 5-23

ure 5-24. The actual bow shock surface is approximated by a flat surface subtending approximately the same angle at the detector that the actual surface would subtend. The points L represent the limits of the source region, D represents the radius of a cross section of the bow shock in a dawn-dusk meridianal cut and R is the geocentric distance of the moon. δ is the half angle of the detector look cone, γ is the angle subtended at the moon by the bow shock and α 's represent pitch angles.

It can be seen from the figure that a particle leaving the shock at point C must have a pitch angle of δ or less to be detected by the instrument on the lunar surface. However, if the particle comes from the point L it must have a pitch angle in the range

$$\gamma - \delta < \alpha < \gamma + \delta$$

to be detected. Although each point on the surface defines such a range of pitch angles, the particles coming from the points L define the upper limit of the pitch angle range for a given distance from the shock. That is, particles with pitch angles

$$\alpha > \gamma + \delta$$

cannot get into the detector from any point on the shock at the distance defining γ.

Figure 5-24. Illustration of the relationship between the detector look cone angle, the angle subtended at the moon by the bow shock and the pitch angle of the particle. The figure shows the moon at last quarter in the dusk-dawn meridional plane. The dotted particle trajectory represents the upper limit to the pitch angle at this distance.

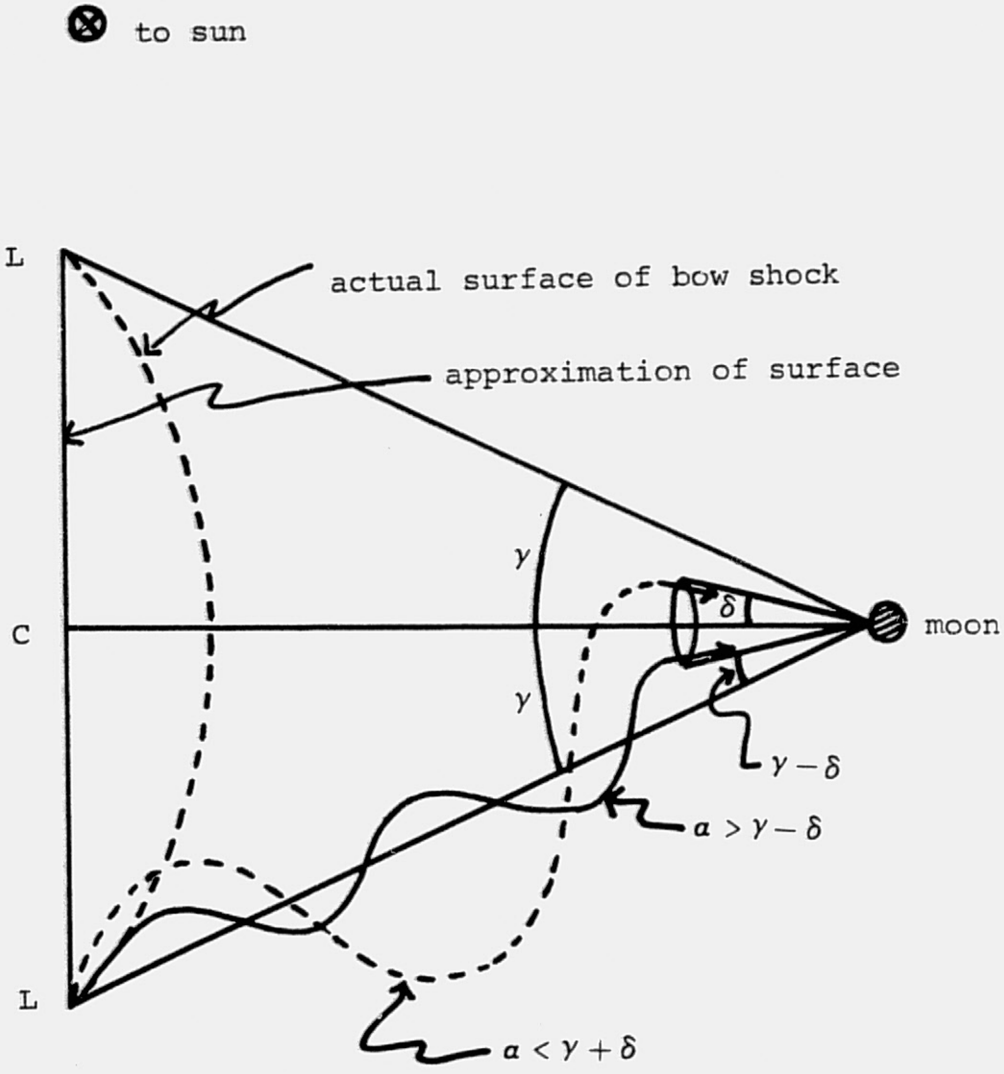

⊗ to sun
L
actual surface of bow shock
approximation of surface
γ
C
δ
moon
γ
$\gamma-\delta$
$a > \gamma - \delta$
L
$a < \gamma + \delta$

Figure 5-24

When the moon is very near the shock γ is very large and the particles of high pitch angle may be observed while as the moon moves away from the shock γ gets smaller, limiting the range of observable pitch angles. The limit of observable pitch angles for a case in which the α-range is fairly restricted can be estimated by calculating γ when the moon is on the dusk-dawn meridian. For this case,

$$D \sim 20\ R_e$$

$$R \sim 60\ R_e$$

$$\gamma = \tan^{-1}\left(\frac{20}{60}\right) = 20°$$

$$\alpha < 23°$$

This limit is probably one of the more restrictive due to the fact that as the moon moves further toward lunar nightime the detector sees a larger shock surface, thereby increasing γ and as mentioned above, γ is larger when the moon is nearer the shock surface.

The effect of this limited range of pitch angles was not considered in constructing the computer model, but the effect of this neglect should not be significant. Particles with high pitch angles have small $//$ velocities causing their resultant guiding center trajectories to be more in an anti-solar direction than ones with small pitch angles indicating that as one gets further away from the shock it becomes more difficult to see a high pitch angle particle based on considerations of guiding center trajectories alone. Not rejecting a particle in the model because of its high pitch angle does not significantly degrade the synthetic data since the particle would probably not be seen anyway because of its largely anti-solar guiding center trajectory.

The above considerations neglect the fact that the pitch angle is not constant with regard to the guiding center trajectory, but similar behavior of the pitch angle limits can be expected if this effect is taken into consideration.

5.11 Energy density of upstreaming protons

To estimate the effect of the upstreaming protons on the incident solar wind it is appropriate to calculate the energy density of the particles and compare this with the energy density of the incident solar wind protons.

By measuring the counterstreaming flux of the particles seen at the detector and assuming that each observed particle's energy is due to its linear motion into the detector, one obtains an energy density of

$$\eta_{B.S.} \sim 7 \times 10^{-13} \text{ ergs/cm}^3$$

for the 1 to 3.5 keV particles seen on a typical dawn side bow shock region. The incident solar wind energy density is of the order of 7 X 10^{-9} ergs/cm^3 which implies that

$$\eta_{B.S.} / \eta_{S.W.} \sim 10^{-4} \quad \text{(1 keV to 3.5 keV)}$$

One may conclude that the bow shock protons observed by SIDE would probably not cause a significant perturbation of the incident solar wind.

Other investigators have calculated energy density for the counterstreaming protons that are considerably higher than this value, however none of these other values are greater than about 1% of the incident solar wind energy density for quiet conditions. Lin and co-workers [1974] calculate a value of 10^{-12} ergs/cm^3 for protons in the range 29 to 100 keV. Evidence from their data indicates that there is a sharp cutoff in counterstreaming protons above 100 keV which implies that 100 keV is probably the upper limit in energy for bow shock protons. Asbridge et al. [1968] calculate an energy density of 10^{-11} ergs/cm^3 in the range of 3 to 6 keV which is 1% of the incident solar wind energy density. Scarf et al. [1970] have observed values of the counterstreaming energy density that are comparable to the incident solar wind energy density at times. However, it seems that large scale, long time perturbations of the incident solar wind by the counterstreaming protons is not a significant factor in determining the general behavior of these particles.

5.12 Conclusions.

The results of the analyses presented in this chapter give rise to the following conclusions:

a.) the observability of particles at the lunar surface, during the pre and post shock regions of the lunar orbit, is at least partially dependent on the configuration of the interplanetary magnetic field.

b.) the evidence from the analysis of the data and from the behavior of the model suggests that the model discussed in chapter 3 is probably operative in the pre and post shock regions of the lunar orbit and is responsible for the moderate to high energy particles observed in these regions. This result is not as well established in the pre shock region as in the post shock region and more data are needed to further analyze this region.

c.) The non-zero gyroradius of the particles cannot be ignored in the computer model but the effect it has on generating synthetic data can be approximated by enlarging the detector look cone angle to include a larger range of guiding center trajectories.

d.) the energy density of the counterstreaming protons is not sufficient to significantly perturb incident solar wind conditions.

Chapter 6

6.1 Discussion

There are possible sources other than the bow shock of moderate to higher energy protons, $\xi \geq 750$ eV, seen in the bow shock regions, viz.

- a.) lunar atmostpheric ions
  - 1.) interplanetary $\vec{E}$ field ions
  - 2.) surface $\vec{E}$ field ions
- b.) solar wind ions and suprathermal solar wind ions
- c.) cosmic rays
- d.) unknown sources such as lunar bow shock protons

The "bow shock region" will refer to the regions of the lunar orbit extending from shock crossing to about a day or so past the sunset terminator on the dawn side and the analogous region before shock crossing on the dusk side of the magnetosphere.

The reasons that it is unlikely that these sources can account for the observations completely will be pointed out below.

a.) lunar atmospheric ions-As discussed by Lindeman [1973] and Manka [1972], ions from the lunar atmosphere can be accelerated into the detector by the interplanetary electric field $\vec{E}_{IP}$ when the field lies in the ecliptic plane. By considerations of surface density and temperature, ion scale height, ionization rate, and strength of the electric field, the expected energy spectrum observed by the SIDE is given by,

$$F(\xi) = \frac{p\,n_o}{e\,E} \exp\left[-\xi/eEH\right] \qquad 6\text{-}1$$

where,

n_o=surface number density

p=ionization rate

e=charge on the ion

H=scale height

$E = \left|\vec{E}_{IP}\right|$

ξ =ion energy

Using appropriate values of these parameters for the Apollo 15 event observed on day 312, 1971 Lindeman [1973] has determined the predicted flux values and compared them to the observed fluxes. The result is shown in figure 6-1 (after Lindeman [1973]). The flux drops off rapidly after about 250 eV indicating that the higher energy ions observed in this same region are not lunar atmospheric ions which have been accelerated by the interplanetary electric field. It should also be pointed out that the distribution obtained in figure 5-5 indicates that most of the particles were observed when the interplanetary electric field was not in the ecliptic plane in contrast to the results obtained by Lindeman [1973],(figure 6-2), and Manka [1972],(figure 6-3), that lunar atmospheric ions are seen when $\vec{E}_{IP}$ is in the

Figure 6-1. Predicted and observed energy spectra of lunar atmospheric ions. Note the sharp drop in energy after about 250 eV. [after Lindeman (1973)].

Figure 6-2. Integral flux vs. angle out of the ecliptic plane of the interplanetary $\vec{E}$ field. The integral flux drops smoothly as the field goes out of the ecliptic. The bottom part of the graph displays $\xi / |\vec{E}|$ vs. angle out of the ecliptic plane. [Lindeman, 1973]

Figure 6-3. Correlation in integral flux and B_x. $B_x \sim 0$ implies an $\vec{E}$ field that is about in the ecliptic plane and pointing into the detector. [Manka (1972)]

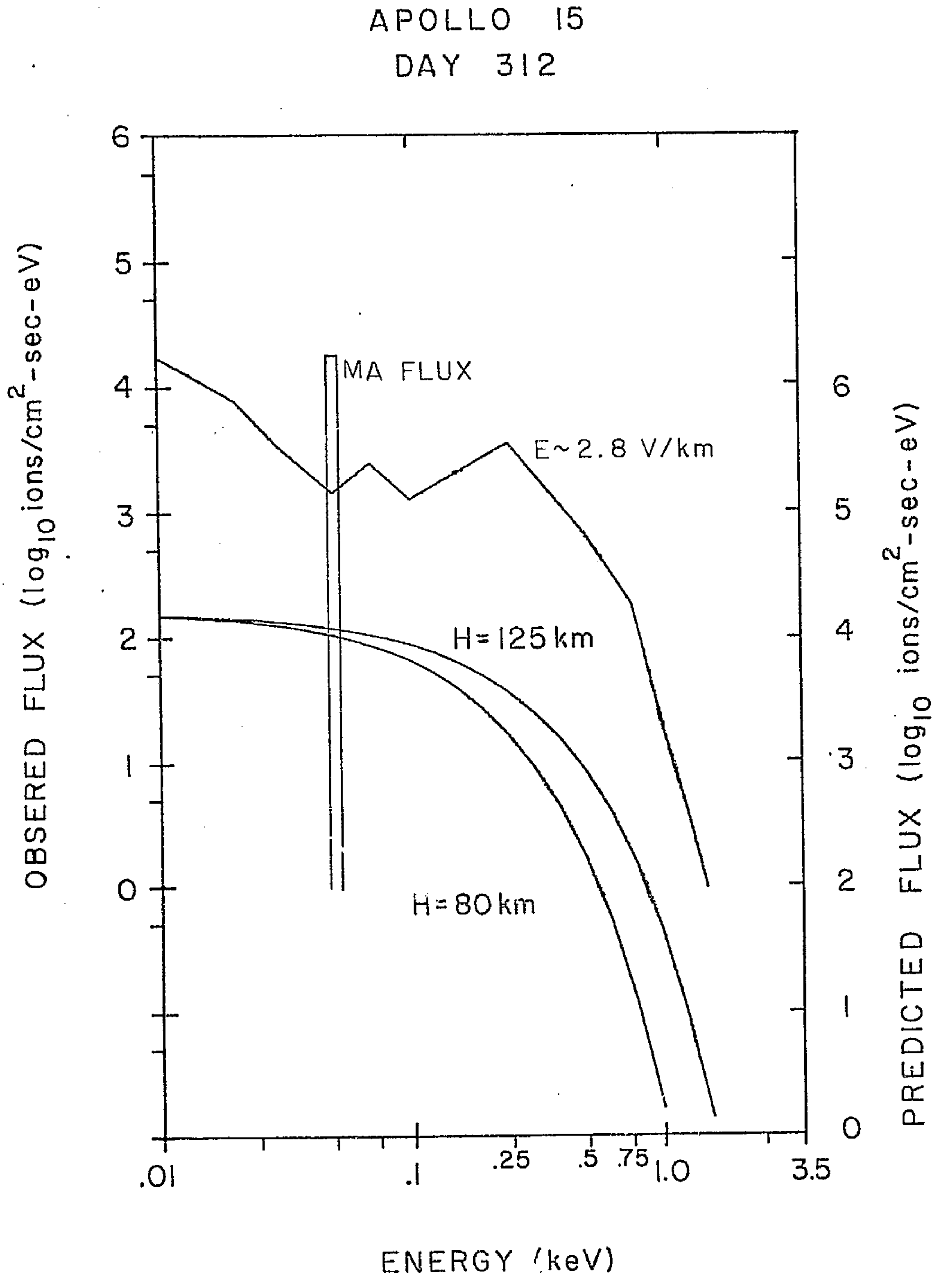
APOLLO 15
DAY 312
OBSERED FLUX ($\log_{10}$ ions/cm^2-sec-eV)
PREDICTED FLUX ($\log_{10}$ ions/cm^2-sec-eV)
ENERGY (keV)
MA FLUX
E~2.8 V/km
H=125 km
H=80 km
6
5
4
3
2
1
0
6
5
4
3
2
1
0
.01
.1
.25
.5
.75
1.0
3.5

Figure 6-1

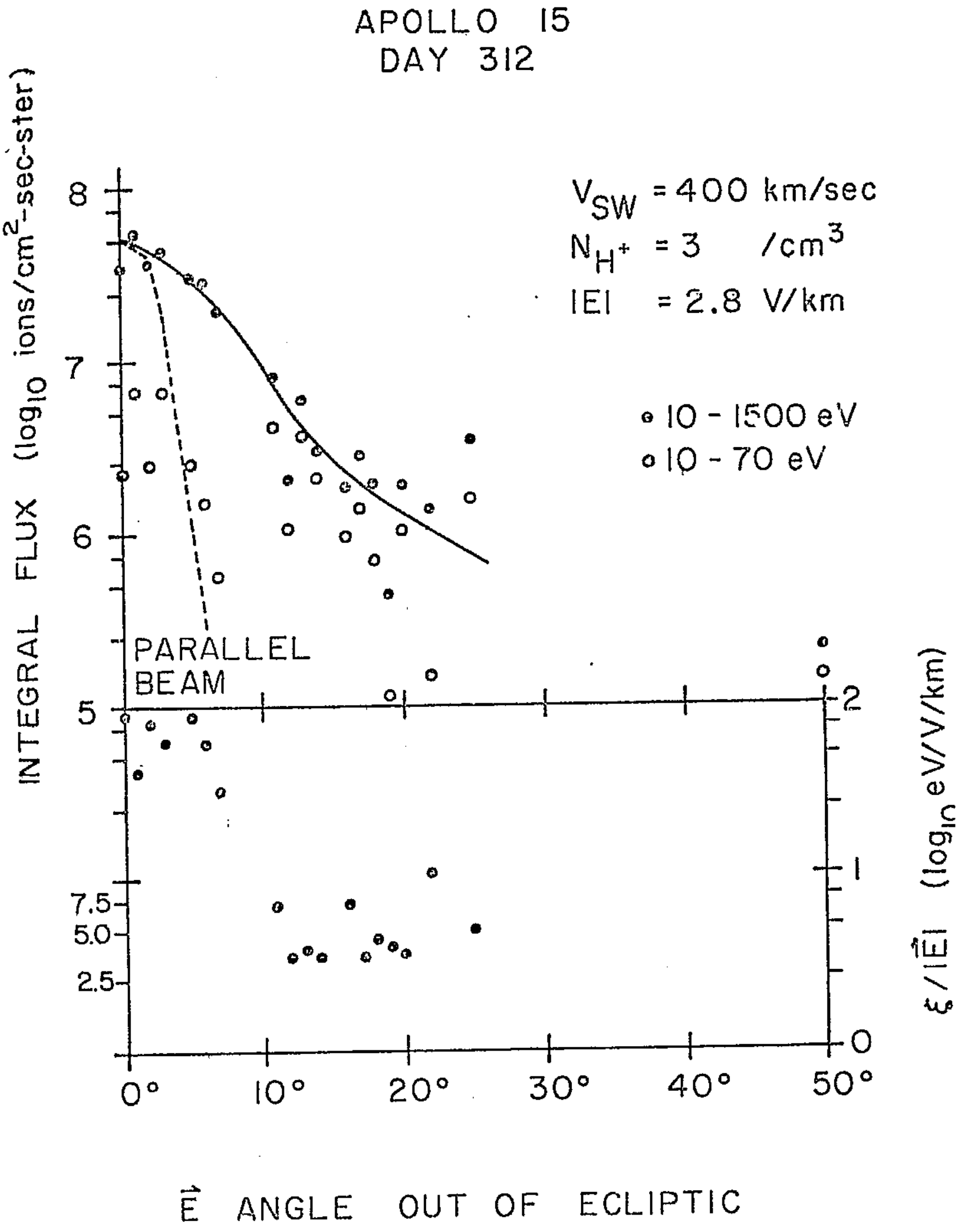
APOLLO 15
DAY 312
INTEGRAL FLUX ($\log_{10}$ ions/cm^2-sec-ster)
8
7
6
5
7.5
5.0
2.5
V_{SW} = 400 km/sec
N_{H^+} = 3 /cm^3
$|E|$ = 2.8 V/km
10 - 1500 eV
10 - 70 eV
PARALLEL BEAM
2
1
0
$\mathcal{E}/|E|$ ($\log_{10}$ eV/V/km)
0°
10°
20°
30°
40°
50°
$\vec{E}$ ANGLE OUT OF ECLIPTIC

Figure 6-2

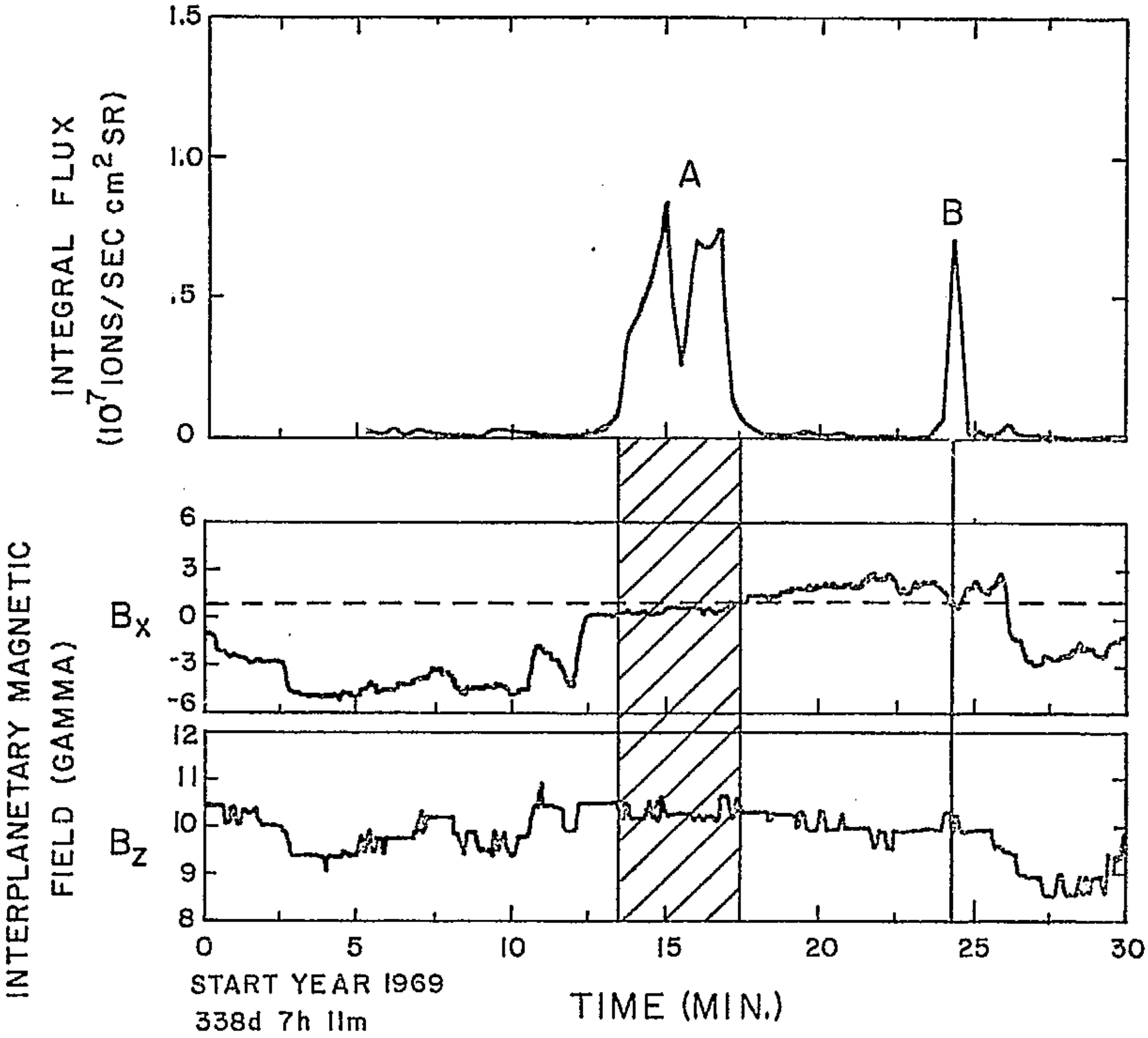

INTEGRAL FLUX
(10^7 IONS/SEC cm^2 SR)
1.5
1.0
.5
0
A
B
INTERPLANETARY MAGNETIC
FIELD (GAMMA)
B_X
6
3
0
-3
-6
B_Z
12
11
10
9
8
0
5
10
15
20
25
30
START YEAR 1969
338d 7h 11m
TIME (MIN.)

Figure 6-3

ecliptic plane.

Indications are that at the terminator the largest value of an attractive lunar surface potential is on the order of -100 V [Fenner et al., 1973], which implies that essentially thermal atmospheric ions could not attain energies much greater than about 100 eV before being detected by the SIDE. The lunar surface potential is obviously not responsible for the particles of energy greater than about 100 eV. It is difficult to imagine any other local electric fields of sufficient strength to accelerate atmospheric ions to the observed energies.

b.) solar wind ions-The thermal energy of a solar wind proton is on the order of 10 ev and its energy due to bulk flow motion, ($V \sim 400$ km/sec), is ≥ 1000 eV. The angle between the look direction of the detector and the solar wind flow in the bow shock region eventually becomes $>90°$, yet the high energy flows are still observed.

Although local lunar surface magnetic fields as high as 300 gammas have been measured, Dyal et al. [1972], these fields are not of sufficient strength to deviated solar wind particles into the detector. In addition, there is still no known acceleration mechanism that could produce the 3500 eV particles that are observed. There is no reason to suspect that the spectrum ends abruptly at 3500 eV as well. Counter-streaming protons of energy 3 to 6 keV have been observed in this region of space by other investigators, viz. Asbridge et al. [1968]. Lin et al., [1974] have observed counter-streaming protons in the energy range 30 to 100 keV. Although solar wind protons in the energy range $5 \leq \xi \leq 50$ keV known as suprathermal solar wind protons have been observed [Frank, 1970], these energetic proton events are not characteristic of the quiet solar wind. Since these suprathermal protons come from the solar direction one would again have to invoke some mechanism to deviate the particles into the detector.

c.) cosmic rays-Very high energy protons ($\xi \geq$ 50 MeV) can penetrate the case of the SIDE instrument and activate the channeltron causing counts to appear in whatever energy channel is being sampled at the time. The cosmic ray flux in the interplanetary medium is responsible for part of the background noise during instrument daytime and is responsible for most of the background during instrument nightime. These counts in random channels are generally very low (1 or 2), and are only enhanced during unusual solar proton events such as solar flares as discussed by Medrano [1973]. That is, cosmic ray protons produce a random background of very low intensity in quiet times and ir disturbed times the background counts rise independent of energy channel making their identification easy.

d.) other sources-At the time of this writing no lunar bow shock capable of producing 3 keV protons has been observed. Other complicated solar wind-lunar interactions may occur to produce these particles, but such processes have not been reported.

The above considerations alone indicate strongly that the high energy particles observed in this region are indeed protons from the bow shock since it is the most likely other source. Other corroborating evidence that the high energy particles are from the bow shock can be summarized as follows.

a.) Protons of the same energies as the observed ones have been previously observed in this region by several investigators so it is not unreasonable to expect that the SIDE would detect them. The instrument looks back at the shock in this region of the orbit.

b.) Results of the data analysis of this thesis indicate that these high energy particles are influenced by the interplanetary magnetic field in such a way as to be consistent with the proposed $\vec{E}X\vec{B}$ drift model.

It is apparent that bow shock particles are a dominant feature of the data observed in the bow shock regions which suggests a reclassification of the recurring ion events discussed by Lindeman [1971,1973]. Lindeman classified the ion spectra in the extra-magnetospheric regions of the lunar orbit into five basic types, two of which are clearly identifiable with bow shock protons. The Type I spectrum has a single peak from 2000 eV to 3500 eV and Type II has a double peak, the first peak from 30 eV to 250 eV and the second from 2000 eV to 3500 eV, (see figure 6-4). Subsequent investigation by Lindeman [1973], has shown that the low energy events in the bow shock region can be classified into three types.

a.) $\vec{V}X\vec{B}$ events 10 eV to 500 eV

b.) Lunar surface potenial (LSP) events 10 eV to 100 eV

c.) Instrument resonance events (IRE's) $\lesssim 50$ eV

In light of these findings, the low energy peak of the Type II event is easily identified as being due to LSP and $\vec{V}X\vec{B}$ events near the terminator with the high energy peak being explained by the presence of bow shock protons in this region. The Type II event is merely a Type I event with the contribution to the spectrum of the LSP and $\vec{V}X\vec{B}$ events.

The ion data observed in the bow shock region can therefore be classified as consisting of four basic types of events; a.,b.and c. above and

d.) Bow shock proton (BSP) events $\xi \geqq 750$ eV

Based on the present research it is possible then to state a general criterion for identifying BSP events in the data. During passage of the moon through the bow shock region, any observed particles having energy greater than or about equal

Figure 6-4. Recurring ion events Types I and II. Type I has only a high energy peak while Type II has a low energy peak in addition to the high energy peak. [redrawn after Lindeman (1971)]

C.3

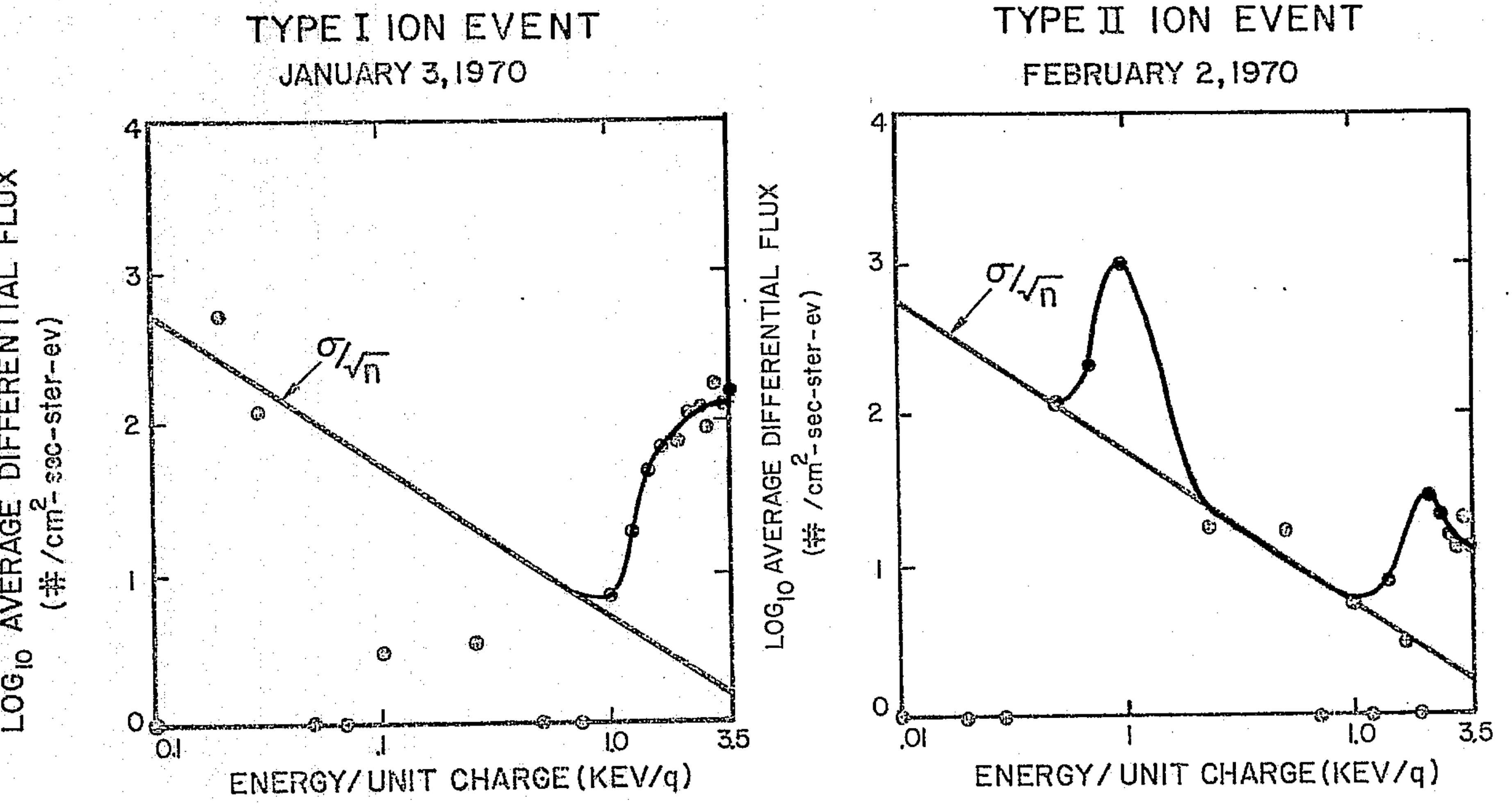
TYPE I ION EVENT
JANUARY 3, 1970

TYPE II ION EVENT
FEBRUARY 2, 1970

Figure 6-4

to 750 eV are probably bow shock protons, with the exception of clearly identifiable high energy events associated with unusual activity in the interplanetary medium.

Figure 6-5 shows representative counting rate spectra in the bow shock region near the sunset terminator with two of the above types of events easily identifiable. LSP's and BSP's are readily apparent and a tentative identification of $\vec{V} \times \vec{B}$ events can be made. The marginality in the identification of the $\vec{V} \times \vec{B}$ events could be easily removed by looking at the interplanetary field behavior for this period and remembering that $\vec{B}$ out of the ecliptic implies $\vec{V} \times \vec{B}$ events and $\vec{B}$ in the ecliptic implies BSP events.

Figure 6-5. Representative part of the bow shock region showing varied ion spectra near the sunset terminator.

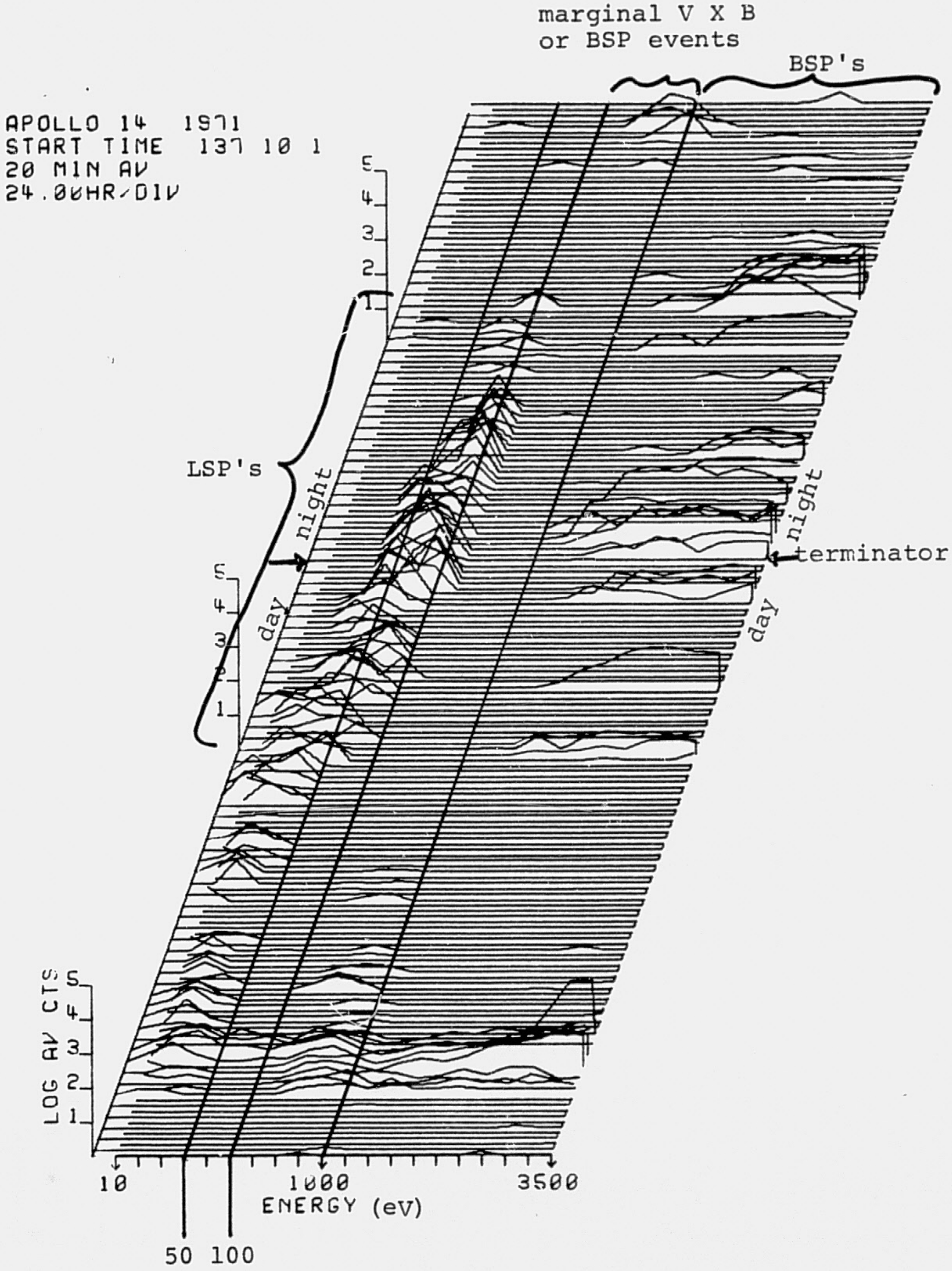
marginal V X B
or BSP events
BSP's
APOLLO 14 1971
START TIME 137 10 1
20 MIN AV
24.00HR/DIV
5
4
3
2
1
LSP's
night
day
5
4
3
2
1
night
terminator
day
LOG AV CTS
5
4
3
2
1
10
1000
3500
ENERGY (eV)
50 100

Figure 6-5

6.2 Further Research

Limitations on the accuracy of the present analysis are due primarily to a lack of sufficient simultaneous magnetic field and ion data. An analysis of the bow shock regions carried out over several lunations would much enhance the significance of the results and would likely improve the agreement of the data with what is expected from the model. This can be seen by noting the better correlation achieved in the outbound region, (see figure 5-5), where three days of data were analyzed as opposed to two days on the inbound side. The amount of simultaneous particle and field data available in any one lunation is also limited by the data gaps in the field data incurred while Explorer 35 is behind the moon. The lack of an onboard recorder causes data gaps of about 5 hours on each orbit of the satellite.

Other problems exist such as the unknown spatial distribution of the field, an important factor in determining the resultant guiding center trajectory of a particle. Not much can be done about this problem but it appears that the variation of the field over a distance comparable to the proton gyroradius is not significant since particles do seem to make it to the moon via the $\vec{E}X\vec{B}$ mechanism. Likewise the problem of including the effects of the local surface fields is very difficult in that the spatial configuration and extent is not well known, but again these fields do not seem to play a significant role from the self consistent point of view. That is, if one assumes a model and observes the behavior predicted by the model then other influences must not be too significant.

In some instances the field is also highly time varying and no account of this has been taken in the present analysis. If the field is varying rapidly with respect to a characteristic time of the motion, say the gyroperiod, (~ 12 sec), the guiding center treatment breaks down. There were several instances in the data where the field was stable with respect to a gyroperiod but the inclusion of times where the field was varying rapidly would detract from the accuracy of the results. An obvious way to improve the results would be to confine the analysis to times of stable field conditions.

As noted above, the bow shock regions are of a highly diverse character in ion spectra with bow shock protons contributing a large portion of the observed ions but certainly not all of them. This would imply that any correlation of particles observed with field configuration would be further obscured by including particles whose observability did not depend on the field configuration. All events were included in this analysis. Obviously, the contribution by the LSP's, the IRE's and any other event associated with the lunar atmosphere would be detrimental to the results. This point can be clearly seen by noting the effect of including all of the ion events on the distributions shown in figures 5-5 and 5-3. In particular, the inclusion of the $\vec{V}X\vec{B}$ events inflates the upper end of the distribution in the outbound region and the lower end of the distribution in the inbound region. For this particular type of event the contributions to the distributions cannot really be considered detrimental since $\vec{V}X\vec{B}$ events do depend on the field configuration and are easily distinguishable from BSP events.

Again by considering isolated events where the field is stable and where particles from other known sources can be removed from the analysis, e.g. near the terminator, the correlation would be greatly improved.

With the availability of good data from all three SIDE's and Explorer 35, the directional nature of the proposed model could be more effectively tested. The wide variation in longitude of the look direction of the three detectors would allow a cross correlation in dependence on longitude of the observability of ions. The use of three instruments in this manner could also be helpful in determining the effective size of the look cone as discussed in chapter 5.

Any investigation such as the one done for this thesis yields many new and interesting areas for further work. Two of the related areas of special interest are, the possible acceleration mechanisms associated with the bow shock itself and a study of the nature of the source points on the shock surface. If a very good fit to the real data can be achieved using a particular type of source function, then one is led to suspect that that source function probably approximates the real one. Knowing the source function at the shock surface could be useful in determining which if any of various models for the acceleration mechanism is correct. Two of the major models for the acceleration mechanism are reviewed in the Appendices. Specular reflection at the shock and subsequent energization by the interplanetary electric field has been proposed by Sonnerup [1969] and the mechanism of Fermi acceleration has been developed by Jokipii [1966].

However, the primary mission of the SIDE is to gather data that can be used to learn about the lunar atmosphere which suggests that the real value of this research and any further research in this area is that it aids in understanding the complicated spectrum of events occurring in the bow shock regions of the lunar orbit. These bow shock regions are the most fertile in the data for providing information on the lunar atmosphere and certainly warrant further investigation.

Chapter 7

7.1 Summary

The basic objectives of the research done for this thesis were outlined in chapter 1 and will be briefly restated here.

a.) to determine if the particles of energy $\gtrsim 750$ eV observed in the pre and post bow shock regions are indeed bow shock particles.

b.) to establish a criterion for the identification of these particles.

c.) to propose and develop a physical model to explain the presence of the bow shock protons if they are found in the data.

Such a model based on $\vec{E}X\vec{B}$ drift trajectories was developed in chapter 3 leading to the following basic conclusions about the behavior of bow shock protons in this region.

a.) the observability of bow shock particles at the moon by this mechanism is highly dependent on the configuration of the interplanetary magnetic field.

b.) there is an inherent dusk-dawn asymmetry in the model that should be observable in the data.

It was also pointed out that the present model, although similar to that proposed by Asbridge et al. [1968], is a more realistic one in that it describes all particles leaving the shock, not just those with a special velocity and pitch angle.

The details of the computer model and its connection to the physical model were discussed in chapter 4 where criteria for the observability of bow shock particles at the moon were established. For a particle to be observed at the moon by the $\vec{E}X\vec{B}$ mechanism, it must,

a.) come from the right direction and

b.) have a source point on the shock surface.

The plausibility of the physical model of chapter 3 was established by the data analysis, the results of which are displayed in chapter 5. The major conclusions drawn from interpretation of the data are,

a.) analysis, independent of the model, shows that the data behave as one would expect from the model.

b.) synthetic data generated by the computer model agree semi-quantitatively with the observed data.

c.) behavior of the computer model coupled with considerations of actual particle trajectories indicates that the effective size of the look cone of the detector is substantially larger than the nominal value when applied to bow shock protons.

Arguments against other possible sources for the observed ions of energy ≥ 750 eV are presented in chapter 6. These other sources are,

a.) lunar atmospheric ions

b.) solar wind ions

c.) cosmic rays

d.) lunar bow shock or other unknown sources

and were rejected primarily on energy considerations. Lunar atmospheric ions and solar wind ions have much lower energies in general than the observed moderate to high energy ions and it was pointed out that no known acceleration mechanism at the moon is capable of producing particles of the observed energies. Cosmic rays were dismissed based on the well established character of penetrating particle events which are unlike bow shock proton spectra.

The value of isolating and identifying bow shock protons in the data was also discussed in chapter 6 where it was noted that the usefulness of the bow shock region for studying the lunar atmosphere can be enhanced by separating BSP events from the lunar atmosphere events. A general criterion for identifying bow shock protons was given; particles of energy greater than or about equal to 750 eV and found in the pre and post bow shock crossing are probably associated with the bow shock.

7.2 Conclusions

a.) The protons observed in the bow shock regions with energies $\geq$ 750 ev are from the bow shock and can readily be identified in the data.

b.) The proposed $\vec{E}X\vec{B}$ drift model is a viable one as long as its limitations are kept in mind.

Appendix 1

A1.1 Define an orthogonal coordinate system S and an orthogonal coordinate system S' that has the same origin as S but is oriented arbitrarily with respect to S otherwise. It is possible to make the axes of system S coincident with system S' by three sucessive counterclockwise rotations of the S axes. The angles through which one must rotate to perform such a "transformation" of the coordinate axes are known as Euler angles. The angles ϕ, ψ, and θ of figure A1.1 are the Euler angles for the transformation from system S to S' and the transformation matrix and its inverse are shown on the next page.

A1.2 Notes concerning chapter 4.

In transforming from system S'' to S_{se} the matrix of transformation was ($\underline{SBA}$) and the position of the moon in the SE system was found to be

$$\vec{r}_{se} = \underline{SBA}\,\vec{r}'' \qquad \text{A1.3}$$

The vector $\vec{r}''$ has only an x-component in system S'' since the moon is on the x''-axis at a distance r from the origin. That is,

$$\vec{r}'' = r\,\hat{x}'' \qquad \text{A1.4}$$

or represented as a column matrix,

$$r'' = \begin{pmatrix} r \\ 0 \\ 0 \end{pmatrix}$$

$$\underline{A} = \begin{pmatrix} \cos\psi\cos\phi - \cos\theta\sin\phi\sin\psi & \cos\psi\sin\phi + \cos\theta\cos\phi\sin\psi & \sin\psi\sin\theta \\ -\sin\psi\cos\phi - \cos\theta\sin\phi\cos\psi & -\sin\psi\sin\phi + \cos\theta\cos\phi\cos\psi & \cos\psi\sin\theta \\ \sin\theta\sin\phi & -\sin\theta\cos\phi & \cos\theta \end{pmatrix} \quad \text{A1.1}$$

$$\underline{A}^{-1} = \begin{pmatrix} \cos\psi\cos\phi - \cos\theta\sin\phi\sin\psi & -\sin\psi\cos\phi - \cos\theta\sin\phi\cos\psi & \sin\theta\sin\phi \\ \cos\psi\sin\phi + \cos\theta\cos\phi\sin\psi & -\sin\psi\sin\phi + \cos\theta\cos\phi\cos\psi & -\sin\theta\cos\phi \\ \sin\theta\sin\phi & \sin\theta\cos\phi & \cos\theta \end{pmatrix} \quad \text{A1.2}$$

<u>Figure A1.1</u> Euler angles θ , ψ and ϕ . The coordinate transformations between the primed and the unprimed systems can be conveniently expressed in terms of the Euler angles. (Goldstein, 1950)

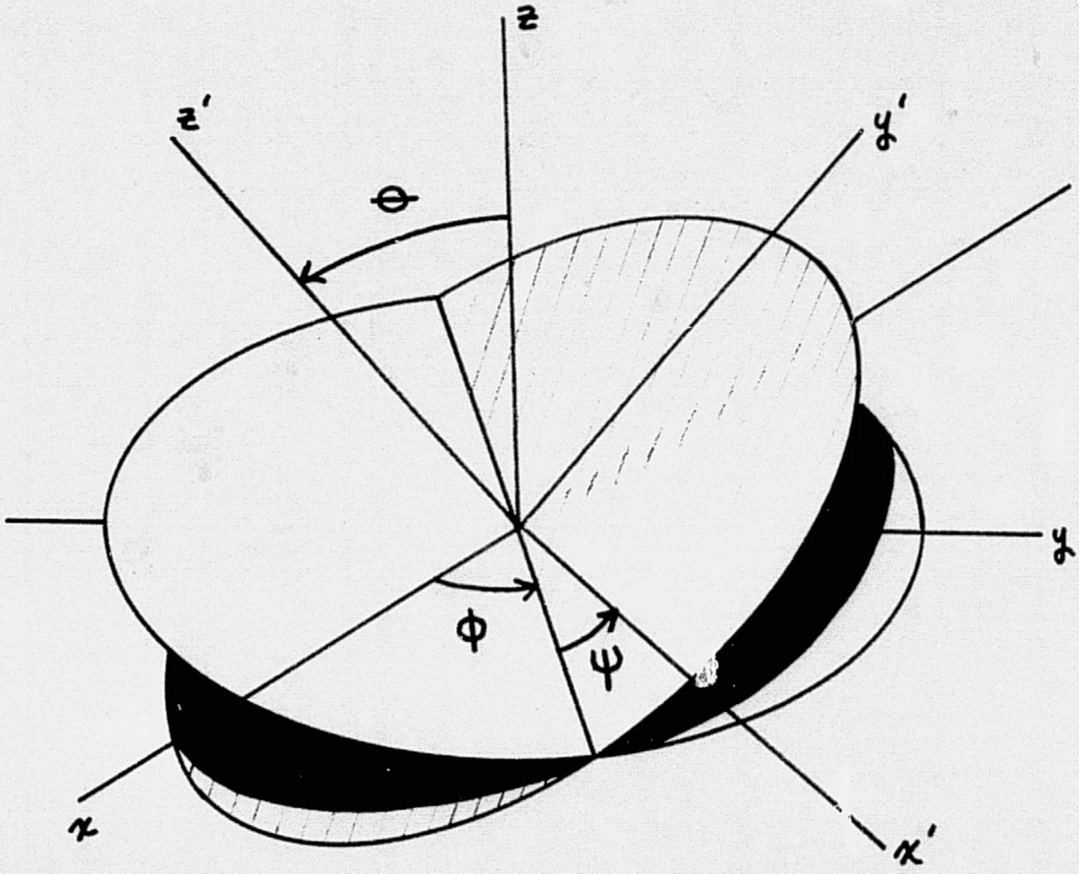

Figure A1.1

Figure A1.1

This column matrix, when multiplied by (SBA) from the left gives

$$\begin{pmatrix} r_{sex} \\ r_{sey} \\ r_{sez} \end{pmatrix} = \begin{pmatrix} SBA_{xx} & SBA_{xy} & SBA_{xz} \\ SBA_{yx} & SBA_{yy} & SBA_{yz} \\ SBA_{zx} & SBA_{zy} & SBA_{zz} \end{pmatrix} \begin{pmatrix} r \\ 0 \\ 0 \end{pmatrix} \qquad \text{A1.6}$$

$$\begin{pmatrix} r_{sex} \\ r_{sey} \\ r_{sez} \end{pmatrix} = r \begin{pmatrix} SBA_{xx} \\ SBA_{yx} \\ SBA_{zx} \end{pmatrix} \qquad \text{A1.7}$$

Hence equations 4-8.

Appendix 2

Derivation of equations 3-2 through 3-9.

Consider a charged particle moving in a region in which there exists electric and magnetic fields. The force on the particle due to the electric field is,

$$\vec{F}_e = q\,\vec{E} \qquad \text{A2.1}$$

and the force due to the magnetic field is

$$\vec{F}_b = q\,\vec{V} \times \vec{B} \qquad \text{A2.2}$$

so that the equation of motion (eq. 3-1) is

$$m\,\frac{d\vec{V}}{dt} = q\,(\vec{E} + \vec{V} \times \vec{B}) \qquad \text{A2.3}$$

or in component form,

$$m\,\frac{dV_x}{dt} = q\,(E_x + V_y B_z - V_z B_y) \qquad \text{A2.4}$$

$$m\,\frac{dV_y}{dt} = q\,(E_y + V_z B_x - V_x B_z) \qquad \text{A2.5}$$

$$m\,\frac{dV_z}{dt} = q\,(E_z + V_x B_y - V_y B_x) \qquad \text{A2.6}$$

Since the electric field is given by

$$\vec{E} = -\vec{V}_{sw} \times \vec{B} \qquad \text{A2.7}$$

$\vec{E}$ is always perpendicular to $\vec{B}$. So without loss of generality, we can take $\vec{B}=B\hat{z}$ and $\vec{E}=E\hat{y}$. Equations 4,5, and 6 of this section then become,

$$m\frac{dV_x}{dt} = q\,V_y\,B \qquad \text{A2.8}$$

$$m\frac{dV_y}{dt} = q\,E - q\,V_x\,B \qquad \text{A2.9}$$

$$m\frac{dV_z}{dt} = 0 \qquad \text{A2.10}$$

Taking the time derivative of equation A2.8 and substituting it into equation A2.9 gives

$$m(m/qB)\,\frac{d^2V_x}{dt^2} = q\,E - q\,V_x\,B \qquad \text{A2.11}$$

or

$$\frac{d^2V_x}{dt^2} + (qB/m)^2V_x = (q^2\,E\,B/m^2) \qquad \text{A2.12}$$

Defining

$$\omega = q\,B\,/\,m$$

$$\text{A2.13}$$

and

$$K = (q^2\,E\,B/\,m^2)$$

equation A2.12 becomes

$$\frac{d^2V_x}{dt^2} + \omega^2V_x = K \qquad \text{A2.14}$$

Equation A2.14 is a well known second order, first degree linear differential equation with constant coefficients whose solution is of the form

$$V_x(t) = A \cos \omega t + D \sin \omega t + C \qquad \text{A2.15}$$

The constant C can be determined by substituting equation A2.15 into equation A2.14. i.e.

$$\begin{aligned} \dot{V}_x &= - \; A \sin \omega t + \; D \cos \omega t \\ \ddot{V}_y &= - \; \omega^2 A \cos \omega t - \; \omega^2 \; D \sin \omega t \qquad \text{A2.16} \\ &= - \; \omega^2 (V_x - C) \end{aligned}$$

so that

$$\ddot{V}_x + \omega^2 V_x = K \qquad \text{A2.17}$$

becomes

$$C\,\omega^2 = K \qquad \text{A2.18}$$

or

$$C = K/\omega^2 = E / B \qquad \text{A2.19}$$

A and D can be determined by applying the boundary conditions at t=0 and equation A2.8.

$$A = V_{xo} - E / B \qquad \text{A2.20}$$

and from equation A2.16 and A2.8

$$\hat{V}_x(0) = \omega D = qB/m \quad V_{yo} \qquad \text{A2.21}$$

or

$$D = V_{yo} \qquad \text{A2.22}$$

and hence,

$$V_x(t) = (V_{xo} - E/B) \cos \omega t + V_{yo} \sin \omega t + E/B \qquad \text{A2.23}$$

Similarly,

$$V_y(t) = V_{yo} \cos \omega t - (V_{xo} - E/B) \sin \omega t \qquad \text{A2.24}$$

and from eq. A2.10,

$$V_z(t) = V_{zo} \qquad \text{A2.25}$$

The quantity E/B will be shown to be the magnitude of the drift velocity. Therefore the equations for the velocity are

$$V_x(t) = (V_{xo} - V_d) \cos \omega t + V_{yo} \sin \omega t + V_d \qquad \text{A2.26}$$
$$V_y(t) = V_{yo} \cos \omega t - (V_{xo} - V_d) \sin \omega t \qquad \text{A2.27}$$
$$V_z(t) = V_{zo} \qquad \text{A2.28}$$

Integrating eqs. 26 through 28 of this section and applying the condition that the particle start out at the origin yields,

$$X(t) = \left((V_{xo}-V_d)/\omega\right)\sin\omega t + (V_{yo}/\omega)(1-\cos\omega t) + V_d t \qquad \text{A2.29}$$

$$Y(t) = (V_{yo}/\omega)\ \sin\omega t + \left((V_{xo}-V_d)/\omega\right)(\cos\omega t - 1) \qquad \text{A2.30}$$

$$Z(t) = V_{zo}t \qquad \text{A2.31}$$

Equations 29 and 30 are the parametric equations of a cycloid in the x-y plane and the z-motion is independent of the x-y motion. The transformation from a fixed coordinate system to one that is moving parallel to the x-axis with velocity V_D is

$$\begin{aligned} X' &= X - V_d t \\ Y' &= Y \\ Z' &= Z \end{aligned} \qquad \text{A2.32}$$

This implies that eqs. A2.30 and A2.31 are unchanged in such a transformation but equation A2.29 becomes,

$$X'(t) = \left((V_{xo}-V_d)/\omega\right)\sin\omega t + V_{yo}/\omega\ \ (1-\cos\omega t)$$

Let $A = (V_{xo}-V_d)/\omega$ and $D = V_{yo}/\omega$ $\phi=\omega t$ then,

$$\begin{aligned} X' &= A\sin\phi + D(1-\cos\phi) \\ Y' &= D\sin\phi + A(\cos\phi - 1) \end{aligned} \qquad \text{A2.33}$$

Rewriting eqs. A2.33,

$$(X' - D) = A \sin\phi - D \cos\phi$$
$$(Y' - (-A)) = D \sin\phi + A \cos\phi \qquad \text{A2.34}$$

Defining the angle,

$$\theta = \tan^{-1}(A/D) \qquad \text{A2.35}$$

then equations A2.34 become,

$$(X' - D) = \sqrt{A^2 + D^2} \cos(\theta + \phi)$$
$$(Y' - (-A)) = \sqrt{A^2 + D^2} \sin(\theta + \phi) \qquad \text{A2.36}$$

Let $R = \sqrt{A^2 + D^2}$, then

$$(X' - D)^2 + (Y' - (-A))^2 = R^2 \qquad \text{A2.37}$$

Apparently the equations A2.29 and A2.30 represent circular motion when transformed to a system that is moving parallel to the x-axis at velocity V_d. The center of the circle in the moving frame is

$$X_c = D = V_{yo}/\omega \qquad Y_c = -A = (V_d - V_{xo})/\omega \qquad \text{A2.38}$$

and it has radius,

$$R = 1/\omega \left((V_{xo}-V_d)^2 + V_{yo}^2 \right)^{1/2} = mV_\perp' / qB \qquad \text{A2.39}$$

where $\vec{V}_\perp'$ is the perpendicular velocity in the moving frame. Hence equations 3-5 and 3-6.

The particle appears to move under the influence of a magnetic field only in the moving frame. That is, we have transformed into the frame in which there is no electric field.

$$\vec{E}_\perp' = \gamma (\vec{E}_\perp + \vec{V} \times \vec{B}) \qquad \text{A2.40}$$

Consider the relation,

$$\vec{B} \times (\vec{E}_\perp \times \vec{B}) = B^2 \vec{E}_\perp - (\vec{B} \cdot \vec{E}_\perp) \vec{B} \qquad \text{A2.41}$$

$$\Rightarrow \qquad \vec{E}_\perp = -(\vec{E}_\perp \times \vec{B}) \times \vec{B} / B^2 \qquad \text{A2.42}$$

but from eq. A2.40,

$$\vec{E}_\perp = - \vec{V} \times \vec{B} \qquad \text{A2.43}$$

Evidently,

$$\vec{V} = (\vec{E} \times \vec{B}) / B^2 \qquad \text{A2.44}$$

which is equivalent to equation 3-8.

The magnitude of $\vec{V}$ is

$$E_\perp / B = V_d \qquad \text{A2.45}$$

Hence the particle obeying eq. A2.3 seeks circular motion in a frame in which the electric field is zero, i.e. one moving with velocity $\vec{V}$ such that the component of the velocity that is perpendicular to the field is equal to the drift velocity. Obviously, the particle can move in the z-direction as well as in the x-y plane, but any velocity it has in the z-direction is velocity parallel to the field and it will still be moving in a frame in which the electric field is zero. Again, since the z-motion and the x-y planar motion are uncoupled, the total motion can be described as cycloidal in the x-y plane and uniform translation of that motion in the z-direction. The resultant velocity vector of the particle's guiding center is

$$\vec{V}_r = V_{zo}\,\hat{z} + V_d\,\hat{x} \qquad \text{A2.46}$$

which is equivalent to eq. 3-7. Clearly, the particle moving in a frame with velocity $\vec{V}_r$ sees no electric field.

$$\begin{aligned} \vec{E}'_{\perp} &= \gamma\,(\vec{E}_{\perp} + (V_{zo}\hat{z} + V_d\,\hat{x})\ X\ B\,\hat{z}) \\ &= \gamma\,(\vec{E}_{\perp} + V_d B\,\hat{x}\ X\ \hat{z}) \qquad \text{A2.47} \\ &= \gamma\,(\vec{E}_{\perp} - \vec{E}_{\perp}) = 0 \end{aligned}$$

Since the perpendicular $\vec{E}$ field is due to the solar wind velocity $\vec{V}_{sw}$ in the present treatment, using eq. A2.44 and $\vec{E}=-\vec{V}_{sw} X\ \vec{B}$ it is easy to see that

$$\vec{V}_d = \vec{V}_{sw} - (\vec{V}_{sw} \cdot \hat{B})\ \hat{B} \qquad \text{A2.48}$$

$$\vec{V}_d = (\ -(\vec{V}_{sw} \times \vec{B}) \times \vec{B}\ ) / B^2 \qquad \text{A2.49}$$

or using the identity,

$$\vec{A} \times (\vec{B} \times \vec{C}) = (\vec{B} \cdot \vec{A})\ \vec{C} - (\vec{C} \cdot \vec{A})\ \vec{B} \qquad \text{A2.50}$$

$$\vec{V}_d = (\vec{V}_{sw}\ B^2 - (\vec{V}_{sw} \cdot \vec{B})\ \vec{B}\ ) / B^2$$

$$\vec{V}_d = \vec{V}_{sw} - (\vec{V}_{sw} \cdot \hat{B})\ \hat{B} \qquad \text{A2.51}$$

hence equation 3-9.

Appendix 3

A3.1 A representative correlation program is discussed in this section, viz. the program that produced figure 5-6. The basic idea behind all of the correlation programs was discussed in chapter 5 and will not be repeated here. Only the details of the procedure used to obtain the results are relevant to this discussion.

Program A3.1 does the following:

a.) reads the Explorer 35 magnetometer tape to find the start time

b.) reads the SIDE data tape to find start time

c.) reads a record of Explorer 35 data to determine the value of the field latitude for that 82 second interval and decides the appropriate bin number for that latitude (i.e. for the 180 values of field latitude from -90° to +90°, 90 bins of 2° each are used and are numbered from 1 to 90).

d.) after selecting the bin number, the average integral flux over the same 82 second interval is calculated from the SIDE data tape and this number is deposited in memory at that bin location.

e.) The processes c. and d. above are repeated until the period of interest has been evaluated. Each time flux is added to a particular bin, a counter for that bin is incremented so that the number of times that bin was encountered is known.

f.) at the end of the period of interest, the total accumulated flux in each bin is divided by the number of times that that bin was encountered. Thus the number obtained in that bin represents the average integral flux observed at a given latitude over the period of interest.

g.) The results of all 90 bins are then dumped onto magnetic tape and are subsequently plotted to obtain figure 5-6.

The details of the calculation of the integral flux are as follows. Figure A3.1 shows the meaning of the parameters relevant to the following discussion and the approximate nature of the integration over the energy spectrum. The appropriate values of the parameters for the Apollo 14 SIDE are given in table A3.1.

For the ith energy channel, the number of counts C_i will be given by

$$C_i = R_i \Delta t \qquad R_i = \text{count rate } (\text{sec}^{-1})$$

$$\Delta t = 1.13 \text{ sec}$$

the count rate R_i is related to the differential energy flux by

Figure A3.1 Illustration of the technique used to calculate integral flux. The number that represents the integral flux is given by summing the areas of the unshaded rectangles defined by ΔE_ω and (dj/dE).

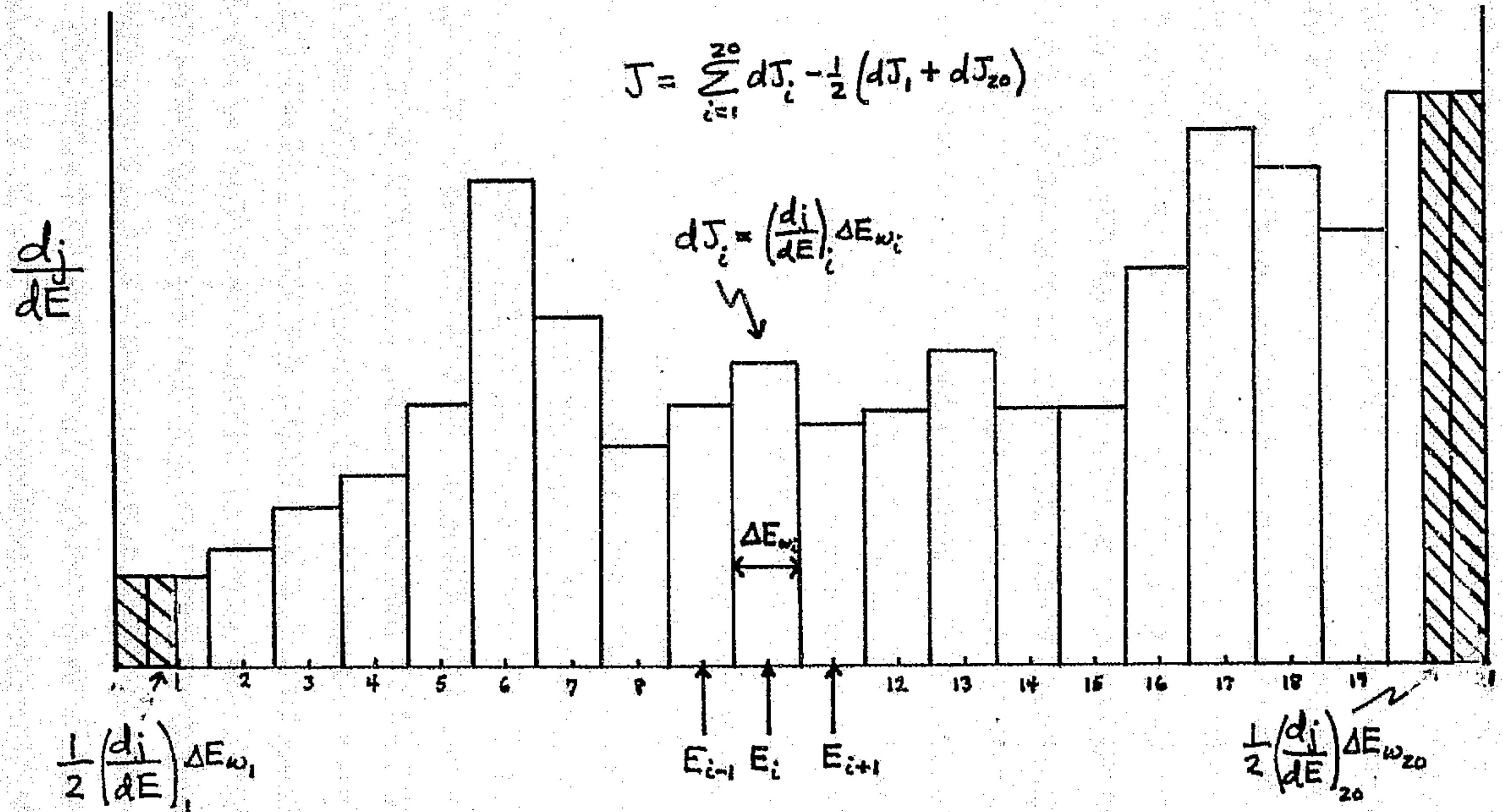$\frac{dj}{dE}$
$J = \sum_{i=1}^{20} dJ_i - \frac{1}{2}\left(dJ_1 + dJ_{20}\right)$
$dJ_i = \left(\frac{dj}{dE}\right)_i \Delta E_{\omega_i}$
ΔE_{ω_i}
1
2
3
4
5
6
7
8
12
13
14
15
16
17
18
19
E_{i-1}
E_i
E_{i+1}
$\frac{1}{2}\left(\frac{dj}{dE}\right)_1 \Delta E_{\omega_1}$
$\frac{1}{2}\left(\frac{dj}{dE}\right)_{20} \Delta E_{\omega_{20}}$

Figure A3.1

Table A3.1

nominal energy		peak response	ΔE_ω	$(10^{-5} \text{cm}^2\text{-str})$	
				G	ΔE (FWHM)
1	10	7	8.5	3.6	1.4
2	20	17	11.5	5.0	1.0
3	30	30	14.0	6.8	2.0
4	50	45	19.5	3.2	3.0
5	70	69	25.5	15.0	6.0
6	100	96	88.0	13.0	6.0
7	250	245	214.5	7.7	24.0
8	500	525	242.5	6.5	30.0
9	750	730	237.5	3.3	30.0
10	1000	1000	235.0	9.2	102.0
11	1250	1200	225.0	4.5	50.0
12	1500	1450	262.5	3.2	76.0
13	1750	1725	287.5	9.0	140.0
14	2000	2025	262.5	4.7	230.0
15	2250	2250	237.5	7.9	180.0
16	2500	2500	225.0	9.8	190.0
17	2750	2700	225.0	3.3	250.0
18	3000	2950	262.5	9.9	320.0
19	3250	3225	287.5	8.8	330.0
20	3500	3525	262.5	7.1	300.0

$$R_i = \left(\frac{dj}{dE}\right)_i \Delta E_i \; G_i$$

where,

$$G_i = G_i(E) \quad (\mathrm{cm}^2\text{-str})$$

$$\Delta E_i = \text{energy passband (FWHM)}$$

The flux, integrated over the energy spectrum is J.

$$J = \sum_{i=1}^{20} \left(\frac{dj}{dE}\right)_i \Delta E_{\omega_i} - 1/2 \left\{ \left(\frac{dj}{dE}\right)_1 \Delta E_{\omega_1} + \left(\frac{dj}{dE}\right)_{20} \Delta E_{\omega_{20}} \right\}$$

$$\Delta E_{\omega_i} = \text{width of the i th integration interval}$$

or in terms of the known parameters,

$$J = \sum_{i=1}^{20} \frac{C_i \, \Delta E_{\omega_i}}{\Delta t \, \Delta E_i G_i} - 1/2 \left\{ \frac{C_1 \, \Delta E_{\omega_1}}{\Delta t \, \Delta E_1 G_1} + \frac{C_{20} \, \Delta E_{\omega_{20}}}{\Delta t \, \Delta E_{20} G_{20}} \right\}$$

(See figure A3.1 to understand the second term)

The values of ΔE_{ω_i} were determined by taking half of the energy difference between the i th peak and the i+1 th peak and half of the difference between E_i and E_{i-1} , i.e.,

$$\Delta E_{\omega_i} = 1/2 \left\{ E_{i+1} - E_{i-1} \right\}$$

<u>A3.2</u> Program A3.2 is the program used to generate the synthetic data of chapter 5. The theory underlying the generation of these data was covered in chapter 4. The program presented here is the SDS 910 version. The IBM version is somewhat lengthy and will not be included. It is basically the same as the 910 version except that the ephemeris data are calculated in that program. However, the tests relevant to the acceptance criteria are the same.

To facilitate the understanding of program A3.2, it should suffice to define the parameters relevant to the theory of chapter 4.

T=kinetic energy of the particle

D=d=distance from the center of the earth to the nose of the shock.

CAPD=D=distance from the center of the earth to the wing of the shock measured along the y-axis.

CR=r=position vector of the moon

APX,APY,APZ,=components of the detector look vector in a solar ecliptic system $\hat{D}$

VR=$\vec{V}_r$=resultant velocity vector for the guiding center

VDOTAP= $\vec{V}_r \cdot \hat{D}$

B2 and AC4 represent equations 4-22

HGT=counts

```
C PROGRAM A3.1
      DIMENSION IRY(28),BIN(91),ITIME(5),IDIV(91),FLX(10),IW(20)
      CALL ITYPE(ITIME)
C TYPE IN START TIME
      CALL ITYPE(IRUN)
C TYPE IN RUNTIME IN HOURS
      CALL ITYPE(IW)
C TYPE IN MODIFIED GEOMETRIC FACTORS
      HTODAY=1./24.
      TODAY=HTODAY/60.
      STODAY=HTODAY/3600.
      DGAP=3.*TODAY
      RUNTIM=FLOAT(IRUN)*HTODAY
      TB=FLOAT(ITIME(2))+FLOAT(ITIME(3))*HTODAY+FLOAT(ITIME(4))*TODAY+FL
     1OAT(ITIME(5))*STODAY
      TEND=TB+RUNTIM
      DO 1 K=1,91
      BIN(K)=0.
1     IDIV(K)=0
      ASSIGN 2 TO IPAR
      ASSIGN 3 TO IEOF
2     CONTINUE
      CALL SETUP(1,28,IRY,IREC,IPAR,IEOF)
C FIND START TIME ON EXPLORER 35 TAPE
17    READ INPUT TAPE 2,16,IDAY,IHR,IMIN,ISEC
16    FORMAT(4I3)
      IDAY=IDAY+1
      IF(IDAY-ITIME(2))17,18,21
18    IF(IHR-ITIME(3))17,19,21
19    IF(IMIN-ITIME(4))17,20,21
20    IF(ISEC-ITIME(5))17,21,21
21    CONTINUE
      TB=FLOAT(IDAY)+FLOAT(IHR)*HTODAY+FLOAT(IMIN)*TODAY+FLOAT(ISEC)*STO
     1DAY
C  FIND START TIME ON SIDE TAPE
51    CALL INPUT
      IF(IRY(2))51,22,22
22    T=FLOAT(IRY(2))+FLOAT(IRY(3))*HTODAY+FLOAT(IRY(4))*TODAY+(FLOAT(IR
     1Y(5))/1000.)*STODAY
25    IF(T-TB)23,24,24
23    T=T+24.16*STODAY
      CALL INPUT
      IF(IRY(2))25,22,22
24    TPLUS=T+24.16*STODAY
      TLAST=TB
C BOTH TAPES ARE ON START TIME HERE
C READ EXP 35 TAPE
30    READ INPUT TAPE 2,26,IDAY,IHR,IMIN,ISEC,BLAT
```

```
26     FORMAT(4I3,32X,F6.1)
       IDAY=IDAY+1
       TB=FLOAT(IDAY)+FLOAT(IHR)*HTODAY+FLOAT(IMIN)*TODAY+FLOAT(ISEC)*STO
      1DAY
       GAP=TB-TLAST
       IF(GAP)30,30,50
50     IF(GAP-DGAP)48,48,51
C CALCULATE BIN NUMBER
48     I=BLAT/2.
       I=I+46
       N=0
       SUM=0.
C CALCULATE INTEGRAL FLUX
29     CALL INPUT
       N=N+1
       CT=0.
       DO 4 J=1,20
       IF(IRY(J+5))61,4,4
61     IRY(J+5)=0
4      CT=CT+FLOAT(IRY(J+5))*FLOAT(IW(21-J))/10.
       CT=CT-(FLOAT(IRY(6))*IW(20)+FLOAT(IRY(25))*IW(1))/20.
62     SUM=SUM+CT
       IF(IRY(2))27,28,28
27     TP=TPLUS
       GO TO 33
28     TP=FLOAT(IRY(2))+FLOAT(IRY(3))*HTODAY+FLOAT(IRY(4))*TODAY+(FLOAT(I
      1RY(5))/1000.)*STODAY
33     TPLUS=TP+24.16*STODAY
       IF(TP-TB)29,31,31
31     SUM=SUM/FLOAT(N)
       BIN(I)=BIN(I)+SUM
       IDIV(I)=IDIV(I)+1
       TLAST=TB
       IF(TB-TEND)30,32,32
32     CONTINUE
       CALL ITYPE(IWATE)
C MOUNT BLANK TAPE ON UNIT 1
       DO 13 K=1,81,10
       DO 57 J=1,10
       I=K+J-1
       IF(IDIV(I))14,14,56
14     FLX(J)=0.
       GO TO 57
56     FLX(J)=BIN(I)/FLOAT(IDIV(I))
57     CONTINUE
C WRITE VALUES OF INTEGRAL FLUX
       WRITE OUTPUT TAPE 1,15,(FLX(J),J=1,10)
15     FORMAT(8X,10F10.3)
C WRITE NUMBER OF TIMES BIN WAS ENCOUNTERED
13     WRITE OUTPUT TAPE 1,58,(IDIV(J),J=K,K+9)
58     FORMAT(8X,10I10)
       END FILE 1
3      CONTINUE
       END
```

```
C PROGRAM A3.2
C J. BENSON    RICE UNIVERSITY
C IP(1)=DISTANCE TO NOSE OF SHOCK IN RE
C IP(2)/IP(3)=DISTANCE TO MOON AT BOW SHOCK CROSSING IN RE
C IP(4)/IP(5)=SOLAR ECL LONG AT BOW SHOCK CROSSING IN RADIANS
C IP(6)=SOLAR WIND VELOCITY IN KM/SEC
C IP(7)=SIZE OF THE LOOK CONE IN DEGREES
C IP(8)=SHADOW ANGLE IN DEGREES
C SHADOW ANGLE IS USED TO AVOID UNECESSARY TESTING
C IP(9)=NUMBER OF RECORDS TO BE PROCESSED AT A TIME
C IP(10)=SOURCE NUMBER
      DIMENSION T(20),IP(10),IR(24),R(12),ICUT(28)
      EQUIVALENCE(IR(2),R(1))
      ASSIGN 40 TO IPAR
      ASSIGN 41 TO IEOF
C CALCULATE 20 VALUES OF THE ENERGY
      DO 2 K=1,14
2     T(21-K)=3500.-(K-1)*250.
      T(6)=100.
      DO 3 K=1,3
3     T(6-K)=70.-(K-1)*20.
      T(1)=10.
      T(2)=20.
      CALL ITYPE(IP)
C TYPE IN INPUT PARAMETERS
      D=FLOAT(IP(1))
      RE=FLOAT(IP(2))/FLOAT(IP(3))
      SELABS=FLOAT(IP(4))/FLOAT(IP(5))
      VS=FLOAT(IP(6))
      SLA=FLOAT(IP(7))
      SHAD=FLOAT(IP(8))
      BETA=.08726
      PI=3.14159
      PI2=PI/2.
      TORAD=PI/180.
      SLA=SLA*TORAD
      CLA=SIN(PI2-SLA)
      SBS=SIN(SELABS)
      CBS=SIN(PI2-SELABS)
C CALCULATE VALUE OF WING DISTANCE CAPD
      CAPD=SQRT((-D*RE*RE*SBS*SBS)/(RE*CBS-D))
      SB=SIN(BETA)
      CB=SIN(PI2-BETA)
40    CALL SETUP(1,24,IR,IREC,IPAR,IEOF)
      DO 7 I=1,IP(9)
C READ EPHEMERIS DATA
      CALL INPUT
7     CONTINUE
```

```
C TEST SHADOW ANGLE
      IF(R(11)-SHAD)1,1,5
 1    DO 6 J=1,20
6     ICUT(J+5)=0
      GO TO 4
5     IF(R(11)-180.)9,16,16
16    IF(R(11)-SHAD-180.)1,1,9
9     CONTINUE
C CALCULATE SOLAR ECLIPTIC ANGULAR PARAMETERS
      SELD=SIN(R(7))
      CELD=SIN(PI2-R(7))
      SSELOD=SIN(R(8))
      CSELOD=SIN(PI2-R(8))
      SELA=SIN(R(9))
      CELA=SIN(PI2-R(9))
      SSELOA=SIN(R(10))
      CSELOA=SIN(PI2-R(10))
      SBLON=SIN(R(11)*TORAD)
      CBLON=SIN(PI2-R(11)*TORAD)
      SBLAT=SIN(R(12)*TORAD)
      CBLAT=SIN(PI2-R(12)*TORAD)
      BX=CBLAT*CBLON
      BY=CBLAT*SBLON
      BZ=SBLAT
      IF(BY)17,19,19
 19   BX=-BX
      BY=-BY
      BZ=-BZ
C CALCULATE R
 17   CR=SQRT(R(4)*R(4)+R(5)*R(5)+R(6)*R(6))
      CRX=CR*CELA*CSELOA
      CRY=CR*CELA*SSELOA
      CRZ=CR*SELA
C CALCULATE DETECTOR LOOK VECTOR
      APX=-CELD*CSELOD
      APY=-CELD*SSELOD
      APZ=-SELD
      DUNC=VS*CB*CBLAT*CBLON-VS*SB*CBLAT*SBLON
C EVALUATE 20 ENERGIES
      DO 4 K=1,20
      VP=SQRT(T(K)*1.602E-22)*1.0936E12
      HCT=0.
C EVALUATE 10 PITCH ANGLES
      DO 13 J=1,10
      PA=(J-1)*10.*TORAD
      SPA=SIN(PA)
      CPA=SQRT(1.-SPA*SPA)
      VP=VP*CPA
```

ORIGINAL PAGE IS
OF POOR QUALITY

```
C CALCULATE RESULTANT VELOCITY VECTOR
      VRX=-VS*CB+BX*DUNG+BX*VP
      VRY=VS*SB+BY*DUNG+BY*VP
      VRZ=BZ*(DUNG+VP)
      VR=SQRT(VRX*VRX+VRY*VRY+VRZ*VRZ)
C CALCULATE ANGLE BETWEEN VR AND DET LOOK VEC AND TEST
      VDOTAP=(VRX*APX+VRY*APY+VRZ*APZ)/VR
      IF(VDOTAP-CLA)13,10,10
10    IF(VDOTAP-1.)18,13,13
C TEST FOR SOURCE POINT
18    CAPA=.+((VRZ*VRZ)/(VRY*VRY))
      CAPB=((CAPD*CAPD)/D)*(VRX/VRY)-2*(CRY*(VRZ/VRY)*(VRZ/VRY)-CRZ*(VRZ
     1/VRY))
      BARF=((CRY*VRZ)/VRY)*((CRY*VRZ)/VRY)
      BELCH=-CRY*((2*CRZ*VRZ)/VRY+(CAPD*CAPD*VRX)/(D*VRY))
      ERUCT=(CAPD*CAPD*CRX)/D+CRZ*CRZ-CAPD*CAPD
      CAPC=BARF+BELCH+ERUCT
      B2=CAPB*CAPB
      AC4=4*CAPA*CAPC
      IF(B2-AC4)13,11,11
11    IF(PA)13,14,15
C FILL CHANNELS WITH APPROPRIATE COUNTS
14    HGT=IP(10)*1..*TORAD
      GO TO 13
15    HGT=HGT+IP(10)*SIN(PA)*1..*TORAD
13    CONTINUE
      IOUT(26-K)=HGT
  4   CONTINUE
      IOUT(1)=-1
      IOUT(2)=R(1)
      IOUT(3)=R(2)
      IOUT(4)=R(3)
      IOUT(5)=0
      DO 8 J=1,3
8     IOUT(J+25)=0
      CALL SETUP(2,28,IOUT,IREC,IPAR,IEOF)
C WRITE A SPECTRUM ON MAG TAPE
      CALL OUTPUT
      GO TO 41
41    CONTINUE
      END
```

Appendix 4

Brief review of the acceleration mechanisms.

A4.1 Sonnerup model- The basic idea of the Sonnerup model is simple specular reflection from the shock and subsequent energization of the particle by the interplanetary electric field. To get an order of magnitude estimate of the increase in energy after reflection we can calculate the ratio of the reflected energy to the initial energy. Assuming the reflected energy is given by the initial energy plus the energy given to the particle by the electric field over one half of a cyclotron orbit,

$$\epsilon_r = 1/2 \; m \; V_{sw}^2 + q \; E_{IP} \, \pi \, r \qquad \text{A4.1}$$

where

$$r = mV_{sw}/qB \qquad \text{A4.2}$$

and

$$E_{IP} = V_{sw} \; B \; \sin\psi \qquad \text{A4.3}$$

ψ = angle between V_{sw} and B

$$\epsilon_r = 1/2 \; mV_{sw}^2 + \pi mV_{sw}^2 \; \sin\psi \qquad \text{A4.4}$$

so that,

$$\epsilon_r/\epsilon_i = 1 + (mV_{sw}^2 \, \pi \sin\psi)/(1/2 \; mV_{sw}^2) \qquad \text{A4.5}$$

$$\epsilon_r/\epsilon_i = 1 + 2\pi \sin\psi \qquad \text{A4.6}$$

for a typical value of ψ, ($\psi = \pi/4$),

$$\epsilon_r/\epsilon_i = 5.45 \qquad \text{A4.7}$$

That is, a particle could gain roughly 5.5 times its incoming energy by this process. For a typical bulk flow velocity of about 400 km/sec, the reflected particle energy would be, by eq. A4.7, about 4.7 keV. This is the right order of magnitude for the observed particles in the upstream region. For different values of ψ the energy gained varies from 0 to about 7.28 times the initial energy.

Sonnerup treats this problem in a more rigorous fashion in his 1969 paper where he considers that the particle energy is conserved in the frame of reference in which the electric field vanishes. The results of this more rigorous treatment will be stated here. By considering the reflection process in the frame of zero $\vec{E}$ field and the rest frame of the shock, Sonnerup obtains,

$$\epsilon_r/\epsilon_i = 1 + 2 \cdot \frac{(1+\delta)\cos(\phi+\gamma)\sin(\psi-\phi)\sin(\psi+\gamma)}{(1+\mu)\cos^2(\psi-\phi)} \qquad \text{A4.8}$$

where the angles are those shown in figure A4.1 and the definitions of μ and δ are as follows.

$$\mu = V_{\perp i}^2/V_i^2 \qquad \delta = V_{\parallel r}/V_{\parallel i} \qquad \text{A4.9}$$

Figure A4.1a. Vector diagram showing how the incident particle guiding center velocity vector, $\vec{V}_i$, is decomposed into a component, $\vec{V}_{\parallel i}$, along the field and a component $\vec{V}_t$ along the shock front.

Figure A4.1b. Similarly the velocity vector of the reflected particle is decomposed into $\vec{V}_{\parallel r}$ along the field and $\vec{V}_t$ along the shock front. The angle ψ between the field direction and the solar wind vector $\vec{V}_{sw}$ is the garden hose angle. The angle ϕ between the shock normal and $\vec{V}_{sw}$ measures the obliqueness of the shock at the point of reflection. The angle γ is non zero only if the incident particle has a non-zero thermal velocity component parallel to the field.

Figure A4.1c. Ratio of the particle energy after and before reflection as a function of shock obliquity.

[the above is paraphrased from Sonnerup (1969)]

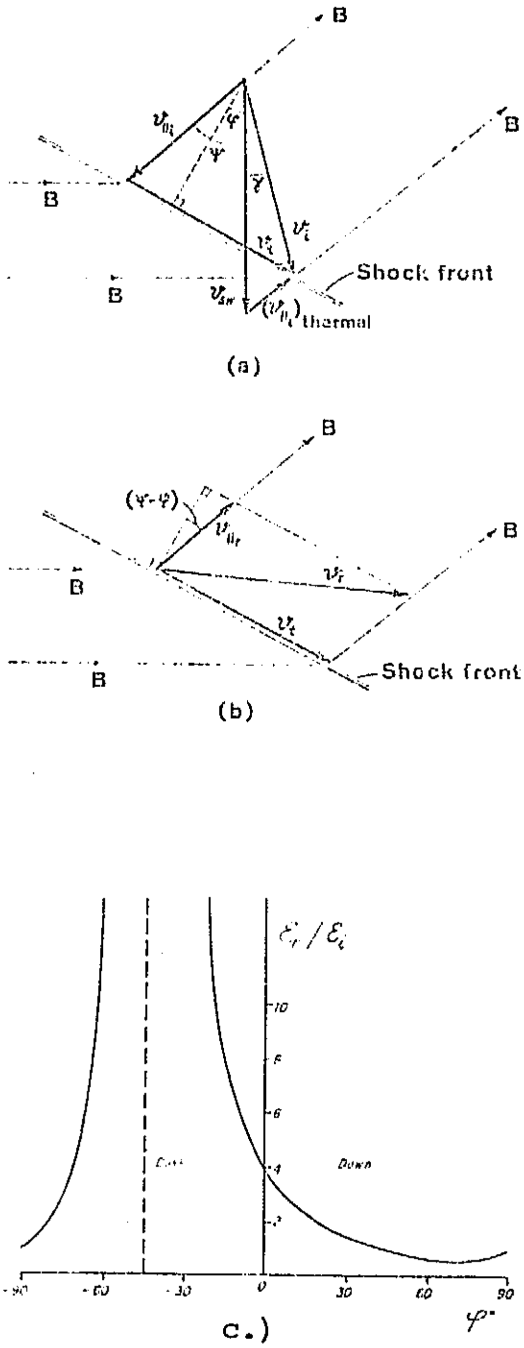

(a)

(b)

c.)

Figure A4.1

Figure A4.1c shows the energy ratio as a function of shock obliquity (ϕ) for the values $\psi = \pi/4$, $\delta = 1/2$ $\gamma=0$ $\mu=0$. It should be noted that the singularity in equation A4.8 at $\psi-\phi= \pi/2$ corresponds to the case in which transformation to the frame in which the $\vec{E}$ field is zero is not possible. That is, the singularity is artificial, physically, and simply means that no finite velocity vector $\vec{V}_t$ (see fig. A4.1) can be found that makes the solar wind velocity parallel to $\vec{B}$ in the moving frame. It can be seen from examining the curve in figure A4.1 that the Sonnerup model predicts very high values of energization on the dusk side of the magnetosphere and relatively small ones on the dawn side. Although electrons of energy greater than 40 keV have been observed [Anderson,(1968)] and more recently protons of energy 30 to 100 keV [Lin et al., (1974)] in the bow shock regions, no such asymmetry has been observed. The dawn side energy increases from the model are much too low to account for the observed high energy particles in this region. On these bases one must conclude that the Sonnerup model is probably not correct.

A4.2 Fermi acceleration mechanism-[Jokipii, (1966)]

The basic idea of the Jokipii model of Fermi acceleration at the bow shock is that quasi-thermalized particles escape from the shock region into a region that is bounded on one end by the bow shock and on the other by a magnetic irregularity that forms a mirror point upstream of the bow shock. (see figure A4.2) Under the assumption that the particle velocity parallel to the field is much greater than the velocity of the moving irregularity, the number of collisions per second that the particle makes with the mirror point is

$$V_{p_{\parallel}} / 2\,L(t) \qquad \text{A4.10}$$

where

$$L(t) = L_o - Vt \qquad \text{A4.11}$$

and the gain in momentum on each collision is

$$\Delta p = m\,V \qquad \text{A4.12}$$

This treatment differs slightly from Jokipii's but the differences are primarily notational; for instance in figure A4.2, $c\beta_o$=V and t_o=0.

Figure A4.2 Jokipii model of the Fermi mechanism for accelerating particles at the bow shock. The trapping region is defined by the bow shock at one end and a magnetic mirror at the other. The magnetic irregularity moves toward the shock with velocity $c\beta_0$.

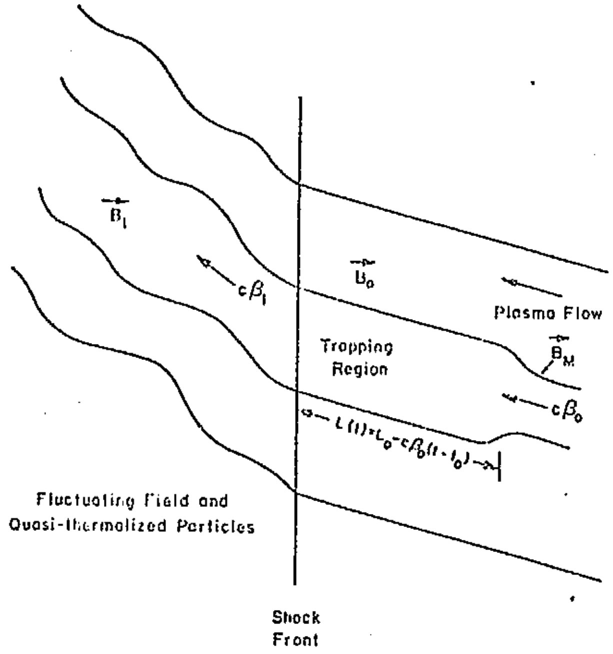
$\vec{B}_1$
$c\beta_1$
$\vec{B}_0$
Plasma Flow
$\vec{B}_M$
Trapping Region
$c\beta_0$
$L(t) = L_0 - c\beta_0(t - t_0)$
Fluctuating Field and Quasi-thermalized Particles
Shock Front

Figure A4.2

From equations A4.10 and A4.12, the time rate of gain of momentum is

$$p\left(\frac{V_p}{2L}\right) \qquad \text{A4.13}$$

or

$$\frac{dp}{dt} = mV_{p_{//}} V/2L = \mu V_p\ /2L \qquad \text{A4.14}$$

where

$$\mu = V_{p_{//}}/V_p = \cos(\text{pitch angle}) \qquad \text{A4.15}$$

and

$$p = m\ V_p \qquad \text{A4.16}$$

but since,

$$W = (m_o^2 c^4 + p^2 c^2)^{1/2} \qquad \text{A4.17}$$

$$p = W^2/\ c^2 - m_o^2\ c^2 \qquad \text{A4.18}$$

$$\frac{dp}{dt} = 2\ W/\ c^2\ \frac{dW}{dt} \qquad \text{A4.19}$$

Comparing equations A4.19 and A4.14 we see that

$$\frac{dW}{dt} = (\mu V/L(t))\ W \left[1 - (m_o^2 c^4/W^2)\right] \qquad \text{A4.20}$$

which differs from Jokipii's result only in notation. This differential equation was derived under the condition that $V_p << V$. If the magnetic moment of the particle is conserved in collisions with the shock and mirror then as the particle gains energy its pitch angle decreases and it will eventually be lost to the solar wind. This sets a limit on the energy that can be gained in a process like this and that limit depends on the dimensions of the trapping region and the velocity of the irregularity in the field. One gathers from this simplistic approach that a particle could gain parallel energy only up to about that associated with the bulk flow velocity of the solar wind. Energies observed in the upstream regions are much higher than this (up to 100 keV protons) [Lin et al. (1974)] which requires some other process to produce these particles. Jokipii depends on pitch angle scattering at a fluctuating shock to avoid losing his particles too quickly. Lin et al. [1974] have pointed out that this acceleration mechanism predicts a hardening of the energy spectrum toward the wings of the shock due to the longer time that a trapping region is in contact with the shock which is not observed.

Acknowledgements

I wish to thank my thesis advisor, Dr. John W. Freeman, Jr., for giving me the opportunity to work with a unique project, the Suprathermal Ion Detector Experiment. Dr. Freeman's patience and understanding have been indispensable in the final realization of this thesis.

I would also like to thank Dr. H. Kent Hills for countless hours he has spent discussing the subject matter of this thesis with me. His immense knowledge of computers and his astonishing attention to detail have been invaluable in the sucessful completion of this work.

I have benefitted greatly from my professional association and personal friendship with Dr. Richard R. Vondrak who has contributed much of his time to valuable discussions concerning this thesis.

I would like to thank Tom Rich for his help in computer programming and Dave Nystrom and John McGarity for maintaining the sanity of the SDS 910 computer during the past three years.

I have enjoyed knowing and working with the other members of the SIDE group, past and present, namely, Dr. Martha Fenner, my good friend and ex-office mate, Drs. R.A. Lindeman and R.A. Medrano, Mohammed Ibrahim, Dave Hardy, Henry Schneider and Dr. Jürg Meister.

Thanks also go to Steve Bowling and Mike Geis for many valuable discussions.

Finally, I would like to thank my wife Jackie for unselfishly spending many nights as a computer widow and for typing the final copy of this thesis.

This research has been supported in part by the National Aeronautics and Space Administration under contract NAS 9-5911.

Anderson, K. A., Energetic Electrons of Terrestrial Origin Upstream in the Solar Wind, JGR, 73, 2387, 1968.

Asbridge, J. R., Bame, S. J., Strong, I. B., Outward Flow of Protons from the Earth's Bow Shock, JGR, 73, 5777, 1968.

Axford, W.I., The Interaction Between the Solar Wind and the Earth's Magnetosphere, JGR, 67, 3791, 1962.

Bowling, S. B., The Magnetic Field Structure of the Plasma Sheet at 30 Re, M.S. Thesis, Rice U., 1973.

Colburn, D.S., Currie, R.G., Mihalov, J.D., Sonett, C.P., Diamagnetic Solar Wind Cavity Discovered Behind the Moon, Science, 158, 1040, 1967.

Colburn, D.S., Mihalov, J.D., Sonett, C.P., Waid, S.H., The Lunar Cavity in the Solar Wind, Trans. Amer. Geophys. Union, 49, 234, 1968.

Colburn, D.S., Description of Ames Magnetometer Data from Explorer 33 and Explorer 35 deposited in the Data Bank, NASA/Ames Research Center preprint, 1969.

Dyal, P., Parkin, C.W., Colburn, D.S., Schubert, G., Lunar Surface Magnetometer Experiment, Apollo 16 Preliminary Science Report, 11-1, 1972.

Dyal, P., Parkin, C.W., Sonett, C.P., DuBois, R.L., Simmons,G., Lunar Portable Magnetometer Experiment, Apollo 16 Preliminary Science Report, 12-1, 1972.

Fairfield, D.H., Bow Shock Associated Waves Observed in the Far Upstream Interplanetary Medium, JGR, 74, 14, 3541, 1969.

Fenner, M.A., Magnetosheath Plasma at 60 Re, M.S. Thesis, Rice U., 1971.

Fenner, M.A., Freeman, J.W., Jr., Hills, H.K., The Electric Potential of the Lunar Surface, Proceedings of the Fourth Lunar Science Conference, 3, 2877, 1973.

Fenner, M. A., Observations of Magnetosheath Plasma at the Lunar Orbit, Ph.D. Thesis, Rice U., 1974.

Frank, L.A. and Shope, W.L., A Cinematographic Display of Observations of Low Energy Proton and Electron Spectra in the Terrestrial Magnetosphere and Magnetosheath and in the Interplanetary Medium, Trans. Am. G. U., 49, 1, 279, 1968.

Frank, L.A., On the Presence of Low Energy Protons ($5 \leq E \leq 50$ keV) in the interplanetary medium, JGR, 75, 4, 707, 1970.

Freeman, J.W., Jr., The ALSEP Lunar Ionosphere Detector, Rice U. preprint, 1969.

Freeman, J.W., Jr., Balsiger, H., Hills, H.K., Preliminary Results from the Lunar Ionosphere Detector, *Apollo 12 Preliminary Science Report*, 83, 1970.

Freeman, J.W., Jr., Energetic Ion Bursts on the Nightside of the Moon, *JGR*, *77*, *1*, 239, 1972.

Geiss, J., Beuhler, F., Cerutti, H., Eberhardt, P., Filleux, Ch. Solar Wind Composition Experiment, *Apollo 16 Preliminary Science Report*, 14-1, 1972.

Goldstein, H., *Classical Mechanics*, Addison Wesley Pub. Co., Reading, Mass., 1950.

Greenstadt, E.W., Green, I.M., Inouye, G.T., Correlated Magnetic Field and Plasma Observations of the Earth's Bow Shock, *JGR*, *73*, *1*, 51, 1968.

Heppner, J.P., Sugiura, M., Skillman, T.L., Ledley, B.G., Campbell, M., OGO-A Magnetic Field Observations, *JGR*, *72*, *21*, 5417, 1967.

Hills, H.K., ALSEP/SIDE Ephemeris Computations, Rice U. preprint, 1969.

Hills, H.K., Meister, J., Vondrak, R.R., Freeman, J.W., Jr., The Suprathermal Ion Detector Experiment, *Apollo 15 Preliminary Science Report*, 12-1, 1971.

Hundhausen, A.J., Composition and Dynamics of the Solar Wind Plasma, *Rev. of Geophys. and Space Physics*, *8*, *4*, 729, 1970.

Johnson, F.S., Evans, D.E., Caroll, J.M., Cold Cathode Gauge Experiment, *Apollo 14 Preliminary Science Report*, 185, 1971.

Jokipii, J.R., A Model of Fermi Acceleration at Shock Fronts with an Application to the Earth's Bow Shcok, *Astrophys. J.*, *143*, *3*, 961, 1966.

Jokipii, J.R., Correlation of $\gtrsim$30 keV Electron Pulses and Magnetic Fields in the Magnetosheath and Beyond, *JGR*, *73*, *3*, 931, 1968.

Lin, R.P., Meng, C.I., Anderson, K.A., 30 to 100 keV Protons Upstream From the Earth's Bow Shock, *JGR*, *79*, *4*, 489, 1974.

Lindeman, R.A., Recurring Ion Events at the Lunar Surface, M.S. Thesis, Rice U., 1971.

Lindeman, R.A., Observations of Ions from the Lunar Atmosphere, Ph.D. Thesis, Rice U., 1973.

Lyon, E.F., Bridge, H.S., Binsack, J.H., Explorer 35 Plasma Measurements in the Vincinity of the Moon, JGR, 72, 6113, 1967.

Manka, R.H., Lunar Atmosphere and Ionosphere, Ph.D. Thesis, Rice U., 1972.

McKenzie, J.F., Hydromagnetic Wave Interaction with the Magnetopause and the Bow Shock, Planet. and Space Sci., 18, 1, 1-23, 1970.

Medrano, R.A., Unusual Solar Wind and Solar Proton Events Observed on the Lunar Surface, Ph.D. Thesis, Rice U., 1973.

Ness, N.F., Scearce, C.S., Seek, J.B., Initial Results of the IMP-1 Magnetic Field Experiment, JGR, 69, 17, 3531, 1964.

Ness, N.F., The Earth's Magnetic Tail, JGR, 70, 2989, 1965.

Ness, N.F., Behanon, K.W., Cantarano, S.C., Scearce, C.S., Observations of the Earth's Magnetic Tail and Neutral Sheet at 510,000 Kilometers by Explorer 33, JGR, 72, 927, 1967.

Ness, N.F., The Geomagnetic Tail, Rev. of Geophysics, 7, 1, 2, 97, 1969.

O'Brien, B.J., Reasoner, D.L., Charged Particle Lunar Environment Experiment, Apollo 14 Preliminary Science Report, 193, 1971.

Rich, F.J., Plasma in the Geomagnetic Tail Observed by the Charged Particle Lunar Environment Experiment, Ph.D. Thesis, Rice U., 1973.

Scarf, F.L. et al., Direct Correlations of Large-Amplitude Waves with Suprathermal Protons in the Upstream Solar Wind, JGR, 75, 34, 7316, 1970.

Sonnerup, B.U.O., Acceleration of Particles Reflected at a Shock Front, JGR, 74, 5, 1301, 1969.

Smith, E.J., Holzer, R.E., McLeod, M.G., Russell, C.T., Magnetic Noise in the Magnetosheath in the Frequency Range 3-300 Hz, JGR, 72, 19, 1967.

Spreiter, J.R., Summers, A.L., Alksene, A.Y., Hydomagnetic Flow around the Magnetosphere, Plan. and Spac. Sci., 14, 223, 1966.

Snyder, C.W., Clay D.R., Neugebauer, M., Initial Result from ALSEP Solar Wind Spectrometer (abstract), Trans. Am. Geo. U., EOS, 51, 407, 1970.

Snyder, C.W., Clay, D.R., Neugebauer, M., Solar Wind Spectrometer Experiment, Apollo 12 Preliminary Science Report, 75, 1970.

Van Allen, J.A., Fennell, J.F., Ness, N.F., Asymmetric Access of Energetic Solar Protons to the Earth's North and South Polar Caps, JGR, 76, 19, 4262, 1971.

Wolfe, J.H., McKibbin, D.D., Pioneer 6 Observations of a Steady State Magnetosheath, Plan. and Spac. Sci., 16, 953, 1968.

Wolfe, J.H., Intriligator, D.S., The Solar Wind Interaction with the Geomagnetic Field, Spac. Sci. Rev., 10, 4, 511-596, 1970.

Zhigulev, V.N., Romeshevskii, E.A., Concerning the Interaction of Currents Flowing in a Conducting Medium with the Earth's Magnetic Field, Soviet Phy. Dokl., 4, 859, 1959.